Bubble Rise Dynamics in Complex Fluids

Azin Padash

Submitted in partial fulfillment of the
requirements for the degree of
Doctor of Philosophy
under the Executive Committee
of the Graduate School of Arts and Sciences

COLUMBIA UNIVERSITY

2022

Abstract

Bubble Rise Dynamics in Complex Fluids

Azin Padash

Formation of gas bubbles in complex fluids and their subsequent rise due to buoyancy is a very important fundamental phenomenon both in nature and industry. Bubble size and bubble velocity are critical parameters which govern the interfacial transport phenomena and play an important role in gas-solid contact. These characteristics affect the operating parameters as well as the design of equipment in industrial applications.

Non-Newtonian, Shear-thickening fluids have been studied extensively due to their immense potential for commercial use in shock absorbing and force damping applications, such as liquid body armor, sports and personal protection. Furthermore, a better understanding of shear-thickening fluid is pertinent to industrial processing for enhancing flow, preventing the breakage or clogging of mixing equipment, and preventing clogging in narrow orifices. Despite their significance, many aspects of the flow of these non-Newtonian fluids remain poorly understood.

In the first part of this dissertation, we study the dynamics of rising bubbles in three dimensional fluidized beds using computational fluid dynamics-discrete element method (CFD-DEM) to shed light on the physics underpinning phenomena uncovered previously using magnetic resonance imaging (MRI). We were able to understand the underlying mechanism behind the anomalous collapse of a bubble in side-by-side injection as well as an alternating asynchronous pinch-off pattern due to jet interaction in a fluidized bed by looking into the gas streamlines and the drag force on the particles.

In the second part of this dissertation, we study dynamics of rising bubbles in Newtonian fluids and non-Newtonian cornstarch-water suspensions experimentally using optical imaging. We were able to identify that Capillary number (Ca) is a key dimensionless parameter governing the regimes of interacting jets in water. We also observed a periodic coalescence of bubbles at the same points in space in cornstarch-water suspensions and attributed this behavior to leading bubbles entering a shear thickening regime. Further, we identified the key dimensionless parameters for wobbling behavior of single bubbles in cornstarch suspensions to be Bond (Bo), and Reynolds (Re) number, regardless of the bubble being in a Newtonian or a shear-thinning regime. We believe our findings can be applied in industry to optimize the mass transport and liquid mixing for a range of applications.

Table of Contents

List of Figures iv

List of Tables xii

Acknowledgments xiii

Dedication xiv

Chapter 1 : Introduction 1

1.1 Background and Motivation 1

1.2 Description of the chapters and their relevance 3

Chapter 2 : Collapse of a Bubble Injected Side-by-Side with Another Bubble into an Incipiently Fluidized Bed: A CFD-DEM Study 8

2.1 Introduction 8

2.2 Methods 10

2.2.1 CFD-DEM simulations 10

2.2.2 Fluidized Bed 12

2.2.3 Bubble Injection 12

2.2.4 MRI Measurements 13

2.2.5 Image Processing 14

2.3 Results and Discussion 14

2.4 Conclusion 21

Chapter 3 : An Asynchronous Bubble Pinch-Off Pattern Arising in Fluidized Beds due to Jet Interaction: A Magnetic Resonance Imaging and Computational Modeling Study 22

3.1 Introduction 22
3.2 Methods 24
3.2.1 Fluidized Bed 24
3.2.2 Jet and bubble injection 25
3.2.3 MRI Measurements 26
3.2.4 Numerical Simulations 26
3.3 Results and Discussion 28
3.3.1 MRI Results 28
3.3.2 Simulation Results 33
3.4 Discussion 39
3.4.1 Proposed Mechanism for Asynchronous, Out-of-Phase Bubble Pinch-Off 39
3.4.2 Comparison with Prior Work 42
3.5 Conclusion 46
Chapter 4 : Characterizing Alternating Bubbles Emerging from Two Interacting Vertical Gas Jets in a Liquid 48
4.1. Introduction 48
4.2 Experimental Methods and Image Processing 50
4.3 Results and Discussion 52
4.3.1 Identification and Quantification of Regimes of Jet Interaction 52
4.3.2 Harmonic Oscillator Model 61
4.3.3 Comparison with Prior Research 67
4.4 Conclusion 72
Chapter 5 : Periodically Structured Coalescence of Bubbles in a Shear-Thickening Suspension. 74

5.1 Introduction 74
5.2 Methods 75
5.3 Results and Discussion 76
5.4 Conclusion 83
Chapter 6 : Dynamics of Single Bubbles in Cornstarch-Water Suspensions 85
6.1 Introduction 85
6.2 Experimental Methods 87
6.3 Results and Discussion 89
6.4 Conclusion 99
Chapter 7 : Conclusion and Future Work 101
References 104

List of Figures

Figure 2.1. Schematic copied from the prior experimental study [29], showing the proposed mechanism for bubble collapse, with one bubble starting out slightly smaller than the other and decreasing in size until collapse because a smaller amount of gas flow (shown in red arrows) channels to the smaller bubble, making it unable to maintain the shape of its roof. 9

Figure 2.2. Horizontal cross-section of the CFD mesh used, marking in green the cells used for the central vertical slice through the bed and in red the cells at the bottom of the fluidized bed through which gas was injected to inject bubbles into the bed. 13

Figure 2.3. Time series of images of the void fraction through a central slice of the fluidized bed with side-by-side bubbles injected for 30 ms from (a) MRI experiments from a prior study with gas injection velocity ~160 m/s through both ports (volumetric flow rate of 0.008 m^3/s through each port), spatial resolution of 3 mm (horizontal) × 3 mm (vertical) with a 10 mm slice and (b) CFD-DEM simulations conducted here with CFD grid size of 9.375 mm, the gas injection velocity of 60 m/s through the left port (volumetric flow rate of 0.0049 m^3/s) and 65 m/s through the right port (volumetric flow rate of 0.0053 m^3/s). 15

Figure 2.4. Time series of 3D renderings of CFD cells from a top view of the fluidized bed showing bubbles rising in the same CFD-DEM simulation shown in Figure 3(b). 16

Figure 2.5. Images of gas velocity surrounding bubbles for the same CFD-DEM simulation as shown in Figure 3 (b) with CFD grid size of 9.375 mm. (a) shows the void fraction and (b) shows the gas speed; both (a) and (b) show a central vertical slice and use arrows

to indicate gas velocity. (c) shows a 3D perspective outlining the bubbles and showing streamlines of gas flowing through the bubbles. 17

Figure 2.6. Time series of images of (a) void fraction, (b) gas speed and (c) a 3D perspective of bubbles with green arrows and lines indicating gas flow in a central vertical plane from a CFD-DEM simulation with CFD grid size of 9.375 mm and bubbles injected side-by-side for 30 ms with a 65 m/s gas injection velocity through both ports. 18

Figure 2.7. Bubble volume vs time for two bubbles injected side by side (L = left, R = right) for 30 ms with different gas injection velocity. (a) The total bubble volume from both the right and left bubbles and (b) the individual volume of each bubble. 20

Figure 3.1. Horizontal cross-section view of the fluid grid used for (a) 1 mm particles and (b) 3 mm particles, with the green slice showing CFD cells used in vertical cross-section images and the red squares showing the two ports for jet injection at the gas distributor. 28

Figure 3.2. Time series of images of particle concentration (upper row) and particle velocity (lower row) of a central vertical slice through the bed of two gas jets separated by $d_{sep}/d_o = 5.0$ injected into an incipiently fluidized bed of 1 mm particles with an average gas velocity through each orifice of u_{jet} = (a) 38 m/s, (b) 66 and (c) 97 m/s. 30

Figure 3.3. Time series of images of particle concentration (upper row) and particle velocity (lower row) of a central vertical slice through the bed of a single central jet injected into an incipiently fluidized bed of 1 mm particles with an average gas velocity through the orifice of u_{jet} = 52 m/s. 31

Figure 3.4. Time series of images of particle concentration (upper row) and particle velocity (lower row) of a central vertical slice through the bed of two gas jets separated by dsep/do

=10.1 injected into an incipiently fluidized bed of 1 mm particles with an average gas velocity through each orifice of ujet = 38 m/s. 32

Figure 3.5. Time series of images of particle concentration (upper row) and particle velocity (lower row) of a central vertical slice through the bed of two gas jets separated by d_{sep}/d_o = 5.0 injected into an incipiently fluidized bed of 3 mm particles with an average gas velocity through each orifice of u_{jet} = 97 m/s. ...33

Figure 3.6. Time series of images of jet interaction in 1 mm particles showing particle concentration (a,c) and horizontal particle velocity (b,d) from MRI measurements (a,b) and CFD-DEM simulations (c,d). MRI Jet velocity: 97 m/s; CFD-DEM jet velocity: 3 m/s. 34

Figure 3.7. Time series of images of jet interaction in 1 mm particles from CFD-DEM simulations showing 3D renderings of voids near the orifices from (a) a front view and (b) a top view.....35

Figure 3.8. Time series of images of jet interaction in 1 mm particles from CFD-DEM simulations showing (a) particle concentration, (b) horizontal gas velocity, (c) horizontal drag force normalized by particle weight and (d) horizontal particle velocity. Jet velocity: 3 m/s. 36

Figure 3.9. Time series of images of jet interaction in 3 mm particles showing particle concentration (a,c) and horizontal particle velocity (b,d) from MRI measurements (a,b) and CFD-DEM simulations (c,d). MRI Jet velocity: 97 m/s; CFD-DEM jet velocity: 40 m/s. 37

Figure 3.10. Time series of images of jet interaction in 3 mm particles from CFD-DEM simulations showing (a) particle concentration, (b) horizontal gas velocity, (c) horizontal drag force

normalized by particle weight and (d) horizontal particle velocity. Jet velocity: 40 m/s. 39

Figure 3.11. Schematic of the mechanism underlying the alternating asynchronous bubbling patter. Red arrows indicate the motion of particles.....41

Figure 4.1. Grayscale image of bubbles emerging from interacting gas jets, showing in red boxes the regions used to evaluate signal intensity to determine bubble formation and breakoff at each orifice. 52

Figure 4.2. (a) Time series of images showing bubbles rising from two orifices through silicone oil with μ = 0.096 Pa s; dsep/do = 4.4; flow rate = 1.5 L/min. (b) Signal intensity of the liquid in a region near the left and right orifices over 150 ms processed from the images for the case shown in (a). (c) Fourier transform (FT) of Fig. 2 (b) over a time frame of 120 s for both orifices with vertical lines showing the dominant frequency for bubble breakoff from each orifice. (d) Cross-correlation of the area curves over the time frame of 120 s with the time delay normalized by the average of the dominant bubble breakoff frequencies for the left and right orifices (27 Hz). 53

Figure 4.3. (a) Time series of images showing bubbles rising from two orifices through silicone oil with μ = 9.71 Pa s; d_{sep}/d_o= 4.4; flow rate = 0.2 lpm. (b) Signal intensity of the liquid in a region near the left and right orifices over 3 s processed from the images for the case shown in (a). (c) Fourier transform (FT) of (b) over a time frame of 120 s for both orifices with a vertical line showing the dominant frequency for bubble breakoff. (d) Cross-correlation of the area curves over the time frame of 120 s with the time delay normalized by the dominant bubble breakoff frequency (0.42 Hz). 54

Figure 4.4. (a) Time series of images showing bubbles rising from two orifices through silicone oil with μ = 0.096 Pa.s; d_{sep}/d_o= 17; flow rate = 1.5 lpm. (b) Signal intensity of the liquid in a region near the left and right orifices over 150 ms processed from the images for the case shown in (a). (c) Fourier transform (FT) of (b) over a time frame of 120 s for both orifices with a vertical line showing the dominant frequency for bubble breakoff. (d) Cross-correlation of the area curves over the time frame of 120 s with the time delay normalized by the dominant bubble breakoff frequency (11 Hz). 55

Figure 4.5. (a,c) bubble breakoff frequency vs. Ca, (b, d) calculated bubble breakoff area (Eq. 1) vs. Ca for two jets at (a, b) 10 cm liquid depth and (c, d) 40 cm depth.....58

Figure 4.6. Cross correlation ratio vs. effective bubble diameter normalized by separation distance ($\boldsymbol{Db,eff/dsep}$) for (a, b) low viscosity fluids and (c, d) high viscosity fluids and liquid depths of (a, c) 10 cm and (b, d) 40 cm. Data for water and silicone oils are shown. 60

Figure 4.7. Schematic time series of bubble breakoff images demonstrating the proposed physical mechanism creating the alternating bubble breakoff phenomenon. Adapted from Penn et al. [31]. 62

Figure 4.8. A schematic diagram of the coupled harmonic oscillator model.....63

Figure 4.9. Model results for positions of the two masses with different values the ratio of inner and outer spring constant used. Model parameters used: $\boldsymbol{m}$ = 0.1 kg; $\boldsymbol{cin}$ = 5 kg/s; $\boldsymbol{cout}$ = 5 kg/s; $\boldsymbol{\phi 1 - \phi 2}$ = 1.05π; $\boldsymbol{\omega 0}$ = 104 s-1. Black solid line: $\boldsymbol{kout}$ = 100 kg/s^2; $\boldsymbol{kin}$ = 100000 kg/s^2. Blue dotted line: $\boldsymbol{kout}$ = 100 kg/s^2; $\boldsymbol{kin}$ = 1000 kg/s^2. The lines oscillating between 0 to 4 cm represent the positions of m_2, whereas the lines oscillating between 0 to -4 cm represent the positions of m_1.....64

Figure 4.10. $S_{0.5}/S_0$ vs. ABD for low viscosity liquid data for (a) 10 cm and (b) 40 cm liquid height. (c-d) ABD vs. $D_{b,eff}/d_{sep}$ for the data of Dzienis et al. [102] as well as the low viscosity liquid data from this study for liquid heights of (c) 10 cm and (d) 40 cm. 69

Figure 4.11. (a) Alternating vs. non-alternating bubbling patterns as a function of $D_{b,eff}/d_{sep}$ for the data of Dzienis et al. [102]. (b) $D_{b,eff}/d_{sep}$ vs. Ca for the data of Dzienis et al. [102] as well as the low viscosity liquid data acquired for this study. 71

Figure 4.12. Schematic of injection setup for (a) this paper and (b) Dzienis *et* al. [102] paper. .. 71

Figure 5.1. Characterization of bubbling from an air jet in a 40 vol% cornstarch-water suspension with Fr = 25. (a) Average bubble area vs. bubble vertical position, showing the standard deviation with the dotted lines and highlighting Regions 1 and 2 of bubble coalescence in red. (b) FTs of bubble coalescence vs. time plots in the two regions, indicating the dominant frequency of bubble coalescence in each region. (c) Time series of images of bubble dynamics shown with a frequency of 7.4 Hz, circling points of periodic coalescence in three vertical regions. Under these flow conditions, bubbles formed at the nozzle at a frequency of approximately 15 Hz. 77

Figure 5.2. Bubble area vs. vertical bubble position for a 40 vol% cornstarch-water suspension at Fr = 25 (black line) as compared with other flow conditions: (a) different gas flow rates, same 40 vol% suspension (b) different vol% of cornstarch, same Fr (c) a density-matched 40 vol% cornstarch suspension, same Fr and (d) silicone oil with a viscosity of 0.096 Pa s, same Fr. 79

Figure 5.3. (a) FT of bubble breakthrough for the same regular coalescence case shown in Fig. 1. (b) Time series of images of bubbling for the same case shown at a frequency of 1.9 Hz. 80

Figure 5.4. Correlation coefficient vs. Fr for a variety of fluid conditions: cornstarch suspensions with vol% of (i) 10, (ii) 20, (iii) 30, (iv) 40, and (v) 44, (vi) a density-matched 40 vol% cornstarch suspension and (vii) silicone oil with viscosity of 0.096 Pa s.....81

Figure 5.5. Dynamics of leading and trailing bubbles at points in time just prior to bubble coalescence for the regular bubble coalescence case shown in Figs. 5.1 and 5.3. (a) Effective viscosity vs. shear rate for the suspension (line) and approximated shear rate of fluid surrounding the leading bubble just prior to coalescence (markers). Average vertical bubble acceleration (b,c) and average bubble rise velocity (e,f) vs. time before coalescence in Region 1 (b,e) and Region 2 (c,f). (d) Average bubble widths just before coalescence in the two regions. 82

Figure 5.6. Normalized bubble area vs. vertical bubble position for a 40 vol% cornstarch-water suspension for (a) bubbles injected at a frequency of 15 Hz with varying bubble injection time, forming initial bubbles of different areas and (b) bubbles injected for the same amount of time but different idle time between injections, creating bubbles at different frequencies. 83

Figure 6.1. Bubble rise shape and trajectory at 5 psi: (a) 0%, (b) 5%, (c) 10%, (d) 20%, (e) 30%, (f) 40%, (g) silicone oil 9.3 mPa s, (h) silicone oil 96 mPa s. 90

Figure 6.2. Bubble rise shape and trajectory at 15 psi: (a) 0%, (b) 5%, (c) 10%, (d) 20%, (e) 30%, (f) 40%, (g) 44%, (h) silicone oil 9.3 mPa s, (i) silicone oil 96 mPa s.....91

Figure 6.3. Bubble rise shape and trajectory at 25 psi: (a) 0%, (b) 5%, (c) 10%, (d) 20%, (e) 30%, (f) 40%, (g) 44%, (h) silicone oil 9.3 mPa s, (i) silicone oil 96 mPa s.....92

Figure 6.4. Bubble orientation (first row) and rise velocity (second row) for the (a,d) 5 psi, (b, e) 15 psi and (c,f) 25 psi injection pressures.....94

Figure 6.5. Amplitude of oscillation in rise velocity normalized by the average rise velocity vs. (a) Re, (b) Bo, (c) Mo, (d) Ca, (e) St and (f) Ro on a log-log scale. 96

Figure 6.6. Shape regimes for bubbles through liquids in our study plotted on the regime map of Grace et al. [154], using the black dividing lines of the prior work.....97

Figure 6.7. Experimentally measured effective viscosity vs shear rate for cornstarch-water suspensions with markers showing the approximate viscosity in the fluid surrounding the bubbles for each condition. 99

List of Tables

Table 2.1. Discrete element model (DEM) parameters used in CFD-DEM simulations.....11

Table 2.2. CFD parameters used in CFD-DEM simulations.....12

Acknowledgments

First and foremost, I would like to express my sincere gratitude to my wonderful advisor, Prof. Chris Boyce for letting me fulfill my dream of being a PhD student in his lab at Columbia University. The completion of this study could not have been possible without his expertise and guidance. He has always shown me support, respect, and trust. His genuine interest in mentorship and passion for discovering scientific phenomena always inspired me to dive deeper into every project. Second, I would like to thank Boyuan Chen, an outstanding undergraduate student in our research group for his significant help in modeling and data processing for Chapters 4 and 5 in this dissertation. His eagerness in doing research and intelligence in finding a solution for any given problem is admirable. Third, I would like to thank the rest of the current and previous members of Boyce lab for their help and great ideas in different projects, including Qiang Guo, Wasif Zia, Alireza Bordbar, Jagan Mohan, Amana Mohiuddin, Yuxuan Zhang, Kenan Xi, Shaohan Xu, Tom Kovar, Sean Kim, Yijin Li, Zhongsheng Sang and Carolina Vazquez. Fourth, I would like to thank William Hunnicutt, the manager of Carleton Laboratory for his experimental help with the rheological measurements. Fifth, I would like to thank my friends for all their support and care in this journey including Sara Hamilton, Aylin Kulur, Cisem Nurhan, Seda Sarp, John Vardner, and Steven Denny. Last but not least, I would like to thank my husband, Prof. Bobak Mosadegh and my parents for having faith in me, encouraging me to do my best, and supporting me unconditionally to be the person who I wanted to be.

Dedication

This dissertation is dedicated to my brilliant, loving husband, Bobak Mosadegh, my always encouraging, ever faithful parents, and all my other family members who always supported me throughout my education.

Chapter 1 : Introduction

1.1 Background and Motivation

A wide variety of processes in nature and industry involve bubbles rising through complex fluids, and they have shown fascinating properties which have inspired scientists to study them fundamentally. These bubbly flows are involved in degassing on the ocean floor [1], [2], giant bubbles rising and bursting in volcanoes [3], and chemical and bio reactors [4], such as fluidized beds and bubble columns used in production of fuels and polymers, nuclear power plants, water and wastewater treatment, carbon capture, and many other applications [5]. Therefore, due to the wide application of these systems, especially in chemical engineering field, we are interested in studying bubble dynamics in complex fluids as well as the rheological behavior of these fluids. Both aspects have a significant impact on the mixing of fluids, heat and mass transfer, and chemical reactions in both industrial processes and nature.

The presence of bubbles and particles affects the behavior and response of complex multiphase fluids. In fact, most fluids exhibit non-Newtonian behaviors under certain flow conditions. Even in complex fluids composed of Newtonian components, the coupling between different components and the evolution of internal boundaries often lead to complex rheology. Unlike bubbles in Newtonian fluids which tend to grow as they rise and proceed toward a final shape and terminal velocity [6], bubbles in non-Newtonian fluids can oscillate in rise velocity [7], [8] and shape [9], [10], and also, they can form complex shapes not seen in Newtonian fluids [10], [11], [12]. A number of computational and analytical studies of bubble dynamics in non-Newtonian fluids exist [8], [13], [14]; however, insights from them are somewhat limited due to an inability for models to capture the full rheological behavior of certain non-Newtonian fluids, particularly dense suspensions [15]. Thus, the dynamics of bubbles in both Newtonian and non-

Newtonian fluids is of crucial importance for understanding the effects of the rheological behavior of complex fluids.

Also, the dynamics of rising bubbles in a fluidized bed is different from that of bubbles in Newtonian fluids since there is no surface tension between the gas phase and the fluidized particles, and gas travels freely between the bubbles and the interstices between particles. Experimental studies of bubble dynamics in fluidized beds have been limited by difficulties in characterizing the granular flow around bubbles injected into opaque 3D systems. Previously, the most popular techniques used to study these systems have been particle image velocimetry [16], [17], tracer particle techniques, such as positron emission particle tracking [18], [19], and tomographic techniques, such as X-ray [20], [21] and electrical capacitance tomography [22]. Although these methods still provide valuable insight into the physics governing gas-solid fluidized beds, they are still very limited relative to modern techniques. In the past decade, magnetic resonance imaging (MRI) has proven to be a powerful technique, which can overcome many of the limitations of these other measurement methods by enabling real-time imaging of particle flow fields in granular flows and visualizing the rise of bubbles through particles. Another way to overcome the experimental limitation is the use of computational modeling of fluid-particle flow. In order to model fluid-particle flow, a granular flow model must be coupled with a computational fluid dynamics (CFD) model. On a small scale, CFD cells much smaller than the particle size can be used, such that the no-slip boundary condition can be resolved without the need for closure relationships, in a technique referred to as particle-resolved direct numerical simulation (PR-DNS) [23], [24]. In order to simulate laboratory-scale fluidized beds, a technique referred to as CFD-DEM [25] tracks the motion of each particle using DEM, but it models fluid flow using CFD with cells larger than the particle; this technique requires a drag law to couple fluid and particle flow [11], [12]. To

model laboratory- and industrially-sized systems, a technique referred to as two-fluid modeling (TFM) models both particles and fluid as interpenetrating continua on the same CFD grid [28]. However, this method struggles to describe flows with densely packed particles as well as complex inter-particle forces.

Here we seek to study the bubble dynamics and the flow field surrounding bubbles in fluidized beds (granular media) and dense suspensions composed of cornstarch and water computationally and experimentally, respectively. CFD-DEM simulations of fluidized beds will provide detailed information on the forces on each particle, allowing for insights into the mechanisms driving particle and fluid motion. Optical imaging experiments of bubbly flows in dense suspensions will provide critical insights into flow aspects driving oscillatory rise and the shape of bubbles in non-Newtonian fluids, as well as phenomena seen in bubble rise behavior from gaseous jet in a dense suspension due to shear-thickening effects. The quantitative measurements will provide a strong set of data to challenge analytical, computational and rheological models of these non-Newtonian fluids. Further, the results will enable understanding of how bubbles affect mixing and transport dynamics in fluid, key parameters for developing industrial systems and understanding natural phenomena.

1.2 Description of the chapters and their relevance

In Chapters 2 and 3, the interaction between bubbles and gas jets in fluidized beds were studied computationally using CFD-DEM to shed light on the phenomena uncovered in experimental magnetic resonance imaging work by Boyce et. al [29], validate hypotheses from their work, and reveal the physical mechanisms behind the interaction of the bubbles and jets in a 3D fluidized bed. Both of these Chapters are published in Physical Review Fluids [30], [31]. The results from Chapter 3 were a great motivation to study how gas jets interact in a Newtonian fluid.

Therefore, in Chapter 4, we investigate regimes of bubbling occurring due to the interaction of two vertical gas jets into Newtonian liquids. A simplified coupled harmonic oscillator model is proposed which captures the alternating bubbling regime. This Chapter is published in Chemical Engineering Science [32]. After studying the bubble and jet interaction in fluidized beds and Newtonian fluids, there was a motivation to investigate how bubbles interact with each other in a non-Newtonian fluid in which bubble dynamics have not been studied before. Our research showed that bubble dynamics in cornstarch-water suspensions have complicated and interesting characteristics, and there is still a lot to discover about this suspension. In order to be able to study the bubble or gas jet interaction in a cornstarch-water suspension, it is important to first investigate the dynamics of a single bubble and a single gas jet in this media. Therefore, in Chapters 5 and 6, the dynamic behavior of a single gas jet, and a single bubble in a suspension of cornstarch-water were studied. Our study in Chapter 5 is in revision for Physical Review Letters, and our study in Chapter 6 is submitted to the Journal of Non-Newtonian Fluid Mechanics. Lastly, in Chapter 7, conclusions from all of the work along with potential future studies relevant to this thesis are discussed. In the following paragraphs, a brief description of each chapter is presented.

In Chapter 2, a CFD-DEM study was conducted to shed light on the prior magnetic resonance imaging study by Boyce et al. [29] and reveal the physical mechanism behind the collapse of a bubble which is injected side-by-side with another bubble into an incipiently fluidized bed. The Boyce et al. [29] study demonstrates that, below a critical injection volume, one bubble collapses, while the other bubble survives. However, limitations in their experimental measurements left open questions about the apparent collapse: (1) did the bubble actually collapse or rather move out of the imaging plane and (2) if the bubble collapsed, was it due to gas transfer between bubbles or a preference for gas to channel toward the surviving bubble. Here, we

demonstrate that computational fluid dynamics – discrete element method (CFD-DEM) simulations can predict this phenomenon. Simulation results reveal that the bubble does in fact collapse and that this collapse occurs because the slight size difference between the two bubbles causes gas flow to channel preferentially to the larger bubble, leaving the smaller bubble without enough gas flow to support its roof.

In Chapter 3, another CFD-DEM study was conducted to compare with an experimental magnetic resonance imaging study in conducted previously in Zurich on the pinch-off pattern of two gas jets injected into a 3D incipiently fluidized bed. Experiments conducted by Penn et al. [33] revealed that at large separation distances and in cases with larger particles, bubbles pinch off from the two jets simultaneously with one another. At small separation distances with smaller particles, a jet grows at one orifice while a jet pinches off to form a bubble at the other orifice, resulting in bubbles pinching off from the two jets nearly completely out-of-phase from one another. Our CFD-DEM could reproduce both the simultaneous and asynchronous (out-of-phase) pinch-off patterns. These simulations demonstrate that the asynchronous pattern emerges due to drag forces on the particles causing particle inertia dominate over momentum dissipation, causing motion of particles between the jets to become unstable. Specifically, when one jet is growing, it forces particles to move toward the neighboring jet, causing a bubble to break off from the neighboring jet.

In Chapter 4, optical imaging experiments were conducted to investigate regimes of bubbling when two vertical gas jets are injected into liquids. Three regimes were identified (i) bubbles break off from jets independently of one another, (ii) bubbles coalesce and break off from jets at the same time and (iii) bubbles break off from jets in an alternating pattern, nearly 180 degrees out-of-phase from one another. We identify that a mixed capillary number is key to determining the size of bubbles. Further, we find that the ratio of bubble diameter at breakoff to

separation distance between jets is key to determining the regime of bubble breakoff. The alternating pattern is attributed to a growing jet pushing liquid between the two jets towards the second jet, such that the second jet pinches off, forming a bubble. This mechanism is used to formulate a simplified coupled harmonic oscillator model which captures alternating bubbling.

In Chapter 5, we report periodic coalescence of bubbles at the same points in space from a single gas jet injected vertically into a 40 vol% cornstarch-water suspension at a specific Froude number. This regular coalescence is not observed at other conditions, such as different Froude numbers, volume fractions of cornstarch, density-matched suspension, or in a Newtonian fluid with comparable viscosity. We were also able to create this structured bubble coalescence by injecting bubbles in a consecutive fashion using solenoid valves. In this method, we varied the injection time and the time interval between each injection systematically and observed controllable periodic coalescence of bubbles. We attribute the regular bubble coalescence to the rheology of the suspension since the leading bubbles entering a shear-thickening regime, while trailing bubbles are in a shear-thinning regime, leading to coalescence.

In Chapter 6, we conducted optical imaging experiments to investigate the shape and rise behavior of a single bubble in a cornstarch-water suspension at different packing fractions with comparison to Newtonian fluids with comparable viscosities. Quantification of the amplitude of velocity oscillation reveals that intermediate Bo and high Re are the key dimensionless parameter conditions for producing wobbling bubbles which oscillate in orientation and rise velocity. With increasing viscosity and bubble size, wobbling is suppressed, and bubbles tend to adopt spherical cap shape, except ellipsoidal bubbles form in 44 vol% suspensions. Shear-thinning conditions in suspensions were not able to create wobbling conditions in high Bo or low Re conditions tested here.

In chapter 7, we discuss the highlights of this study, potential future studies, and how the insights from this study can be applicable to a variety of industrial systems and natural phenomena.

Chapter 2 : Collapse of a Bubble Injected Side-by-Side with Another Bubble into an Incipiently Fluidized Bed: A CFD-DEM Study

This chapter was published previously in the following article:

A. Padash and C.M. Boyce "Collapse of a bubble injected side-by-side with another bubble into an incipiently fluidized bed: A CFD-DEM study," *Phys. Rev. Fluids*, vol. 5, no. 3, 34304, 2020.

2.1 Introduction

Voids or "bubbles" in fluidized granular beds create fascinating scientific questions due to their similarities in shape and rise behavior to bubbles in conventional fluids, despite the fact that there is no interface or surface tension between the void and particle-laden regions and gas passes freely between both regions [34], [35]. Further, bubbles are critical to a variety of industrial processes involving fluidized beds, since bubbles are the main cause of particle mixing and convection, promoting uniform temperature, and bubbles provide a path for gas to largely bypass interaction with particles, limiting gas-particle heat and mass transport [36]. Thus, bubbles in fluidized beds have been the attention of longstanding and focused study in engineering and physics.

Recently, Boyce et al. [29] published an experimental magnetic resonance imaging (MRI) study, reporting the collapse, or volume abruptly reaching zero, of a bubble injected into an incipiently fluidized bed when a neighboring second bubble was injected simultaneously. Prior studies have shown bubbles collapsing in systems with internal obstacles [37], but the findings of Boyce et al. [29] were the first demonstration known to the authors of bubble collapse related to bubble interaction. When two bubbles were injected simultaneously for the same period of time,

one bubble always collapsed and it varied randomly which of the two bubbles collapsed, suggesting the manifestation of an instability. Further, when only a single bubble was injected, the bubble did not collapse. As shown in Figure 2.1, reproduced from Boyce et al. [29], the authors hypothesized that bubble collapse occurred due to one bubble being slightly smaller than the other, and the smaller bubble receiving less flow through it than the larger bubble because the larger bubble provides a higher permeability to gas flow than the smaller one. As known since the landmark theoretical work of Davidson [34], gas bubbles require sufficient gas to flow through their roof to maintain their shape. Thus, without sufficient gas flow through its roof, the smaller bubble would decrease in size, and as it decreased in size, less and less gas would channel towards it, causing the decrease in size to continue until its collapse.

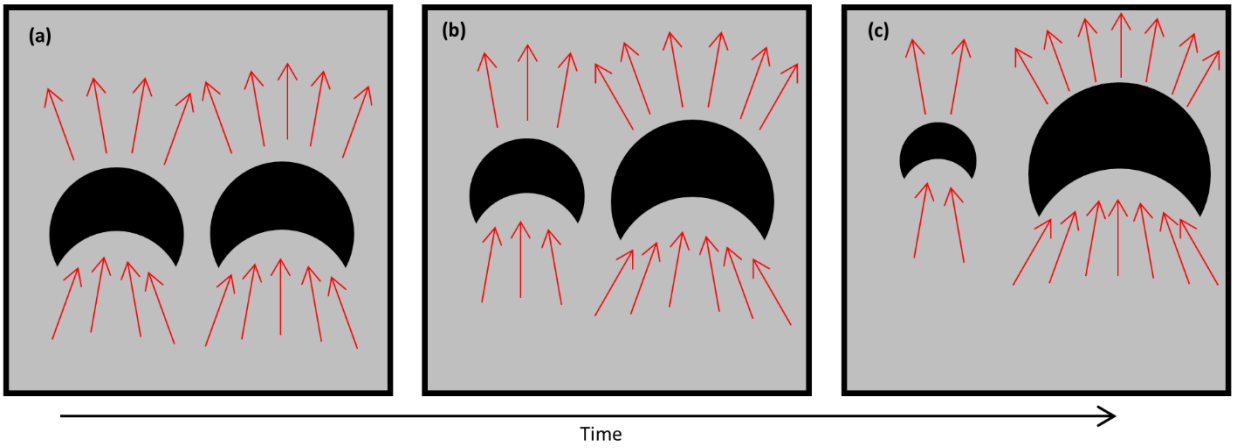

Figure 2.1. Schematic copied from the prior experimental study [29]**, showing the proposed mechanism for bubble collapse, with one bubble starting out slightly smaller than the other and decreasing in size until collapse because a smaller amount of gas flow (shown in red arrows) channels to the smaller bubble, making it unable to maintain the shape of its roof.**

This hypothesis for the mechanism underlying the observed collapse is physically sound; however, a number of questions and counterhypotheses surrounded the hypothesis which could not be addressed directly with MRI measurements:

1. Did the bubble actually collapse, or did it simply move out of the 2D MRI imaging plane in the 3D fluidized bed?
2. Does one bubble actually have to be smaller than the other for collapse to occur, since to the best control of the experiments the bubbles were the same size, and which bubble collapsed varied from experiment to experiment?
3. Is the mechanism actually related to gas channeling below the two bubbles, or could it be related to gas transfer from the collapsing to the surviving bubble more directly?

These questions largely stem from the fact that the MRI measurements were conducted in a single central plane and did not measure gas velocity. Here, we use Computational Fluid Dynamics – Discrete Element Method (CFD-DEM) [25] simulations, which model the motion of each individual particle using Newtonian and contact mechanics [38] and couple the particle motion to a CFD model of gas flow [39] via a drag law [40], to address these questions and identify the mechanism underlying bubble collapse.

2.2 Methods

2.2.1 CFD-DEM simulations

CFD-DEM simulations were conducted using the open source platform CFDEMcoupling [41], which models gas flow using the CFD software OpenFOAM [42] and models particle motion using the DEM software LIGGGHTS [43]. A full description of the equations used is described in a previous paper from the corresponding author [44].

The motion of each granular particle was modeled based on contact and Newtonian mechanics using DEM [38]. Table 2.1 summarizes the DEM parameters used. A Hertzian spring model was used for normal and tangential contacts with a coefficient of restitution set to 0.69, matching the experimental value. To avoid using excessively small DEM time steps, the particles

were simulated as being less stiff than they are in reality, which is used almost universally in CFD-DEM simulations and has been shown to not impact flow significantly [44]. Coulomb's law was used to account for sliding, with a coefficient of friction for particle-particle interactions of 0.56 based on the experimental value.

Table 2.1. Discrete element model (DEM) parameters used in CFD-DEM simulations

Parameter	Value
Tapped bed height, H_0	200 mm
Bed diameter, D_{bed}	190 mm
Particle shape	Spherical
Particle diameter, d_p	2.93 ± 0.04 mm
Particle density	1040 kg/m^3
Coefficient of restitution	0.69
Coefficient of inter-particle friction	0.56
Particle-wall friction coefficient	0.56
Poisson's ratio	0.32
Young's modulus	10 MPa
Spring model	Hertzian
DEM time step	0.001 ms

The gas phase was modeled as a continuum, using Computational Fluid Dynamics (CFD) with a discretized form of the volume-averaged fluid equations [39] used to solve for gas velocity and pressure on a co-located fluid grid. Table 2.2 summarizes the CFD parameters. To allow for longer CFD time steps, an incompressible code with an implicit solver was used. To match the cylindrical experimental geometry, an unstructured grid was used with rectangular cells used in the center of the system and wedge-shaped cells near the walls. Figure 2.2 shows a horizontal cross-section of the mesh used. The vertical-direction grid spacing was dz = 9.375 mm and dx = dy = 9.047 mm was used for the square grid cells far from the boundaries in the horizontal direction, between 3 and 4 particle diameters, matching recommendations for accurate and grid-

independent simulation results [45]–[47]. The two phases were coupled using the drag law of Wen & Yu [40].

Table 2.2. CFD parameters used in CFD-DEM simulations

Parameter	Value
Overall height of simulation	300 mm
Bed diameter, D_{bed}	190 mm
Fluid grid spacing	9.375 mm
Superficial velocity, U	0.70 m/s
Distance between injection ports	72.4 mm
Wall boundary condition	No slip
Outlet boundary condition	Constant pressure

2.2.2 Fluidized Bed

The fluidized bed simulated was identical to that used in the previous MRI experiment [29]: it was 190 mm in diameter and 300 mm in height. The particle diameter was 2.93 ± 0.04 mm, and density was 1040 kg/m^3, to match those measured for the experimental particles. The minimum fluidization velocity used to barely suspend the particles in both the experiments and the simulations was 0.70 m/s.

2.2.3 Bubble Injection

The simulated bubble injection setup was created to match that used experimentally as closely as possible. Through all cells in the base of the fluidized bed, except for two used for bubble injection, gas was flowed at a constant gas velocity equal to the minimum fluidization velocity to barely suspend the particles. This matches the experimental condition of gas injected uniformly at minimum fluidization conditions through a perforated plate except at the two orifices used for bubble injection. Bubbles were injected via two CFD cells highlighted in Figure 2.2, with gas velocity non-zero for 30 ms, to match that used in the experiments. Gas velocities were the same in the two orifices in one simulation, to simulate a condition in which the two bubbles were

equal in size, and slightly different in another simulation, to simulate one bubble being slightly smaller than the other. In the prior experiments, the bubble injection ports were separated by 80 mm and were circular with a diameter of 7.95 mm. In the simulations, the injection ports were 72.4 mm apart and were square in shape with side length 9.05 mm.

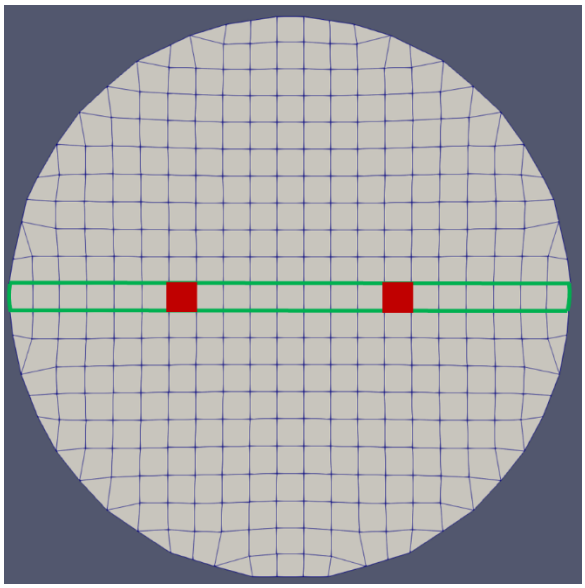

Figure 2.2. Horizontal cross-section of the CFD mesh used, marking in green the cells used for the central vertical slice through the bed and in red the cells at the bottom of the fluidized bed through which gas was injected to inject bubbles into the bed.

2.2.4 MRI Measurements

No MRI measurements were performed in this study, but we describe the details of the prior experimental study [29] briefly here and refer readers to other papers for fuller descriptions [29], [48]. Rapid imaging of granular flows was achieved using a combination of techniques, as described previously [48]. A specially built 16-channel radiofrequency coil [48] was placed around the fluidized bed and the entire system was placed in a Philip Achieve 3T MRI scanner. Echo planar imaging [49] with the SENSE algorithm [50] was used for rapid imaging of the particle concentration field. This was combined with phase contrast velocimetry [51] to achieve

rapid imaging of both the particle concentration and the particle velocity field. Images were taken of a central vertical slice through the fluidized bed with a slice thickness of 10 mm.

2.2.5 Image Processing

Images of simulation data of void fraction and gas velocity were produced using Matlab and Paraview. Images of void fraction and gas velocity for a 2D central vertical slice (highlighted in Figure 2) were produced by importing simulation data into Matlab. Images in 3D were produced in Paraview by applying a filter to only show CFD cells in which the void fraction was above 0.8 to show the bubbles and using the "streamline" feature to convert the gas velocity field output by the simulation into streamlines.

2.3 Results and Discussion

Figure 2.3 shows (a) MRI measurements [29] and (b) CFD-DEM simulation predictions of the void fraction over time through a central vertical slice in a case in which both bubbles are injected for 30 ms and the left bubble collapses. In the MRI measurements (a), both bubbles had identical injection conditions, and thus the expectation is that the same amount of gas is injected through both ports and bubbles are equal in size. However, image processing of the MRI data in the previous study shows that the left bubble was actually a bit smaller than the right bubble [29]. Thus, in the CFD-DEM simulations, the gas in the left bubble was injected at 60 m/s, while that in the right bubble was injected at 65 m/s, making the left bubble slightly smaller than the right bubble. The injection velocities were different for CFD-DEM and MRI measurements, due in part to the larger area of the simulated injection ports, and the simulated bubbles rose at different velocities than the experimental bubbles with somewhat different shapes. Nevertheless, the simulations qualitatively reproduce the apparent bubble collapse phenomenon, providing confidence in the validity of the model in addition to the multitude of other studies validating CFD-

DEM simulations against experiments [24], [25], [44], [52]–[54]. Figure 2.3 demonstrates that CFD-DEM can reproduce the apparent bubble collapse phenomenon observed experimentally; however, the question still remains if the left bubble actually collapsed or if instead it just moved out of the imaging plane. While the CFD-DEM simulations reproduce the collapse phenomenon, the bubbles rise and collapse in the CFD-DEM simulation is significantly more rapidly than in the MRI experiments. The authors attribute this to quantitative inaccuracies in CFD-DEM simulations, most likely introduced by the use of a drag law to couple gas and solids flow, as it has been shown in previous studies [44], [45] that changing drag laws strongly affects bubble dynamics. These inaccuracies could be avoided by using a smaller CFD grid and directly coupling gas-solid flow via the no-slip boundary condition; however, this would be prohibitively computationally expensive.

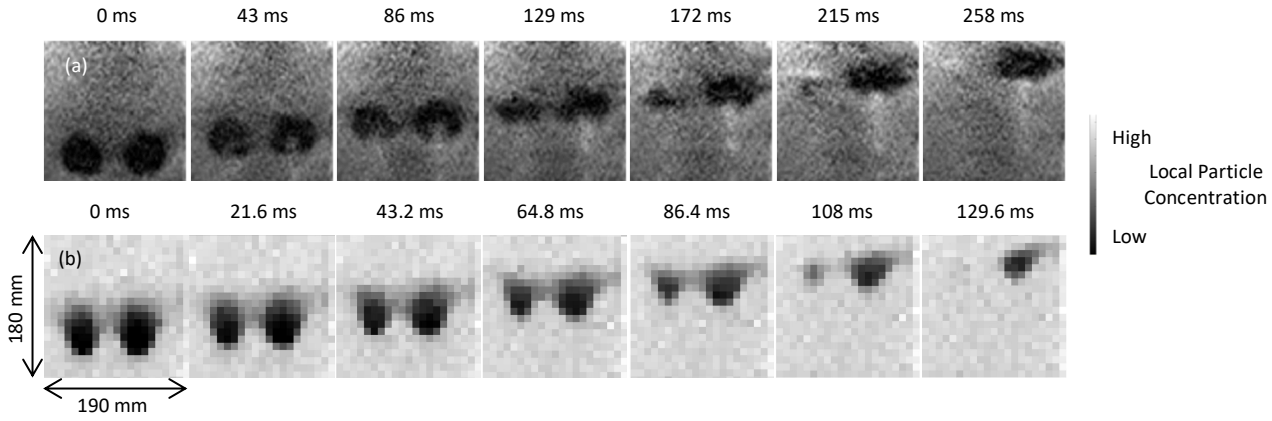

Figure 2.3. Time series of images of the void fraction through a central slice of the fluidized bed with side-by-side bubbles injected for 30 ms from (a) MRI experiments from a prior study with gas injection velocity ~160 m/s through both ports (volumetric flow rate of 0.008 m^3/s through each port), spatial resolution of 3 mm (horizontal) × 3 mm (vertical) with a 10 mm slice and (b) CFD-DEM simulations conducted here with CFD grid size of 9.375 mm, the gas injection velocity of 60 m/s through the left port (volumetric flow rate of 0.0049 m^3/s) and 65 m/s through the right port (volumetric flow rate of 0.0053 m^3/s).

Figure 2.4 shows images from the same simulation as in Figure 2.3 (b), but this time showing a top view of the bubbles in 3D as they rise over time. Figure 2.4 demonstrates that the left bubble does in fact collapse, and neither bubble moves out of the central plane.

Figure 2.4. Time series of 3D renderings of CFD cells from a top view of the fluidized bed showing bubbles rising in the same CFD-DEM simulation shown in Figure 3(b).

To address the question of the mechanism causing bubble collapse, Figure 2.5 shows simulation predictions for the same simulation as in Figure 2.3 (b), but showing (a) the void fraction and (b) the gas speed field in a central vertical slice with gas velocity indicated by arrows. Figure 2.5 (c) provides a 3D perspective of the gas flow surrounding the bubbles, with streamlines indicating the gas flow as the bubbles rise over time. These results demonstrate that gas flow below the bubbles is channeled into both bubbles, with more gas flow channeled into the right bubble than the left bubble. This channeling of gas flow is expected due to the higher permeability of bubbles to gas flow than the particulate phase, and greater channeling through the larger bubble can be explained by larger bubbles providing an even easier path for gas to permeate through the fluidized bed. Channeling of gas through bubbles is expected based on Davidson's theory [34] for gas flow around a single bubble, and this theory also demonstrated that this gas flow through the roof of the bubble, not arching, is what allows the bubble roof to maintain its shape as it rises.

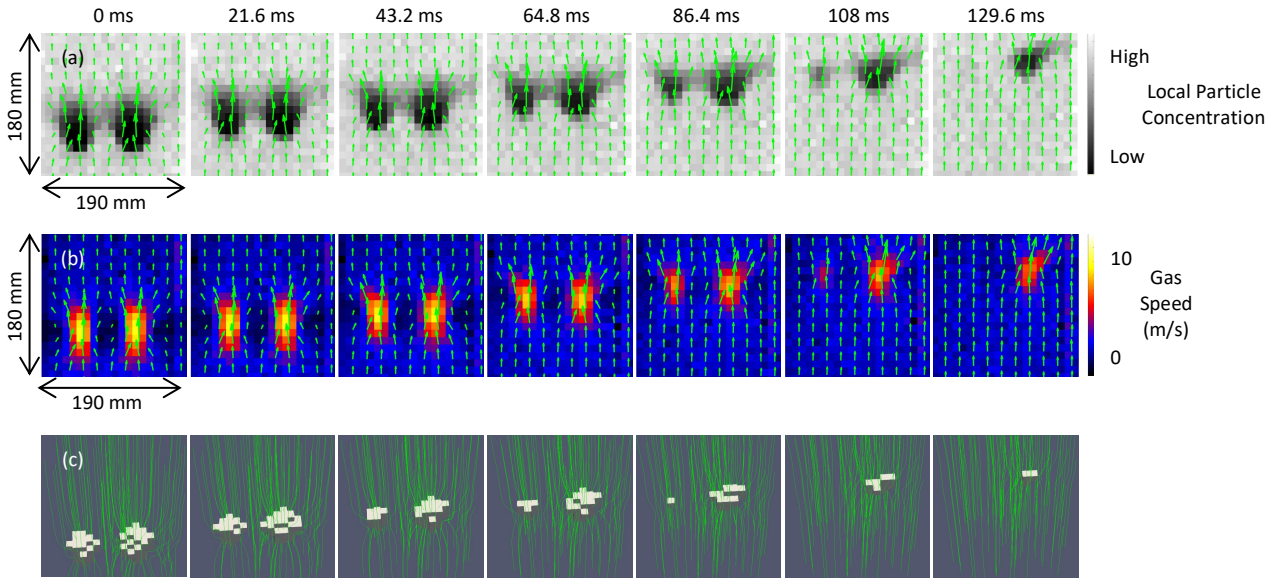

Figure 2.5. Images of gas velocity surrounding bubbles for the same CFD-DEM simulation as shown in Figure 3 (b) with CFD grid size of 9.375 mm. (a) shows the void fraction and (b) shows the gas speed; both (a) and (b) show a central vertical slice and use arrows to indicate gas velocity. (c) shows a 3D perspective outlining the bubbles and showing streamlines of gas flowing through the bubbles.

To address the question of whether or not a smaller bubble is needed for a bubble to collapse, Figure 2.6 shows simulation prediction for bubble injection where both bubbles are injected at 65 m/s. In this case, both bubbles form at the same size and rise through the bed without collapsing, indicating that a mismatch in bubble size is critical to collapse. Also, the simulation results show that the collapse phenomenon only occurs when the extent of size difference is beyond a critical value. When the gas injection velocities in the left bubble and right bubbles are 63 m/s and 65 m/s respectively, both bubbles rise through the bed and no collapse occurs.

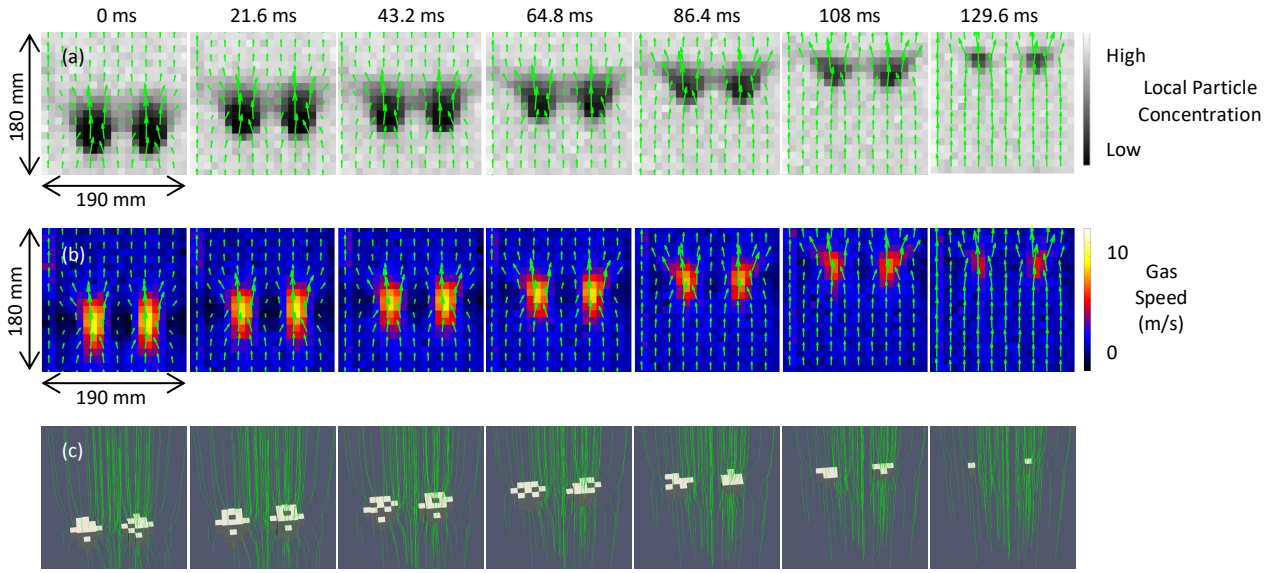

Figure 2.6. Time series of images of (a) void fraction, (b) gas speed and (c) a 3D perspective of bubbles with green arrows and lines indicating gas flow in a central vertical plane from a CFD-DEM simulation with CFD grid size of 9.375 mm and bubbles injected side-by-side for 30 ms with a 65 m/s gas injection velocity through both ports.

Figure 2.7 quantifies the results shown in Figure 2.5 and Figure 2.6 Figure 2.7 (a) demonstrates the total volume of both bubbles for the two injections with ($U_{inj,L}$ = 65 m/s , $U_{inj,R}$ = 65 m/s) and ($U_{inj,L}$ = 63 m/s , $U_{inj,R}$ = 65 m/s) are fairly similar throughout the bubble rise process. However. the injection with ($U_{inj,L}$ = 60 m/s , $U_{inj,R}$ = 65 m/s), has a lower value for the total volume of bubble initially because of the lower amount of injected gas, but then it starts to have a greater value than the other two cases due to the collapse of the left bubble and gas transfer from interstitial flow to the right bubble so that the right bubble maintains its shape and volume and reaches the bed surface. In Figure 2.7 (b), the volume of both individual bubbles ($U_{inj,L}$ = 65 m/s , $U_{inj,R}$ = 65 m/s) are similar to one another as they both grow after the injection, reach a maximum volume and then start to decrease in size due to gas leakage into the interstitial flow before eventually reaching the bed surface. In the other case, the volume of the bubble with $U_{inj,L}$ = 63 m/s is lower than the volume of the bubble with $U_{inc,R}$ = 65 m/s throughout the rise process, but they both reach the surface of the bed without collapsing. However, when the size difference is even increased more,

with injecting the gas into the bubble with $U_{inj,L} = 60$ m/s, and keeping the $U_{inj,R} = 65$ m/s the same, it can be observed that the left bubble decreases in size faster until it's volume reaches zero. However, the right bubble retains a larger volume than in any other case as it reaches the surface of the bed. Thus, the simulation results confirm the hypothesis from the previous experimental work shown in Figure 2.1 that preferential gas channeling toward the larger bubble leads to the collapse of the smaller bubble. As the smaller bubble decreases in size, less and less gas channels into it, demonstrating the instability which causes the collapse. Further, the gas velocity fields and streamlines demonstrate that gas is not transferred directly from the collapsing bubble to the surviving bubble, but rather, gas channels into both bubbles from below and re-emerges from the roofs of both bubbles to create a fairly uniform upward gas flow above the bubbles.

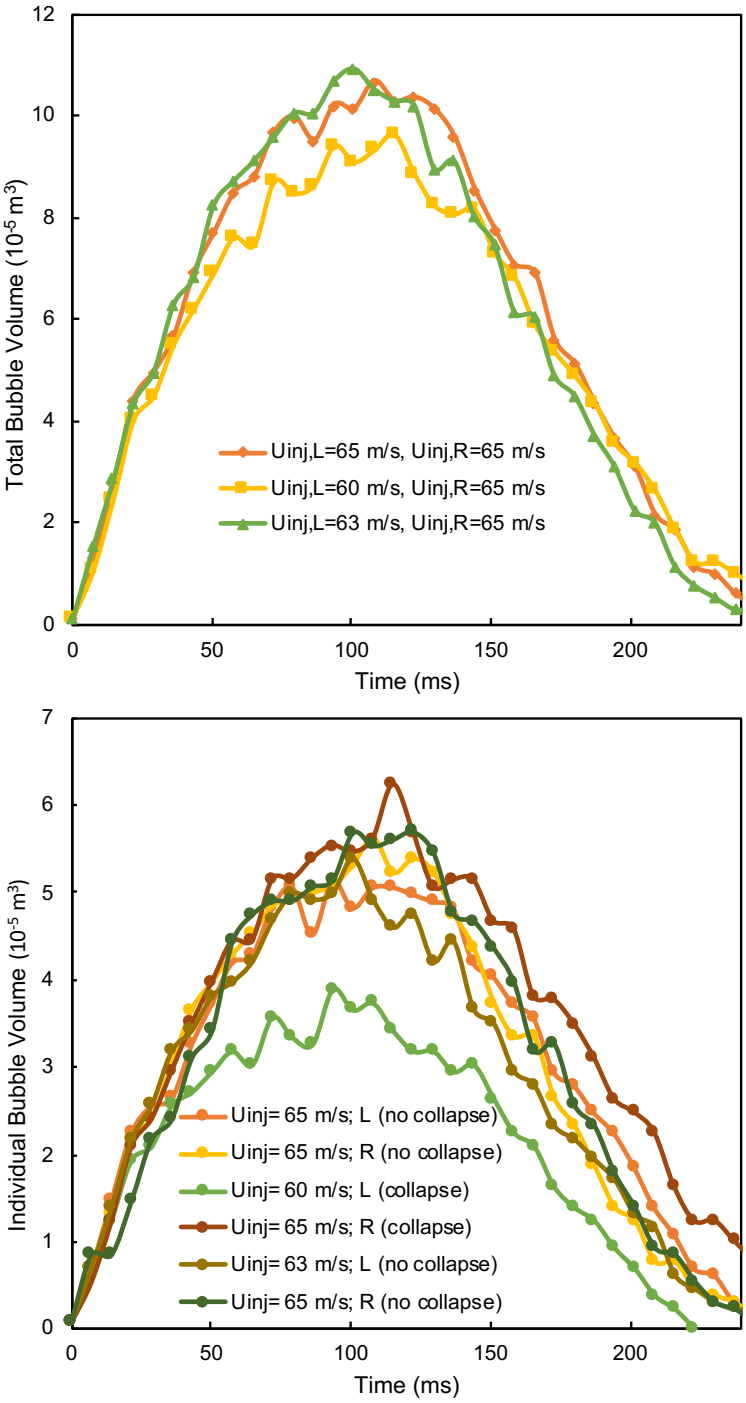

Figure 2.7. Bubble volume vs time for two bubbles injected side by side (L = left, R = right) for 30 ms with different gas injection velocity. (a) The total bubble volume from both the right and left bubbles and (b) the individual volume of each bubble.

2.4 Conclusion

CFD-DEM simulations have been shown to reproduce the bubble collapse phenomenon observed in a prior experimental study [29] when two bubbles are injected side-by-side into an incipiently fluidized bed. Simulation results show that the bubble does indeed collapse, rather than move out of the central injection plane and that the collapsing bubble must be slightly smaller than the surviving bubble for collapse to occur. CFD-DEM simulation predictions of gas velocity confirm the mechanism proposed in the experimental study [29] that gas channels preferentially to a larger bubble, leaving the smaller bubble with insufficient gas flow through it to maintain its shape. Simulation predictions also show that gas flowing out of the collapsing bubble does not flow directly into the surviving bubble.

Chapter 3 : An Asynchronous Bubble Pinch-Off Pattern Arising in Fluidized Beds due to Jet Interaction: A Magnetic Resonance Imaging and Computational Modeling Study

This chapter was published previously in the following article:

A. Penn, A. Padash, M. Lehnert, K. P. Pruessmann, C. R. Müller, and C. M. Boyce, "Asynchronous bubble pinch-off pattern arising in fluidized beds due to jet interaction: A magnetic resonance imaging and computational modeling study," *Phys. Rev. Fluids*, vol. 5, no. 9, pp. 1–17, 2020.

This work was a co-first authorship between Alexander Penn and Azin Padash. Penn and his collegues at ETH Zurich conducted all the magnetic resonance imaging (MRI) experiments, and Padash conducted all the CFD-DEM simulations in Prof. Boyce's lab at Columbia University.

3.1 Introduction

Fluidized beds are formed when upward gas flow through a bed of granular particles suspends the particles, causing them to exhibit properties resembling those of a continuous liquid, rather than a set of discrete solid particles. Fluidized beds have been the subject of decades of research in the engineering and physics communities due to both their relevance to a variety of industrial processes as well as their intriguing physical aspects which blend solid, liquid and gaseous physics. The entry of gas into fluidized beds often comes in the form of jets: concentrated areas of gas flow through an orifice which can form permanent voids as well as voids which oscillate in space and time as bubbles of gas pinch off from these voids and subsequently rise to the bed surface. These jets are of industrial importance since they affect the gas-solid contact and solids mixing in industrial processes. Jets are also interesting on a fundamental physics basis, since their behavior is in many ways analogous to jets and plumes in gas-liquid systems, despite the fact

that no surface tension exists between gaseous voids and particulate regions in fluidized beds and thus gas passes freely between voids and the interstices between particles.

Previous experimental [55]–[59] and numerical [57], [59]–[61] studies have investigated the interaction between two jets in fluidized beds. These studies have generally noted three regimes of behavior [55], [56], [60], [61]: (1) an isolated regime in which the two jets do not affect one another, (2) a coalesced or merged regime in which the jets or the bubbles which pinch off from them merge into a single body and (3) a transition regime in between the isolated and coalesced regime. These studies have noted that the strongest factor differentiating these regimes is the separation distance between orifices and that gas jet velocity acts as a secondary factor. The largest difference between previous studies has been the description of the transition regime: descriptions have included (a) jets looking essentially like isolated jets but taller due to jet-jet interaction [55], (b) jets and bubbles changing in shape due to one another but not coalescing [60], [61] and (c) jets oscillating in time between acting as isolated jets and coalescing [56]. An issue with these previous studies has been that they have characterized jet interaction in pseudo-2D beds or semi-cylindrical beds where the jets are located near the planar wall to enable optical measurements. Since jets also have been shown to interact with walls [62], it is unclear how wall effects could impact the understanding of jet interaction provided by the prior work.

Here, we seek to use rapid magnetic resonance imaging (MRI) of particle concentration and velocity in a 3D fluidized bed as well as computational fluid dynamics – discrete element method (CFD-DEM) simulations to provide new insights into the transition regime of bubble interaction in fluidized beds. Several previous studies have used tomographic imaging, such as X-ray and MRI, to study the internal dynamics of fluidized beds [63], [64]. Two excellent review articles provide an overview of MRI of granular materials and flow phenomena [65], [66]. Notably,

prior studies have used MRI to investigate jetting in fluidized beds [62], [67], [68]. However, these studies mostly have been limited to time-averaged measurements [62], [69], and thus have not been able to image the dynamics of interacting jets in the transitional regime. Additionally, they have often studied systems where the only gas flow came from the jet orifices, and thus gas from jets was used to both fluidize the bed and generate a jet, leading to very different dynamics from studies in which background gas flow from the distributor fluidizes the particles [68]. One study [68] achieved rapid MRI of jet and bubble motion in a system with a central jet and background gas flow; however, the imaging was not able to produce rapid images of particle velocity and only one jet was studied, precluding understanding of dynamic jet interaction. Recently developed MRI advances [70] have enabled dynamic imaging of both particle concentration and velocity, and these capabilities have been used to characterize bubble dynamics in beds with [71] and without [72][29] cohesive liquid bridging. These techniques have also recently been used to characterize the dynamics of single jets injected into incipiently fluidized beds [73], [74]. Here, we use these rapid MRI techniques and simulations to enable us to identify new types of behavior in the transitional jet interaction regime and describe the underlying physical mechanisms.

3.2 Methods

3.2.1 Fluidized Bed

The fluidized bed was made of polymethyl methacrylate (PMMA) and was cylindrical with an inner diameter of 190 mm and a height of 300 mm. It was filled with particles to a height H_0 = 200 mm; the particles were agar shells filled with middle-chain triglyceride oil from which MRI signal was derived. Two different sizes of particles were used in separate experiments: (1) "1 mm particles" which had a diameter d_p = 1.02 ± 0.12 mm, a density ρ_p = 1040 kg/m^3, a coefficient of friction μ = 0.54 ± 0.05 and a coefficient of restitution e = 0.70 ± 0.03 and (2) "3 mm particles"

with d_p = 2.93 ± 0.04 mm, ρ_p = 1040 kg/m^3, μ = 0.56 ± 0.04 and e = 0.69 ± 0.03. Air at ambient conditions flowed through a distributor made from a 10 mm perforated plate of PMMA to fluidize the particles. Particle with a diameter of 3 mm fall into Geldart [75] Group D and 1 mm particles are on the border between Groups B and D. The minimum fluidization velocities of the 1 mm and 3 mm particles were 0.25 m/s and 0.70 m/s, respectively.

For both types of particles, the coefficients of restitution were measured by dropping individual particles from 130 mm height onto a polished horizontal stone surface and recording the rebound height of the particles with a high-speed camera. The measurements were repeated ten times in order to obtain the coefficients of restitution and their standard deviation. The described technique neglects the effect of the air resistance and therefore the actual coefficients of restitution might be slightly higher compared to the reported values. The angles of repose θ_r were measured by filling a transparent horizontal cylinder of diameter 100 mm halfway with particles and slowly rotating the cylinder around its axis at about 0.2 rpm, while recording the inclination angle between the particle surface and a horizontal level using a camera. The coefficient of friction μ was determined according to $\mu = \tan(\theta_r)$.

3.2.2 Jet and bubble injection

Gas was injected through orifices which were flush with the distributor and d_o = 7.95 mm in diameter. Three different configurations of orifices were used: (1) a single central port, (2) two ports with centers separated by d_{sep} = 40 mm, each 20 mm from the center of the distributor, corresponding to d_{sep}/d_o = 5.0 and (3) two ports separated by d_{sep} = 80 mm, each 40 mm from the center, corresponding to d_{sep}/d_o = 10.1. For jet injection, gas was injected continuously from a 2.5 L tank kept at constant pressure; the pressure of the tank was set to different values to achieve different flow rates of gas through the jets, corresponding to different average gas velocities

through the jet orifices (u_{jet}). For all cases, the flow rates through both jets in one experiment were the same.

3.2.3 MRI Measurements

MRI measurements were conducted by surrounding the fluidized bed with a custom-built 16-channel radiofrequency array [70] and placing the system in a Philips Achieva 3T medical scanner. Both the solids volume fraction and the vertical and horizontal components of the particle velocity were measured simultaneously using echo planar imaging (EPI) [76] with phase contrast velocimetry [77]. The temporal resolution of the measurements was 18 ms, the nominal spatial resolution was 3 mm horizontal (x) × 5 mm vertical (y) and the field-of-view was 200 mm (x) × 300 mm (y). Images were taken of a central vertical slice through the bed with a slice thickness of 10 mm. The MRI pulse sequence and methods used are described further by Penn et al. [70] . In processing of the MRI velocity images, pixels which contained a particle signal intensity less than 25% of the maximum intensity were considered as consisting of the gas phase. The particle velocities were set to zero in the gas-phase pixels to avoid the images from showing spurious low signal-to-noise particle velocity measurements in these gas-laden regions.

3.2.4 Numerical Simulations

CFD-DEM simulations were conducted in a 3D cylindrical bed with an inner diameter of 190 mm and a height of 300 mm matching the size of the experimental setup. The simulations used CFD to model the gas flow on a computational grid and DEM was used to model the motion of each individual particle using Newtonian and contact mechanics. Simulations were conducted using the open source CFDEMcoupling software [41] which combines CFD from OpenFOAM [42][78] and DEM from LIGGGHTS. A prior paper provides the full equations used [44].

The simulations matched the particle properties used in the experiments. The minimum fluidization velocity measured in the simulations for the 1 mm and 3 mm particles were 0.25 m/s and 0.70 m/s, respectively, matching those determined experimentally. To match the cylindrical experimental geometry, an unstructured grid with rectangular cells was used in the center of the system and wedge-shaped cells near the walls. Figure 3.1 shows a horizontal cross section of the mesh used in CFD for (a) 1 mm particles and (b) 3 mm particles. For 1 mm particles, the grid spacing in the vertical-direction was dz = 3 mm, and for the square grid cells far from the boundaries $dx = dy$ = 3.015 mm was used in the horizontal direction. For 3 mm particles, dz = 9.375 mm, and $dx = dy$ = 9.047 mm were used. Grid sizes were chosen to be approximately 3 times the particle diameter to match that the recommended values for CFD-DEM simulations in the literature [47]. The jet injection ports were square in shape with side length of 9.05 mm, and they were separated by d_{sep} = 36.2 mm, each 18.1 mm from the center of the grid, corresponding to the experiment in which the ports are separated by 40 mm. An incompressible code with an implicit solver was used with CFD time step of 0.1 ms. The no-slip wall boundary condition as well as constant pressure for the outlet boundary condition were used for CFD. In DEM, the Poisson's ratio and Young's modulus used were 0.32 and 10 MPa, respectively with a time step of 0.001 ms. The two phases were coupled using Wen & Yu drag law [79]. Jet velocities used in simulations were significantly different from those used in experiments, as has been seen in simulations for bubble injection [30]. These differences can be attributed to (i) inaccuracies in the measurement of jet velocity and (ii) inaccuracies in the drag law used in simulations. The sources of this difference in jet velocity to produce similar results is worthy of a complete study, but we consider this outside of the scope of the current study.

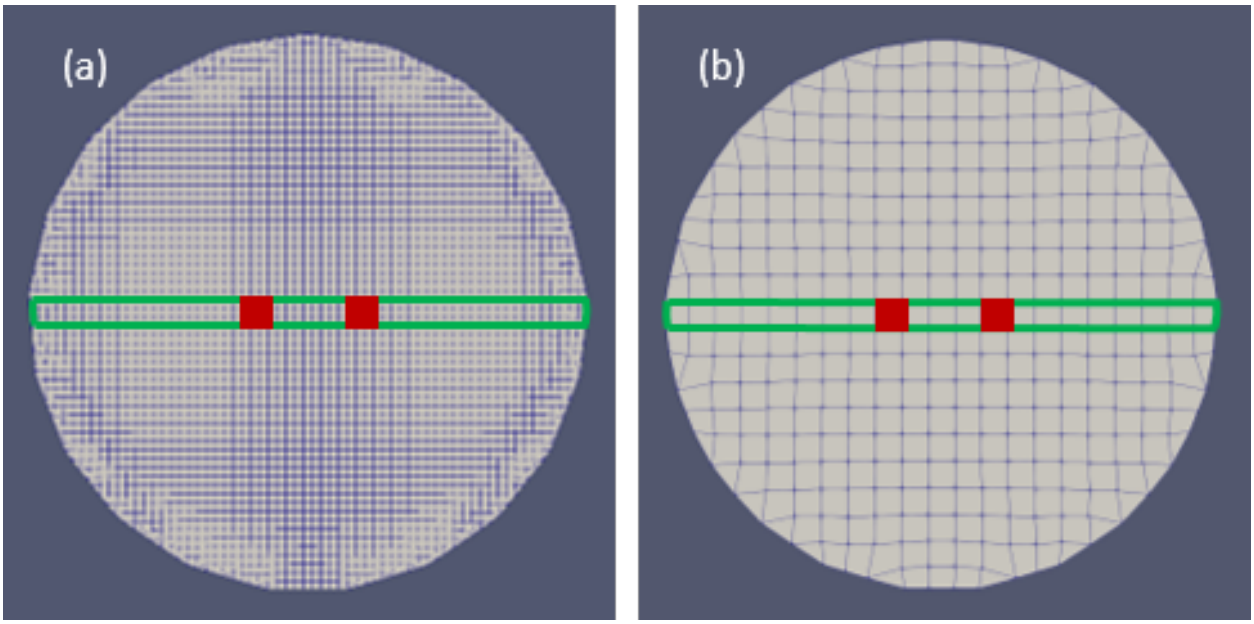

Figure 3.1. Horizontal cross-section view of the fluid grid used for (a) 1 mm particles and (b) 3 mm particles, with the green slice showing CFD cells used in vertical cross-section images and the red squares showing the two ports for jet injection at the gas distributor.

3.3 Results and Discussion

3.3.1 MRI Results

Figure 3.2 shows a time series of images of particle concentration (upper row) and particle velocity (lower row) taken of a central vertical slice through the fluidized bed. The images are of two gas jets injected into the bed of 1 mm particles with a separation distance of d_{sep}/d_o = 5.0 between the center of jets with gas velocities through the jet orifices of u_{jet} = (a) 38 m/s, (b) 66 m/s and (c) 97 m/s. For all cases, vertical jets form just above the orifices and the jets pinch off to form bubbles which rise to the bed surface. Particle velocities are fast and upward surrounding the jets and bubbles and slow and downward in the outer annulus of the bed. In all cases, an asynchronous bubbling pattern is observed: when a jet is growing on the right side, a jet pinches off into a bubble on the left side and vice-versa. Bubble pinch-off from the two jets is approximately 180° out-of-phase. This forms an alternating pattern of bubbles which rises in a pattern that resembles

interlocking teeth in a zipper, until the pattern is broken by bubbles coalescing. With increasing gas flow rate, the jets become larger before pinching off to form bubbles, resulting in larger bubbles rising through the bed.

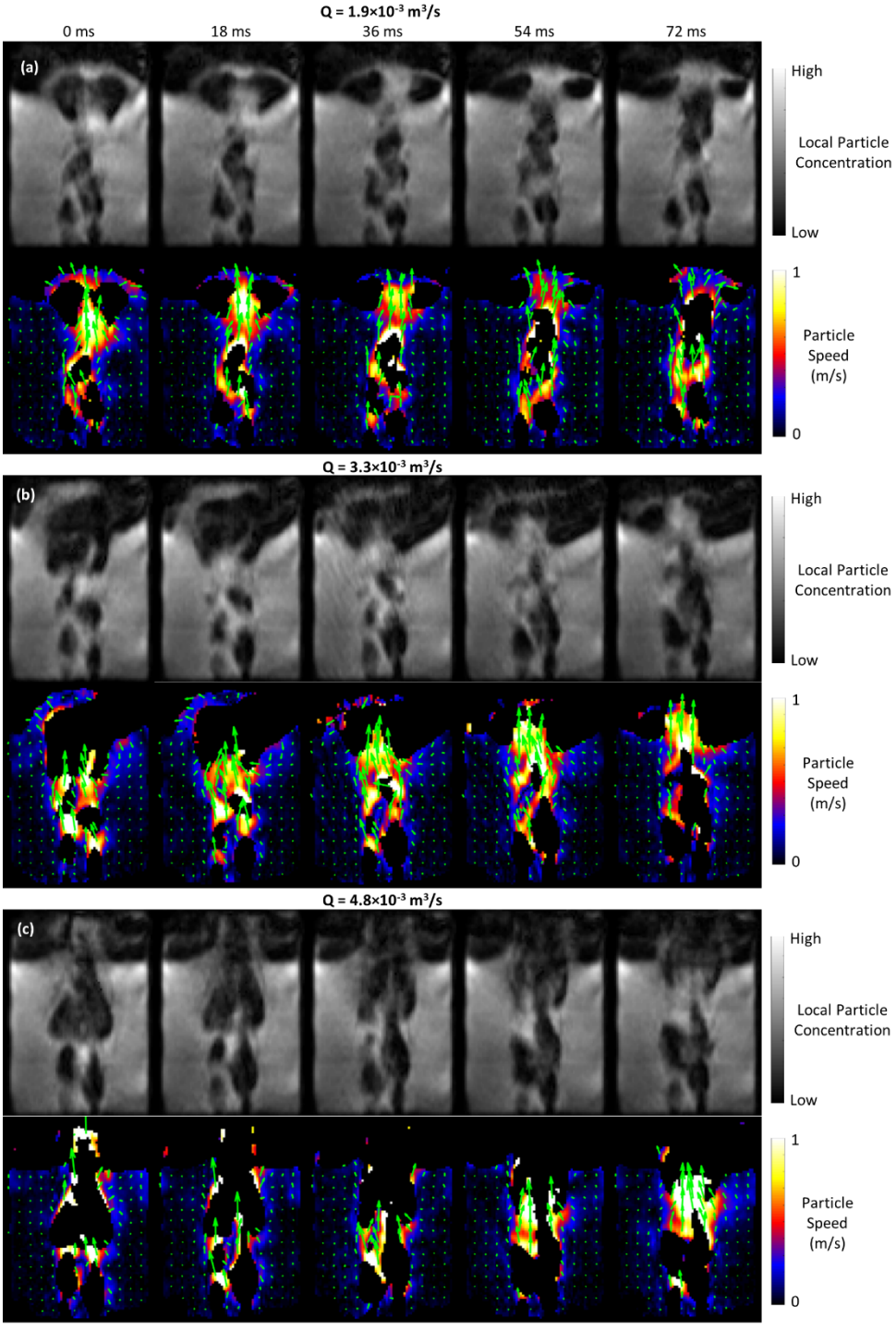

Figure 3.2. Time series of images of particle concentration (upper row) and particle velocity (lower row) of a central vertical slice through the bed of two gas jets separated by d_{sep}/d_o = 5.0 injected into an incipiently fluidized bed of 1 mm particles with an average gas velocity through each orifice of u_{jet} = (a) 38 m/s, (b) 66 and (c) 97 m/s.

Figure 3.3 shows a time series of images of particle concentration and velocity for a single central gas jet injected into an incipiently fluidized bed of 1 mm particles with a gas velocity through the jet orifice u_{jet} = 52 m/s. Vertical bulbous gas jets form directly above the orifice, and these jets pinch off to form bubbles which rise to the bed surface without coalescing. Particle velocities are high and upward directly above and below jets and bubbles, but move downward slowly to the sides of the bubbles and jets. This figure is representative of results from a wider range of flow rates studied; images of experiments at different flow rates are excluded for brevity.

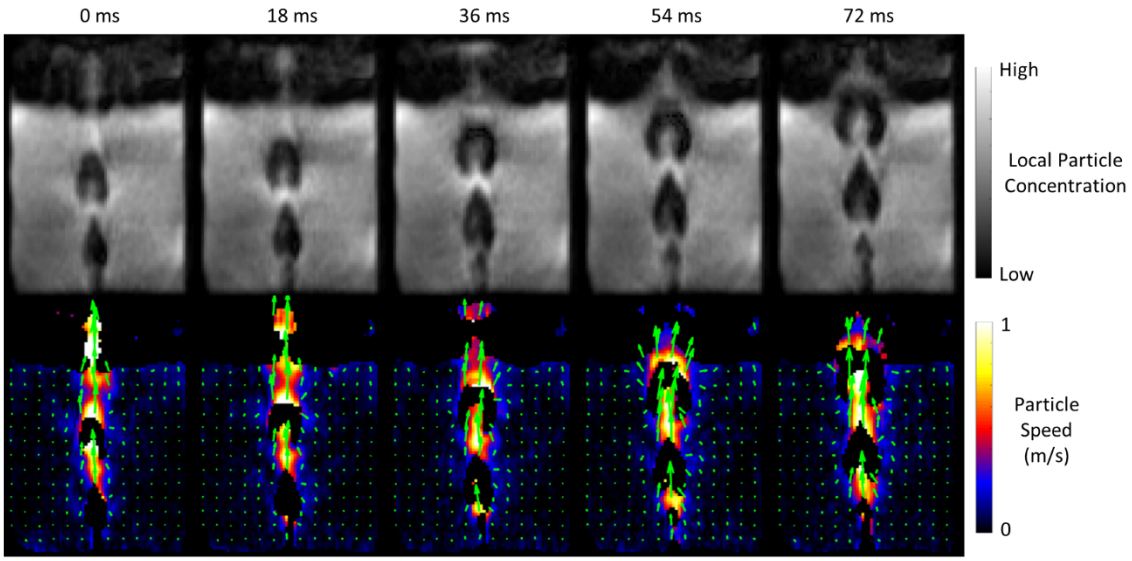

Figure 3.3. Time series of images of particle concentration (upper row) and particle velocity (lower row) of a central vertical slice through the bed of a single central jet injected into an incipiently fluidized bed of 1 mm particles with an average gas velocity through the orifice of u_{jet} = 52 m/s.

Figure 3.4 shows a time series of images of particle concentration and velocity for jets separated by d_{sep}/d_o = 10.1 injected into an incipiently fluidized bed of 1 mm particles with u_{jet} = 38 m/s. The jets are not vertical, but rather angled out toward the walls. The jets undulate in width while generally increasing in width with increasing distance above the orifice. Bubbles pinch off from the top of the jets and rise to the bed surface. Particle velocities are fast and upward in the regions directly above and below bubbles and jets and are downward and slow in the region

between the two jets as well as the regions between the jets and the walls. Unlike the asynchronous bubble pattern for the d_{sep}/d_o = 5.0 separation in Figure 3.2, bubbles pinch off from the two jets nearly simultaneously. This figure is representative of results from a wider range of flow rates studied; images of experiments at different flow rates are excluded for brevity.

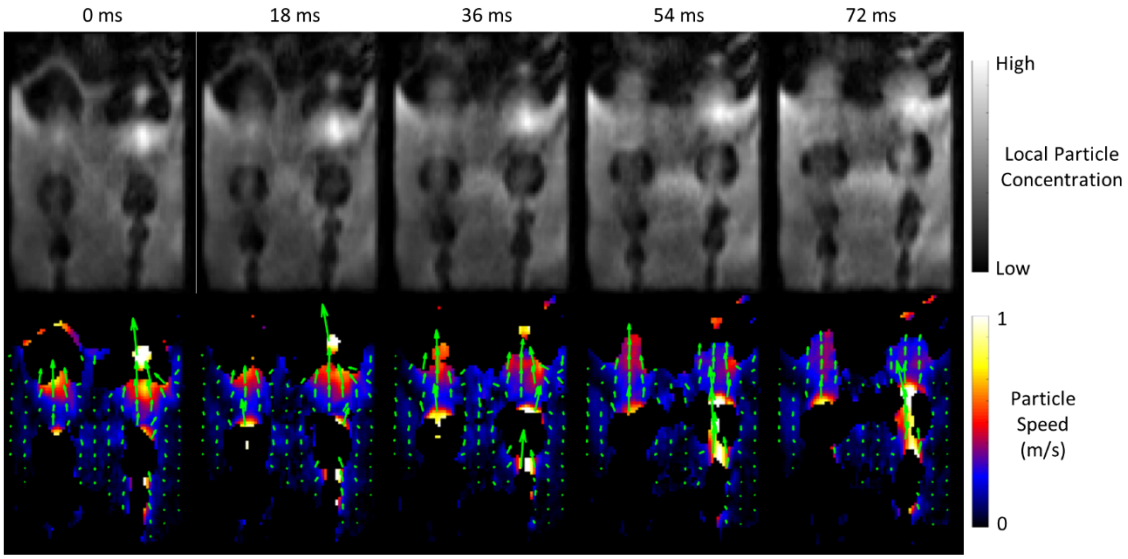

Figure 3.4. Time series of images of particle concentration (upper row) and particle velocity (lower row) of a central vertical slice through the bed of two gas jets separated by dsep/do =10.1 injected into an incipiently fluidized bed of 1 mm particles with an average gas velocity through each orifice of ujet = 38 m/s.

Figure 3.5 shows a time series of images for two jets injected into an incipiently fluidized bed of 3 mm particles with a separation distance of d_{sep}/d_o = 5.0 and u_{jet} = 97 m/s. Vertical jets form directly above the orifices, and bubbles pinch off from the tops of these jets and rise to the bed surface. Unlike the asynchronous bubble pattern in Figure 3.2, the bubbles pinch off simultaneously from the top of each jet. The distinction in particle concentration between the jets and the surrounding particulate phase is less clear than in the corresponding case for 1 mm particles in Figure 3.2 (a). Particle velocities are fast and upward in the regions directly above and below the bubbles and are slow and downward in the outer annulus of the bed. This figure is

representative of results from a wider range of flow rates studied; images of experiments at different flow rates are excluded for brevity.

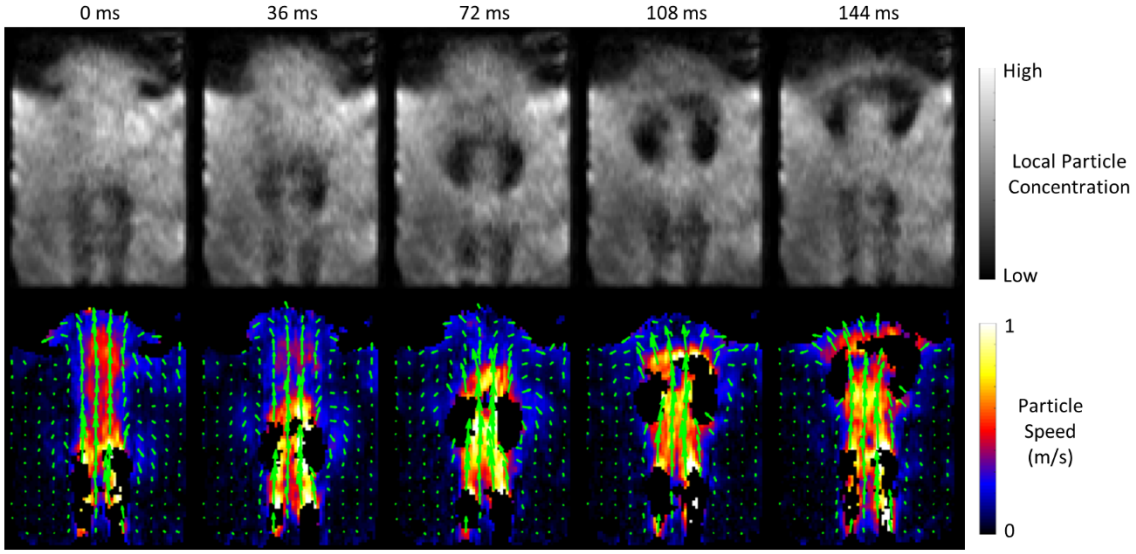

Figure 3.5. Time series of images of particle concentration (upper row) and particle velocity (lower row) of a central vertical slice through the bed of two gas jets separated by d_{sep}/d_o = 5.0 injected into an incipiently fluidized bed of 3 mm particles with an average gas velocity through each orifice of u_{jet} = 97 m/s.

3.3.2 Simulation Results

Figure 3.6 shows time series of images of (a,b) MRI results and (c,d) CFD-DEM predictions for closely spaced jets in the 1 mm particle system, showing (a,c) local particle concentration and (b,d) horizontal particle velocity. Results show that CFD-DEM simulations can reproduce the asynchronous, out-of-phase bubble pinch-off phenomenon observed in MRI, providing confidence in the accuracy of the simulations, in addition to a wide array of studies which have shown that CFD-DEM predictions compare well with experimental results [45], [54], [80]–[82]. Further, both MRI and simulations show that when a bubble is pinching off, particles surrounding the jet move horizontally towards the center of the jet at the point of pinch-off, causing the bubble to pinch off. In contrast, both MRI and simulations show that when a jet is growing, particles move horizontally away from jet, so that the jet can widen.

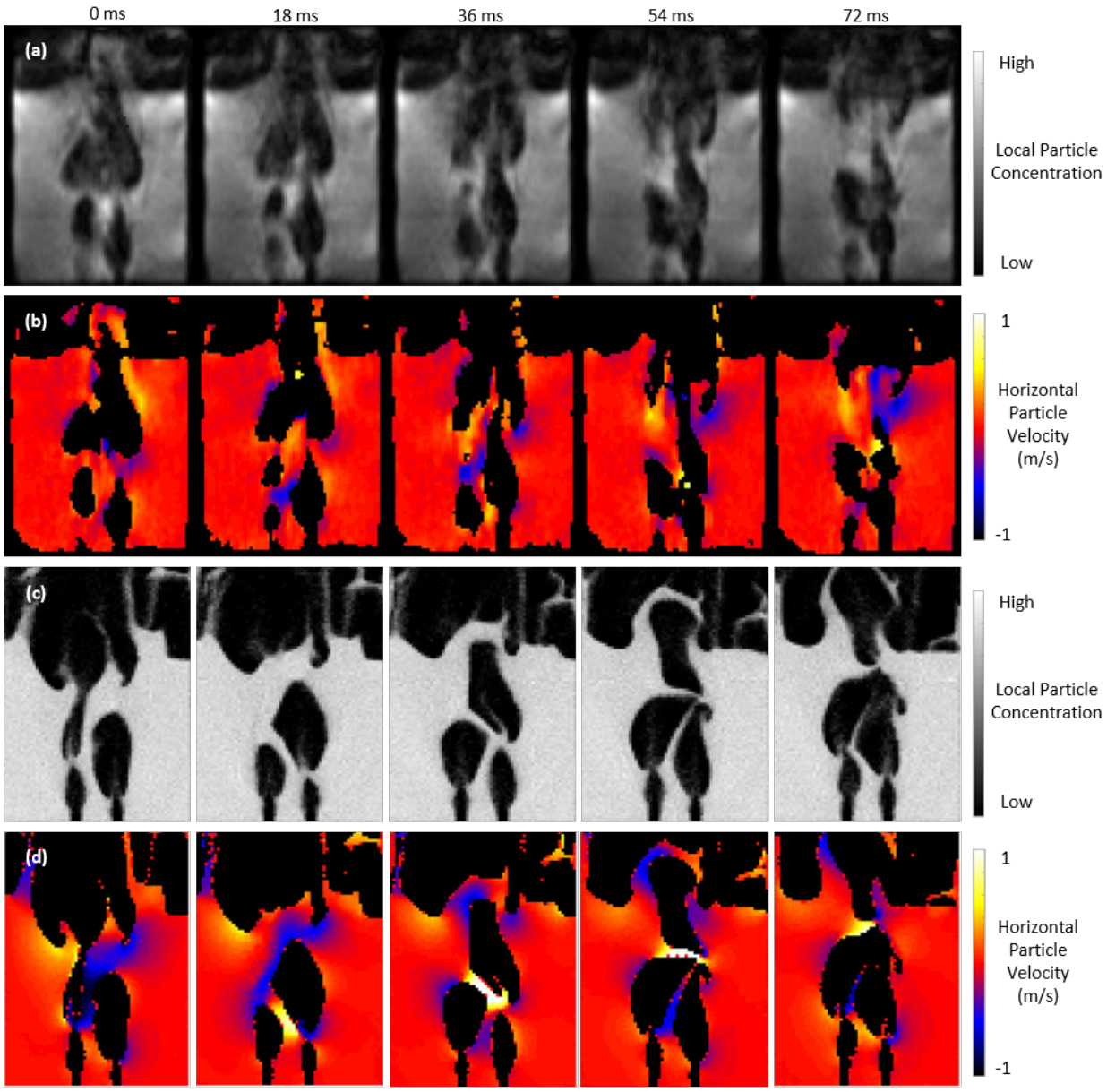

Figure 3.6. Time series of images of jet interaction in 1 mm particles showing particle concentration (a,c) and horizontal particle velocity (b,d) from MRI measurements (a,b) and CFD-DEM simulations (c,d). MRI Jet velocity: 97 m/s; CFD-DEM jet velocity: 3 m/s.

Figure 3.7 shows time series of images from the same CFD-DEM simulation as in Figure 3.6, showing 3D renderings of the void regions near the jet injection ports (gray), providing (a) a front view and (b) a top view. Results show that there is no significant motion of jets and bubbles out of the central vertical slice shown in Figure 3.6.

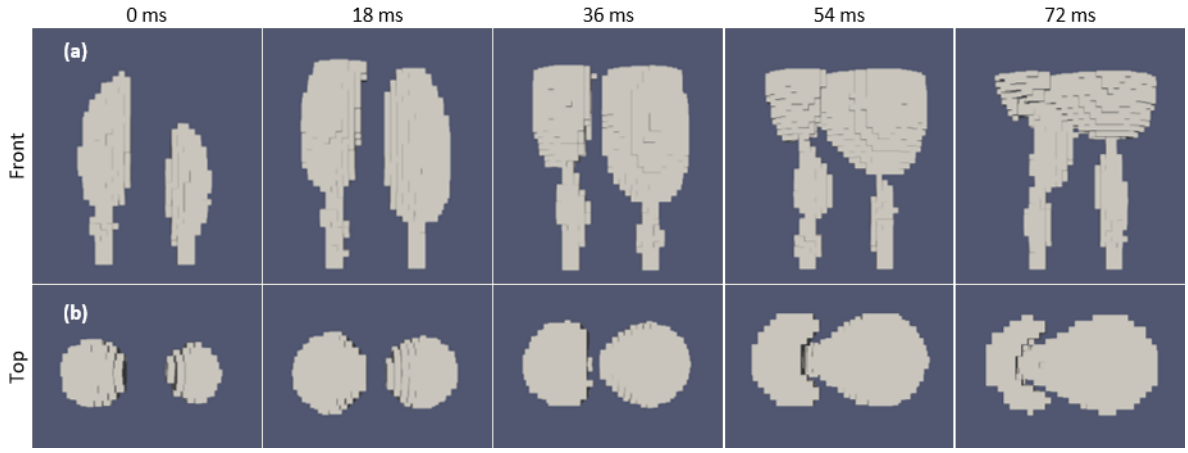

Figure 3.7. Time series of images of jet interaction in 1 mm particles from CFD-DEM simulations showing 3D renderings of voids near the orifices from (a) a front view and (b) a top view.

Figure 3.8 shows time series of images from the same CFD-DEM simulation as in Figure 3.6, but this time showing (a) particle concentration, (b) horizontal gas velocity, (c) horizontal drag force on particles and (d) horizontal particle velocity. In (a, b and d) void regions are colored black to highlight only results in particle-laden regions, while in (c) void regions are colored white. Results show that the gas velocity in the horizontal direction is highest towards the top of jets with gas moving horizontally away from the jets. This gas velocity leads to high horizontal drag forces on the particles relative to their weight in these regions, pushing the particles away from the tops of jets growing jets. This leads to a pattern in which the drag force acting on central particles between the two jets push particles away from a growing jet and toward a jet which is pinching off. The results for the horizontal particle velocity are similar to those for the drag force: particles move away from the tops of growing jets, causing central particles between the two jets to move away from the growing jet and towards a jet which is pinching off.

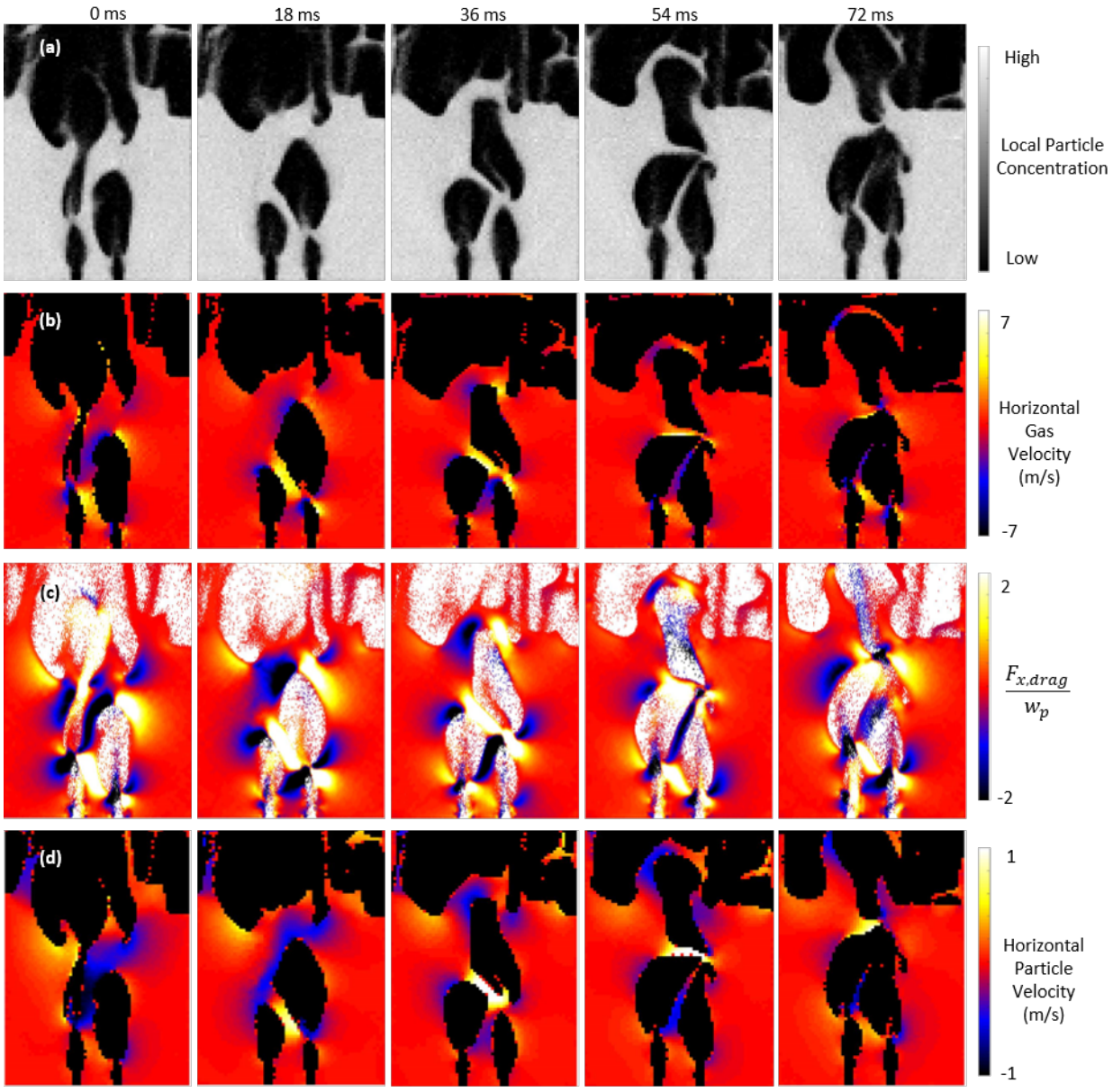

Figure 3.8. Time series of images of jet interaction in 1 mm particles from CFD-DEM simulations showing (a) particle concentration, (b) horizontal gas velocity, (c) horizontal drag force normalized by particle weight and (d) horizontal particle velocity. Jet velocity: 3 m/s.

Figure 3.9 shows time series of images of MRI experiments and simulations with jet separation distances corresponding to those in Figure 3.6, but with 3 mm fluidized particles. In contrast to the jets in Figure 3.6, bubbles pinch of nearly simultaneously, i.e. in-phase, with one another. Figure 3.9 shows that CFD-DEM simulations can reproduce the simultaneous bubble

pinch-off seen experimentally, providing further confidence in the predictive capabilities of the simulations. Horizontal particle velocities have lower magnitudes than those observed in Figure 3.6, but both Figure 3.6 and Figure 3.9 show that particle velocities move horizontally toward the center of a jet at the point of pinch-off as a bubble pinches off from the jet.

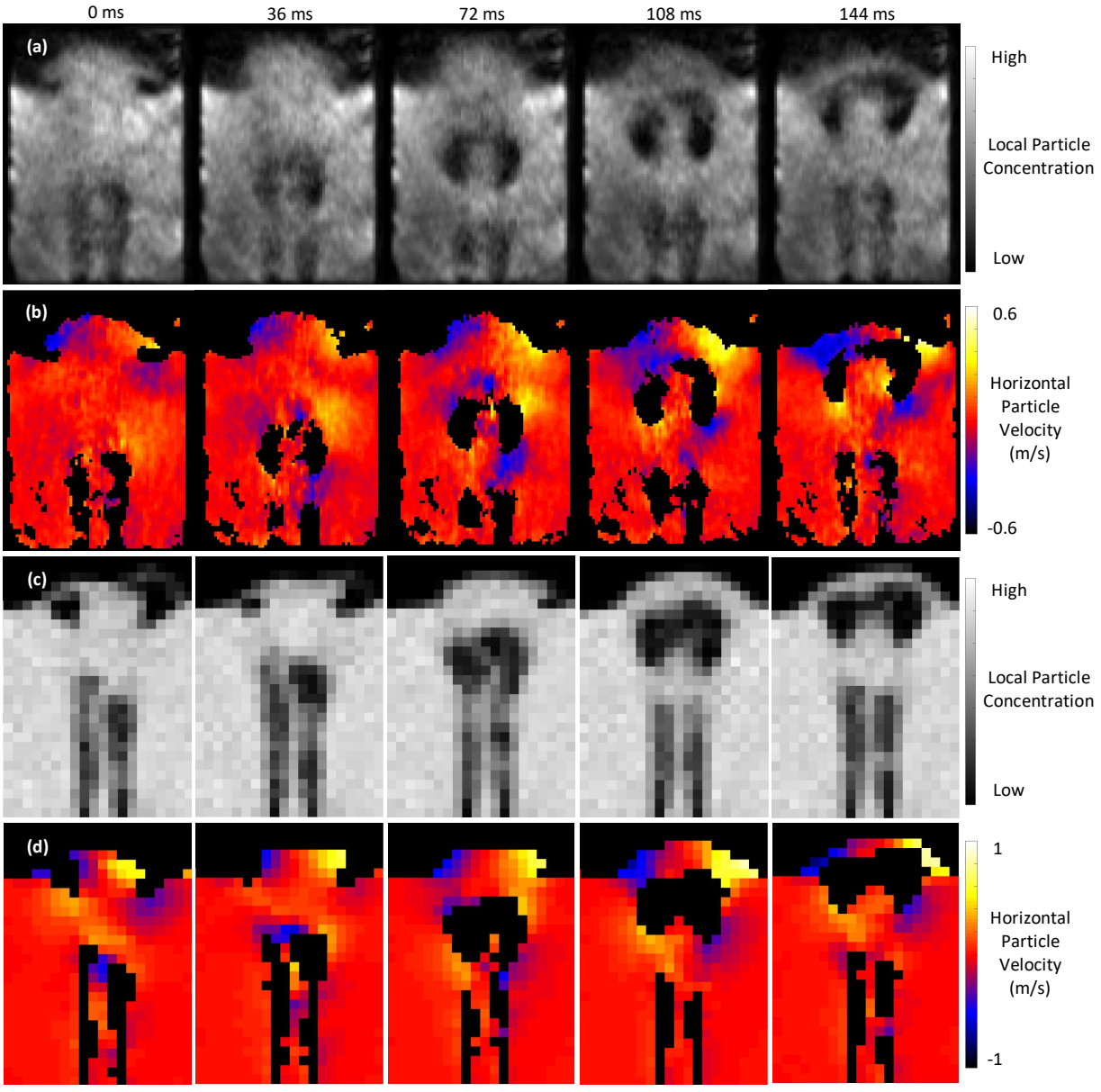

Figure 3.9. Time series of images of jet interaction in 3 mm particles showing particle concentration (a,c) and horizontal particle velocity (b,d) from MRI measurements (a,b) and CFD-DEM simulations (c,d). MRI Jet velocity: 97 m/s; CFD-DEM jet velocity: 40 m/s.

Figure 3.10 shows the same time series of images as in Figure 3.9, but with 3 mm particles instead of 1 mm particles. CFD-DEM predictions show comparable horizontal gas velocity magnitudes to those seen in for 1 mm particles in Figure 3.8. In both 3 mm and 1 mm particles, gas flow moves horizontally away from the tops of growing jets and towards the center of jets at the point of bubble pinch-off. The magnitude of the drag force normalized by particle weight is much smaller in the 3 mm particles than the 1 mm particles. In both 3 mm and 1 mm particles, drag force pushes particles horizontally away from the tops of growing jets and horizontally toward the point of bubble pinch-off when a jet is pinching off. As with the 1 mm particles, the horizontal particle velocity of particles matches the trends seen in the horizontal drag force; however, the magnitude of horizontal particle velocities in 3 mm particles is significantly lower than that observed in 3 mm particles.

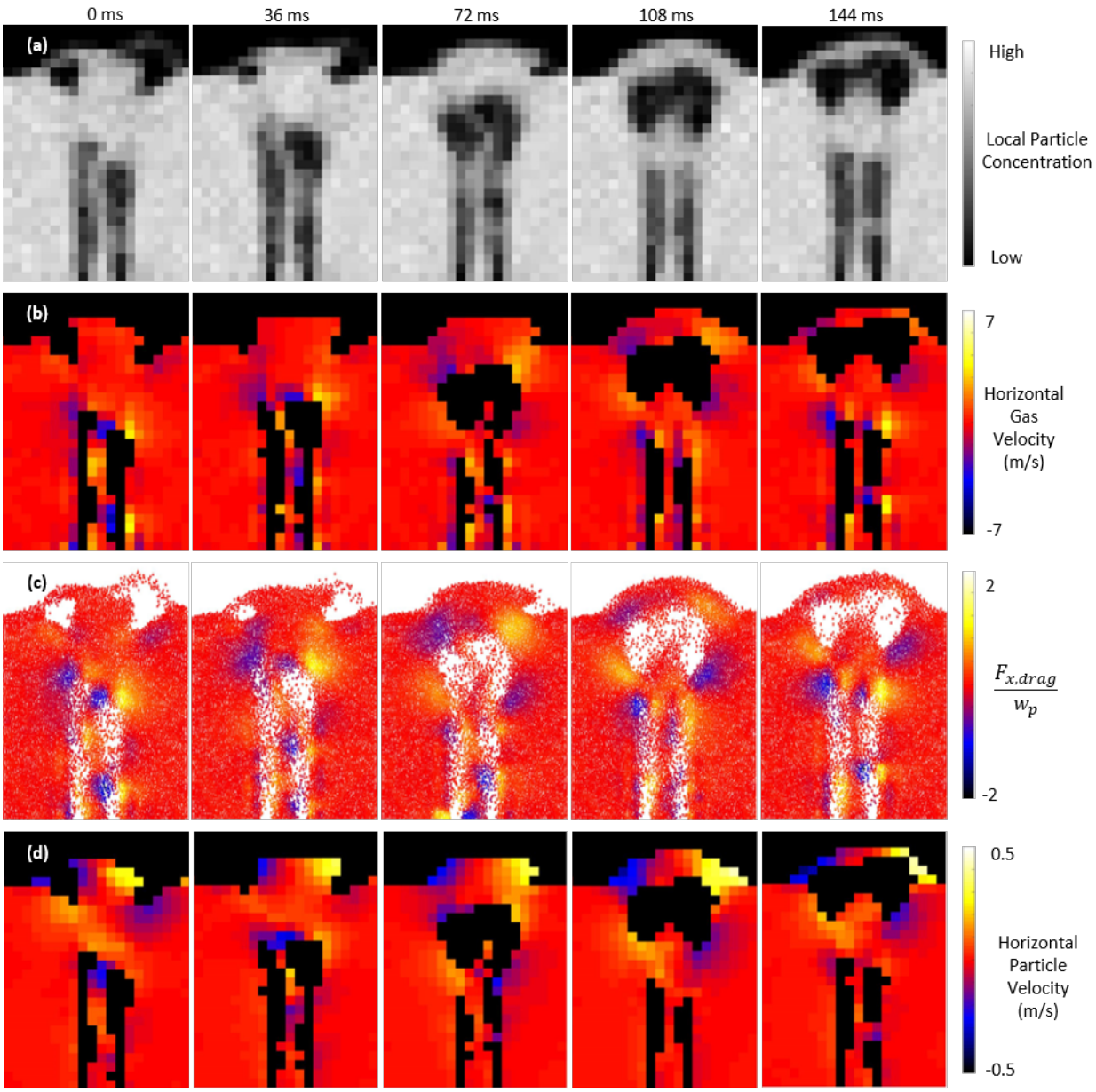

Figure 3.10. Time series of images of jet interaction in 3 mm particles from CFD-DEM simulations showing (a) particle concentration, (b) horizontal gas velocity, (c) horizontal drag force normalized by particle weight and (d) horizontal particle velocity. Jet velocity: 40 m/s.

3.4 Discussion

3.4.1 Proposed Mechanism for Asynchronous, Out-of-Phase Bubble Pinch-Off

The collective MRI and CFD-DEM results lead us to the following mechanism to explain the transition from synchronous to asynchronous bubble pinch-off in the transition regime for jet

interaction in fluidized beds: The transition is controlled by the collective horizontal motion of particles in between the two jets, which is dictated by the balance between inertia induced by drag and the momentum dissipation due to interparticle forces. In the synchronous pinch-off regime, drag forces push central particles away from the top of jets, but the particle inertia is dissipated by normal contact forces between particles as they compress into a more densely packed state and frictional forces as particles shear past one another. Thus, drag force pushes central particles near the left jet to the right and central particles near the right jet to the left, yet overall this leads to central particles shearing minimally and compressing, rather than having a net motion to the right or the left. At a critical magnitude of drag force, the inertia imparted on the particles will overcome the dissipative forces, causing strong shearing in the particles. Under these conditions, regions of particles where drag forces to the left are slightly stronger than those to the right will move collectively to the left and vice-versa. Collective motion of particles to the left will cause the left jet to pinch-off, while collective motion to the right will cause the right bubble to pinch off. Thus, the asynchronous, out-of-phase bubble pinch-off regime is the manifestation of a hydrodynamic instability arising when the drag force acting on the central particles exceeds dissipative interparticle forces due to compression and minor shearing of the central particles, causing the motion of the central particles to become unstable.

This unstable motion of central particles between the two jets leading to the asynchronous, alternating bubble pinch-off phenomenon is shown schematically in Figure 3.11. In Figure 3.11 (a), the left jet is growing, causing particles to be pushed away from it, and thus central particles between the two jets move toward the right jet, causing the right jet to pinch off. Subsequently in Figure 3.11 (b), the right jet grows, causing the central particles to move away from the right jet

and towards the left jet, causing the left jet to pinch off. The cycle begins to repeat itself in Figure 3.11 (c).

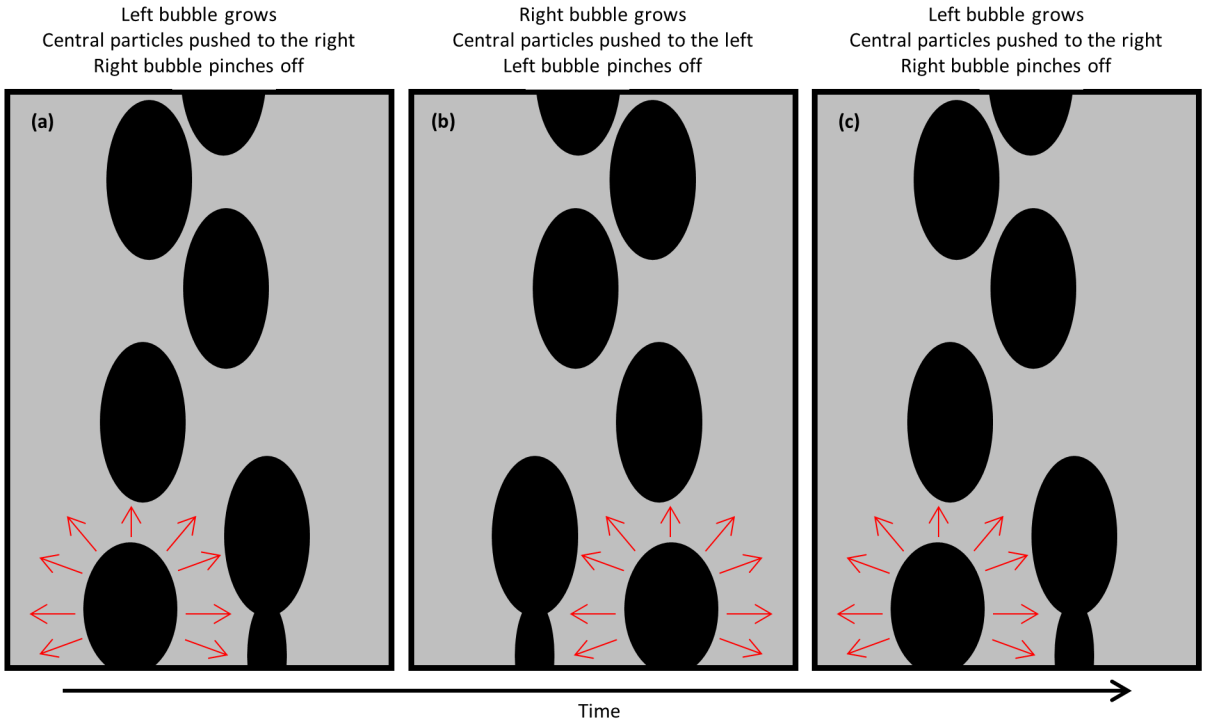

Figure 3.11. Schematic of the mechanism underlying the alternating asynchronous bubbling patter. Red arrows indicate the motion of particles.

The trends for the transition between the two jet interaction regimes shown in the Results section can be explained as follows. Larger particle have a higher permeability to gas flow ($k \propto d_p^3$) [83] and a larger mass than smaller particles. Thus, while the gas velocities and separation distances may be the same as in smaller particles, the larger particles will have a lower drag force normalized by their weight on them. Thus, the particle compression and minor shearing will dissipate the inertia imparted by drag force, explaining the simultaneous bubbling in Figures 3.5, 3.9 and 3.10. Similarly, even if smaller particles are used, but the separation distance between jets is larger, there is more space for particles to compress and minorly shear between the jets to dissipate inertial momentum from a stronger drag force on particles coming from the jets as

compared to the drag force in the larger particles. Thus, there will be enough inertial dissipation to prevent the asynchronous bubble pattern from forming, explaining the simultaneous bubbling in Figure 3.3. Only in cases of small particles and small separation distances between jets will the inertial momentum induced by strong drag forces overcome the ability of compressive and frictional forces to dissipate momentum. Thus, the asynchronous bubble pinch-off instability only manifests with smaller particles and jet separation distances, as shown in Figures 3.2, 3.6, 3.7 and 3.8.

3.4.2 Comparison with Prior Work

Altogether, the results indicate that there are two regimes of jet interaction seen here: (1) synchronous bubble pinch-off, which at moderate separation distances involves jets tilting away from one another and (2) alternating asynchronous bubble pinch-off. Simultaneous pinch-off occurs at high separation distances between jets, high gas permeability (larger particles) and lower gas flow rates. Asynchronous bubble pinch-off occurs at intermediate separation distances between jets, intermediate gas permeability and intermediate gas flow rates. The transition from the simultaneous to the asynchronous bubble pinch-off regime occurs due to the motion of particles pushed away from one jet towards the other due to jet growth becoming strong enough to pinch off the jet from the other orifice. This transition can be attributed to particle inertial forces due to drag over coming dissipative forces due to particle compression and friction.

Previous studies [56], [60], [61], [79] have classified the interaction between two jets into (1) isolated, (2) transition and (3) coalescing regimes. In these studies, isolated regimes occur when jets are separated by a sufficiently large distance such that each jet behaves like a single isolated jet and the jets do not influence each other in any way. Coalescing regimes refer to a regime where either the jets themselves coalesce [55] or the bubbles which pinch off from the jets coalesce soon

after pinch-off [56]. Transition regimes have been characterized as regimes in which bubbles pinch-off simultaneously and the bubbles and jets influence the shape and height of one another but do not coalesce [60], [61], as well as regimes that switch randomly between isolated and coalescing regimes [56]. These studies have focused on differentiating the regimes on the basis of separation distance between jets, often normalized by the orifice diameter, and orifice velocity, often non-dimensionalized as a Froude number. Here, we identify that the transition regime can be further sub-divided into regimes that have not been described before in the literature, to the best of the authors' knowledge. As seen in Figure 3.4 at moderate separation distances, jets can still influence one another by angling away from one another due to the motion patterns of the central particles between bubbles. Additionally, as shown in Figures 3.2, 3.6, 3.7 and 3.8, at smaller separation distances, the motion of central particles can lead to the asynchronous bubble patterns where the jets do not merge but have a strong influence on the temporal development of the other jet. This study also introduces the concept that in addition to separation distance and orifice velocity, the permeability of the particles to gas flow can lead to different flow patterns in the transition regime. For instance, using larger particles with a higher permeability causes a transformation from the asynchronous bubble pattern to a transition regime in which both bubbles detach synchronously, as shown in Figures 3.5, 3.8 and 3.9.

It is also important to consider the appropriate non-dimensionalization of variables related to interacting jets shown experimentally here, particularly for the purpose of creating regime maps for interaction behavior with dividing lines given by critical values of dimensionless parameters. Several dimensional analyses have been performed on single jets injected into fluidized beds [84]–[86], yielding a variety of dimensionless groups deemed critical to this problem, mostly centered around determining a correlation for the dimensionless jet height (h_{jet}/d_o), where h_{jet} is the jet

height and d_o is the orifice diameter. For example, Blake et al. [84] determined single jet behavior was governed by four dimensionless groups: Froude number ($Fr = \frac{u_{jet}^2}{g d_o}$), Reynolds number ($Re = \frac{\rho_g u_{jet} d_p}{\mu}$), Stokes number ($St = \frac{\rho_s u_{jet} d_p^2}{\mu d_o}$) and density ratio ($\frac{\rho_g}{\rho_s}$), where g is the acceleration due to gravity, ρ_g is the gas density, ρ_p is the particle density, μ is the gas viscosity and d_p is the particle diameter. Other studies have found utilized other dimensionless parameters, such as a ratio of densities and diameters ($\frac{\rho_g d_o}{\rho_s d_p}$) [86] and a two-phase Froude number ($Fr_2 = \left(\frac{\rho_p u_{jet}^2}{(\rho_p - \rho_f) g d_o}\right)^{1/2}$) [85].

For two interacting jets, all studies [56], [60], [61], [87] have found the separation distance between jets normalized by the orifice diameter (d_{sep}/d_o) to be a critical parameter for characterizing jet interaction and normalized jet height. However, there is some discrepancy as to whether the separation distance between the center of jet orifices (d_{sep}) [56], [60], or the separation distance between the closest points of the two orifices to one another (d_{sep}-d_o) [61] should be used in the numerator. Guo et al. [56] mapped interaction regimes based on Fr_2 and d_{sep}/d_o, finding interaction to be dictated largely by the latter parameter, with jet interaction occurring at values of $d_{sep}/d_o < 6$. A different study by Guo et al. [87] also included *Re* as relevant to the dimensionless jet height for two interacting jets. A further study by Guo et al. [88] investigated the effect of jet gas velocity on interaction regimes. Zhang et al. [60] mapped interaction regimes based on d_{sep}/d_o as well as a dimensional a posteriori parameter, jet height (h_{jet}), finding a significant dependence on both for regime demarcations.

For the system studied here, it is clear that dimensionless separation distance is a critical parameter for determining jet interaction, since the asynchronous alternating bubble pattern does not occur at $d_{sep}/d_o = 10.1$, but does occur at $d_{sep}/d_o = 5.0$ for the 1 mm particles. It is unclear with the current dataset if jet velocity plays a role in determining if the jets will form the asynchronous

bubble regime because for all jet velocities studied, the asynchronous jet pattern was observed at d_{sep}/d_o = 5.0 for but not at d_{sep}/d_o =10.1 for 1 mm particles. However, the authors anticipate that jet velocities outside the range of those studied here, especially for $5 < d_{sep}/d_o < 10$ could play a role in the formation of the asynchronous pattern. The authors leave it to further study with a larger dataset to determine whether or not u_{jet} is a critical parameter for the regime map, and if so, whether the critical dimensionless parameter is *Re*, *St*, *Fr* or something else. Such a study could be conducted through numerical; however, the CFD-DEM studies used to the determine the mechanism here are too computationally expensive for a parametric study. Further, it is clear that the particle diameter plays a role in determining the regime of jet interaction, since no asynchronous bubble pattern is observed in the 3 mm particles at d_{sep}/d_o = 5.0. The authors expect an appropriate dimensionless group capturing this effect of particle diameter must incorporate differences in gas permeability with particle size [83], since the higher permeability to gas flow in the 3 mm particles is reasoned to be the cause for not observing the asynchronous bubble regime in these particles. The authors defer more definitive assertions on the exact dimensionless groups governing the regimes of jet interaction and the exact dividing lines for the regime maps to future studies in which a wider dataset is available.

The identification of the alternating asynchronous bubble pattern in interacting jets in fluidized beds opens the question of whether or not an equivalent phenomenon exists in gas-liquid systems. The governing physics of gas jets in liquid systems clearly differs from that of gas jets in a gas-solid system, since gas jets in a liquid involve surface tension as well and gas cannot travel freely across the interface between void and liquid-like regions. However, gas-liquid and gas-solid systems have similarities in balances between inertial and dissipative forces influencing their dynamics. Several studies have investigated the interaction of two gas jets injected into a liquid

[89]–[93]. Ruzicka et al. [89] identified regimes of interaction involving (i) bubbles forming and pinching off simultaneously, (ii) an "alternating" pattern in which bubbles form and pinch off at one jet for a period of time and then for another period bubbles form and pinch off at the other jet and (iii) bubbles forming and pinching off asynchronously (although not necessarily completely out-of-phase with one another). These studies have often attributed pattern formation to pressure dynamics upstream of the jet injection ports, since most studies involve gas supply from the same plenum chamber [89]–[91]. However, some studies have involved gas supply from two separate gas lines [92], [93], as conducted here. Studies have also attributed the transition from simultaneous to asynchronous bubbling to changes in the motion of liquid surrounding the jets [90], [92], similar to the mechanism proposed here. However, the authors are unaware of prior gas-liquid jet interaction studies which have identified and characterized a jetting regime with bubbles pinching off completely out-of-phase from one another.

3.5 Conclusion

Rapid magnetic resonance imaging shows that two previously unidentified regimes of jet interaction in fluidized beds exist between the extreme regimes of isolation and coalescence. These regimes are (1) jets angling away from one another at longer separation distances and (2) jets forming an alternating asynchronous bubble pattern at shorter separation distance. The pinch-off of bubbles transitions from being synchronous to asynchronous (and nearly completely out-of-phase) as the separation distance is decreased and particle size is decreased. CFD-DEM simulations and MRI measurements demonstrate that the horizontal motion of particles between the two jets causes the transition from synchronous to asynchronous bubble pinch-off. In the asynchronous, alternating bubble pinch-off regime, particles move away from one jet as it grows, causing the other jet to pinch off. Based on CFD-DEM simulations, we explain this alternating

asynchronous jet pinch-off as the manifestation of a hydrodynamic instability which occurs when inertial forces acting on particles due to drag exceed the dissipative forces from particle compression and friction, causing an unstable collective motion of the central particles. This mechanism is similar to that put forward previously for asynchronous bubbling in gas jets in liquid systems [90]; however, we are unaware of prior reports of completely out-of-phase bubble pinch-off in gas-liquid systems.

Chapter 4 : Characterizing Alternating Bubbles Emerging from Two Interacting Vertical Gas Jets in a Liquid

This chapter was published previously in the following article:

A. Padash, B. Chen, and C. M. Boyce, "Characterizing alternating bubbles emerging from two interacting vertical gas jets in a liquid," *Chem. Eng. Sci.*, vol. 248, p. 117199, 2022.

This work was a co-first authorship between Azin Padash and Boyuan Chen. Padash conducted all the experiments and image processing and Chen developed the harmonic oscillator model in this work.

4.1. Introduction

Jets or plumes of gas enter liquid vertically and break off to form bubbles which rise vertically in a variety of industrial and geological systems. These jets of bubbles are located close to one another in many of such systems, and thus are able to interact, which in turn affects bubble dynamics. Studying these bubble dynamics is of great importance to better comprehend the bubble-bubble and bubble-liquid interactions which are critical in many industrial applications, such as enhancing the intensity of mixing in metallurgical processes [94], [95], [96] nuclear and pharmaceutical reactors [97], [98], reducing greenhouse gas emissions [99]–[101] and oil and natural gas transport [102]. These bubble interactions are also relevant to geological systems [103], [104].

Prior studies have revealed various patterns of bubble formation when two gas jets injected into a liquid interact with one another:

i. synchronous (both jets produce bubbles in-phase with one another) [89], [92], [105]–[107]
ii. temporally uncoordinated (both jets produce bubbles at points in time which are not coordinated with one another) [105]–[107]

iii. intermittent asynchronous (only one jet forms consecutive bubbles at a time, while the other jet forms no bubbles) [89], [105]

iv. alternating (also known as alternative) (both jets produce bubbles nearly completely out-of-phase with one another) [105]–[108]

A few studies [89], [107] have focused on the synchronous bubbling regime and identified critical flow rates at which it transitions to a temporally uncoordinated regime. Jet interaction studies have also noted that the interaction between jets is reduced if the separation distance between jets is increased [89] or if a barrier is added between the jets [89]. Studies have also applied different data analysis methods to confirm the trends in bubbling pattern, using a variety of mathematical analysis approaches [92], [93], [107]. Among these studies, one attempted to use a coupled nonlinear oscillator model to explain the different synchronicity patterns [92]. The authors coupled the total pressure around the two orifices, explaining that the upward liquid circulation in the vicinity of one jet results in a downward circulation of the liquid further away from the jet, which represses bubble formation at the other orifice.

Some studies [93], [102], [106], [109] have focused on the alternating bubbling regime and revealed that this regime only occurs for a specific range of gas flow rate and separation distance between the nozzles. Also, studies have noted that the hydrodynamic interaction between departing bubbles from twin nozzles in the alternating pattern leads to uniform distribution of bubble sizes in the bubble chain [106]. In one study [106], the authors found out that the range of liquid velocities formed by the bubble chain in alternating bubble departure is smaller than in a case with non-alternating bubble departure. This study also found that the velocity of bubbles just above the nozzles are greater in an alternating pattern than in the case of synchronous bubble departure. In a follow up study from the same authors [102], they identified a dimensionless number governing

the alternating bubble regime in their 3D system, $ABD = \frac{f d_{sep} D_b^2}{\pi d_o^2 u_g}$. In this equation, f is the frequency of bubble breakoff, d_{sep} is the distance between the nozzles, D_b is the bubble diameter, d_o is the orifice (capillary) inner diameter and u_g is the average gas velocity coming from the orifice. This study found that alternating bubbling formed in the range $0.5 < ABD < 0.64$. This criterion explains that the occurrence of the alternating bubbling regime is related to the distance between the nozzles as well as the frequency of the bubble departure. The value of this dimensionless number affects the liquid circulation around the departing bubble to influence the growing bubble over the neighbor nozzle to depart in an alternating fashion.

Prior studies have involved relatively low gas flow rates and low liquid viscosities, leading to mixed capillary numbers $Ca = \frac{\mu_l u_g}{\sigma} < 1$, where μ_l is liquid viscosity and σ is surface tension. Here, we investigate synchronous and alternating bubbling patterns in flow conditions with $Ca >> 1$ and utilize cross-correlation plots to quantify the bubbling pattern. We identify *Ca* and the separation distance between jets normalized by the bubble diameter as key dimensionless parameters determining the regime of jet interaction. We also propose a horizontal coupled simple harmonic oscillator model to capture the alternating bubbling phenomenon, simulating the role of horizontal liquid movement in the pinch-off of bubbles.

4.2 Experimental Methods and Image Processing

In this work, a pseudo-2D rectangular container with a height of 100 cm, width of 20 cm, and depth of 1 cm was used. Liquid was filled up to different heights of 10 and 40 cm in the system. The liquids used were (i) distilled water (density $\rho_l = 1000$ kg/m^3, surface tension with air $\sigma = 0.072$ N/m) and (ii) silicone oils (Millipore Sigma) with densities $\rho_l = 960$, 971 and 971 kg/m^3, $\sigma = 0.0209$, 0.0212 and 0.0215 N/m and viscosities of $\mu_l = 0.096$, 0.97 and 9.7 Pa s, respectively.

Air was injected from two separate gas lines through two separate vertical nozzles at the base of the system at constant pressure of 1.38 barg. Air flow came from two separate sources and was controlled by two separate rotameters (Omega FLDA3214G), each with a flow range of 0.5 to 5.0 L/min and accuracy of ±5%. The inner diameter of each nozzle was d_o = 4.5 mm and array of nozzles with a separation distance of d_{sep} = 20 mm between the center of each nozzle was used. All the experiments were recorded using a high-speed camera PROMON 750 from Digital West Imaging at 500 frames per second with a resolution of 0.800 mm (horizontal) and 0.975 mm vertical with a field-of-view of 480 mm (horizontal) and 780 mm (vertical).

To determine bubble formation and breakoff from orifices, the signal intensity of grayscale images in regions 0.5 mm tall and 4.5 mm wide directly above the orifices were evaluated. Fig. 4.1 shows a grayscale image of bubbles emerging from two orifices with red boxes indicating the regions in which signal intensity was evaluated. Fourier Transforms (FTs) were applied to plots of signal intensity vs. time to evaluate the dominant frequency of bubble breakoff from each orifice. Cross-correlation plots were made from the signal intensity plots from the two orifices to determine the time lags between the two plots which produced the highest and lowest values of cross-correlation. These time lags were normalized by multiplying them by the dominant frequency of bubble breakoff. For the case of synchronous bubble formation and breakoff, the cross-correlation plot will have a maximum at a normalized time lag of 0 and a minimum at a normalized time lag of 0.5, and thus the ratio of cross-correlation values $S_{0.5}/S_0$ will be below 1. For alternating bubble formation and breakoff, the maxima and minima will occur at normalized time lags of 0.5 and 0, and thus the ratio $S_{0.5}/S_0$ will be greater than 1. For temporally uncoordinated bubble formation and breakoff, there should not be significant maxima or minima in the cross-correlation plot, and thus $S_{0.5}/S_0$ will be approximately equal to 1.

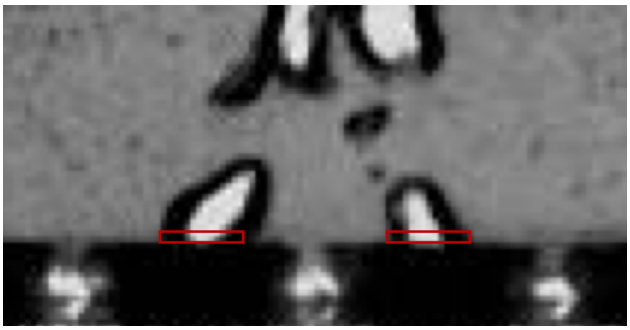

Figure 4.1. Grayscale image of bubbles emerging from interacting gas jets, showing in red boxes the regions used to evaluate signal intensity to determine bubble formation and breakoff at each orifice.

Error bars for cross correlation ratio, bubble breakoff frequency, and bubble breakoff area are calculated by dividing the entire video into three sections, calculating those three parameters for each of the three sections, and then calculating the standard deviation of the three values for each parameter. The size of the error bars is the standard deviation of the three values.

4.3 Results and Discussion

4.3.1 Identification and Quantification of Regimes of Jet Interaction

Fig. 4.2 (a) shows a time series of optical images of bubbles emerging and rising from both orifices at $d_{sep}/d_o = 4.4$ and mixed Capillary number, $Ca = \frac{\mu_l u_g}{\sigma} = 7.2$, where u_g is the gas velocity through the orifice. These images show that bubbles break off from the two orifices in an alternating pattern such that one bubble is growing at the left orifice while the bubble at the right orifice is breaking off. Following this, the next bubble grows at the right orifice while the initial bubble at the left orifice breaks off, and after this, the cycle repeats itself.

Fig. 4.2 (b) shows the image grayscale intensity around the left and right ports indicated in Fig. 4.2 (a) over a time frame of 150 ms. Fig. 4.2 (b) demonstrates that signal intensity increases as a bubble grows at an orifice, and then the signal intensity decreases when a bubble breaks off

from an orifice. Fig. 4.2 (c) shows the Fourier transform (FT) of Fig. 4.2 (b) over a time frame of 120 s for both orifices with vertical line showing the dominant frequency for bubble breakoff, based on the maximum in the FT power spectra. Fig. 4.2 (d) shows the cross-correlation of the area curves over 120 s with the time delay normalized by multiplying it by the dominant bubble breakoff frequency shown in Fig. 4.2 (c). For this plot, the alternating bubble pattern makes it such that there is a minimum in the cross-correlation signal at a normalized delay time of 0, S_0, and a maximum at a normalized delay time of 0.5, $S_{0.5}$.

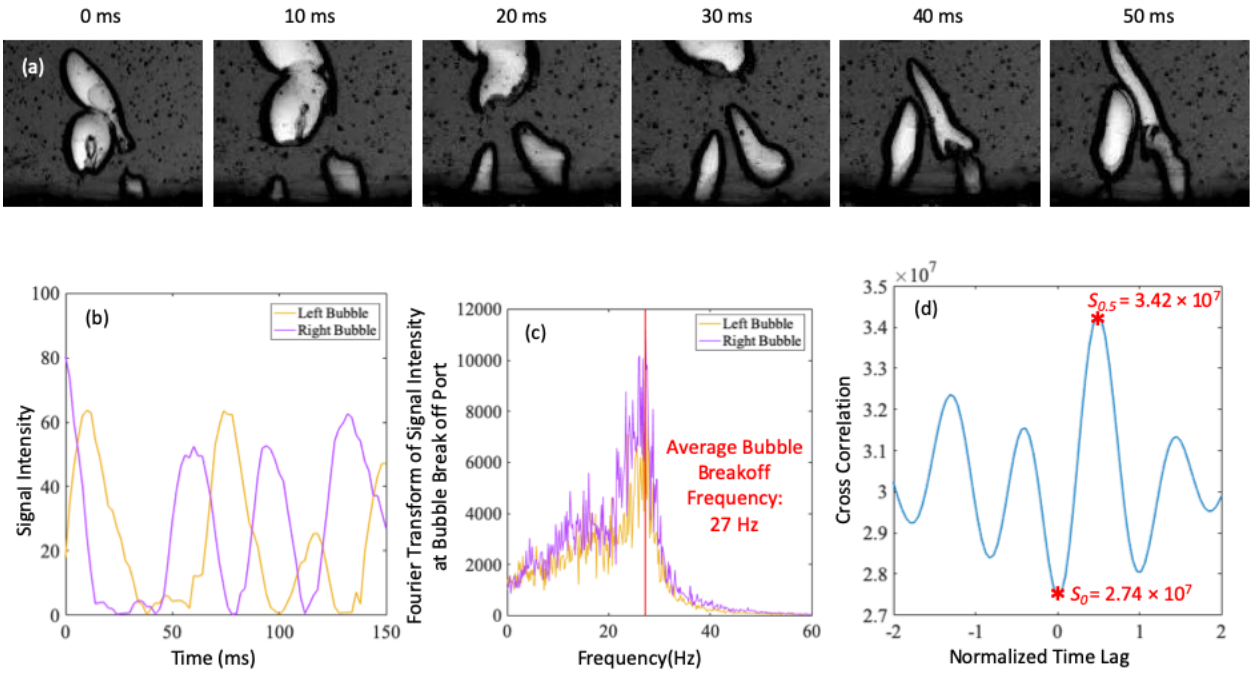

Figure 4.2. (a) Time series of images showing bubbles rising from two orifices through silicone oil with μ = 0.096 Pa s; d_{sep}/d_o = 4.4; flow rate = 1.5 L/min. (b) Signal intensity of the liquid in a region near the left and right orifices over 150 ms processed from the images for the case shown in (a). (c) Fourier transform (FT) of Fig. 2 (b) over a time frame of 120 s for both orifices with vertical lines showing the dominant frequency for bubble breakoff from each orifice. (d) Cross-correlation of the area curves over the time frame of 120 s with the time delay normalized by the average of the dominant bubble breakoff frequencies for the left and right orifices (27 Hz).

Fig. 4.3 shows equivalent images and plots to those in Fig. 4.2, but for a case with a higher viscosity fluid, resulting in a higher mixed Capillary number, Ca. Fig. 4.3 (a) shows a time series of optical images of bubbles emerging and rising from both orifices at $d_{sep}/d_o = 4.4$ and $Ca = 95$. Despite a lower flow rate, larger bubbles form in the case in Fig. 4.3 than those in Fig. 4.2, causing bubbles from the two orifices to coalesce. The images in Fig. 4.3 show that bubbles form and break off from the two orifices in a synchronous pattern, which we can quantitatively verify from the signal intensity and cross-correlation plots, which ultimately quantify that there is a maximum at normalized time lag of 0, S_0, and a minimum at normalized time lag of 0.5, $S_{0.5}$.

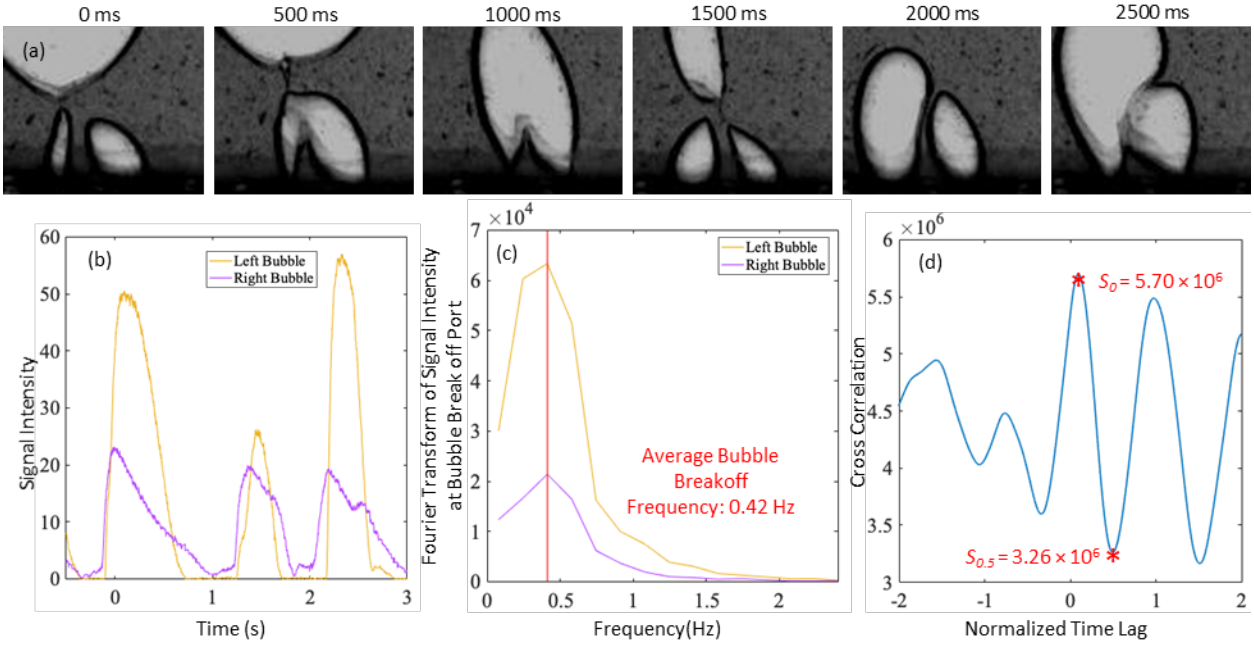

Figure 4.3. (a) Time series of images showing bubbles rising from two orifices through silicone oil with μ = 9.71 Pa s; d_{sep}/d_o = 4.4; flow rate = 0.2 lpm. (b) Signal intensity of the liquid in a region near the left and right orifices over 3 s processed from the images for the case shown in (a). (c) Fourier transform (FT) of (b) over a time frame of 120 s for both orifices with a vertical line showing the dominant frequency for bubble breakoff. (d) Cross-correlation of the area curves over the time frame of 120 s with the time delay normalized by the dominant bubble breakoff frequency (0.42 Hz).

Fig. 4.4 shows equivalent images and plots to those in Fig. 4.2, but for a case with a larger separation distance between jets, resulting in d_{sep}/d_o = 17 and Ca = 7.2. The time series of images in Fig. 4.4 (a) and the signal intensity over time in Fig. 4.4 (b) indicate that there is no clear correlation in time between when bubbles form and break off at the two orifices. These insights are confirmed by the fact that over the entire 120 s of imaging, Fig. 4.4 (d) shows no significant peaks and valley in the cross-correlation plot, and thus $S_{0.5}/S_0 \sim 1$.

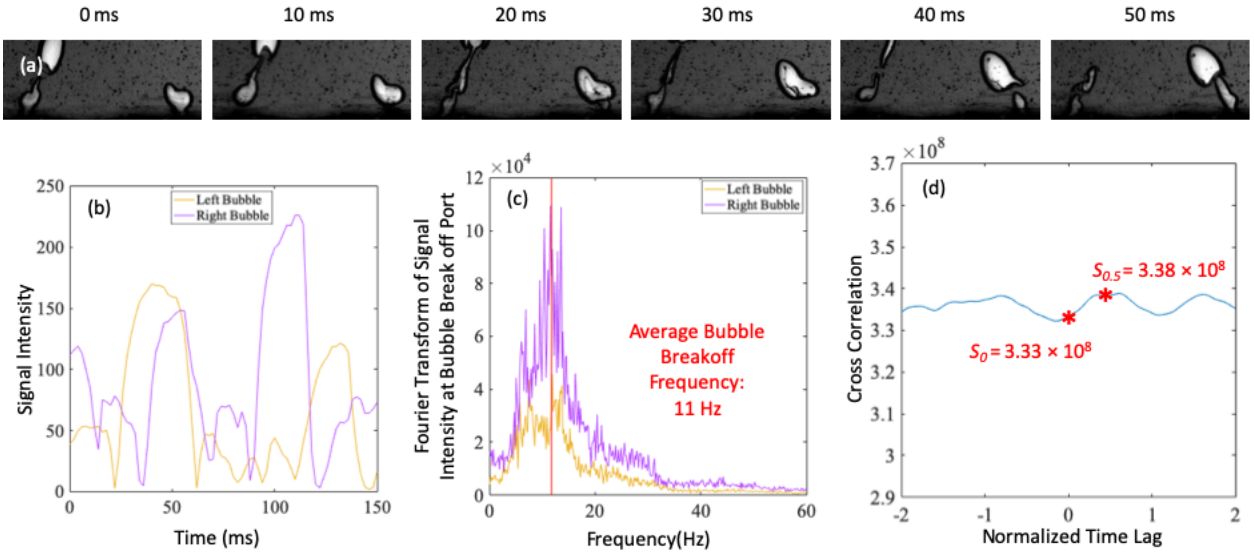

Figure 4.4. (a) Time series of images showing bubbles rising from two orifices through silicone oil with μ = 0.096 Pa.s; d_{sep}/d_o= 17; flow rate = 1.5 lpm. (b) Signal intensity of the liquid in a region near the left and right orifices over 150 ms processed from the images for the case shown in (a). (c) Fourier transform (FT) of (b) over a time frame of 120 s for both orifices with a vertical line showing the dominant frequency for bubble breakoff. (d) Cross-correlation of the area curves over the time frame of 120 s with the time delay normalized by the dominant bubble breakoff frequency (11 Hz).

From inspection of experimental images of jet interaction, such as those shown in Figures 2-4, we discern the following trends:

i. Bubble size increases with increasing gas flow rate and liquid viscosity [110].

ii. When bubble size is large enough and separation distance is low enough such that bubbles overlap regularly, the bubbles coalesce leading to synchronous bubble breakoff [93], [105].

iii. When bubble size is large enough and separation distance is close enough such that bubbles come close to overlapping, but bubbles do not actually overlap, alternating bubble breakoff occurs [93], [105], [107], [108].

iv. When bubble size is small enough and separation distance is far enough that bubbles do not come to overlapping, there is little to no correlation in the timing of bubble breakoff events between the two jets [105], [107].

Based on observations in Fig. 4.2-4.4, we postulate that a mixed Capillary number, $Ca = \frac{\mu_l u_g}{\sigma}$, can characterize the size of bubbles which break off across different flow conditions. Figs. 4.5 (a) and (c) show bubble breakoff frequency vs. *Ca* for the jet interaction conditions studied for (a) 10 cm liquid depth and (c) 40 cm liquid depth. The results show that *Ca* collapses breakoff frequency data across a variety of liquid viscosities, orifice separation distances and gas flow rates. These plots demonstrate that bubble breakoff frequency decreases with increasing *Ca* due to viscous forces dominating over surface tension forces, such that larger bubbles can form over a slower time period. Further, results are nearly identical for different liquid depths, which can be attributed to bubble breakoff being determined by flow near the orifice without significant convection effects caused by liquid and bubbles higher in the system. Figs. 4.5 (b) and (d) shows bubble area calculated using Eq. 1 vs. *Ca*:

$$A_b = \frac{\pi u_g d_o^2}{4fD} \qquad (1)$$

In Eq. 1, A_b is the bubble area, f is the bubble breakoff frequency and D is the depth of the pseudo-2D flow system, 10 mm. These plots demonstrate that bubble area increases with increasing Ca, since more gas enters the bubbles with increasing gas flow rate and there is more time for gas to enter the bubble before bubble breakoff with increasing viscosity and decreasing surface tension. This increase in area with increasing Ca is also seen via inspection of images of experimental results. The data in Fig. 4.5 is not perfectly collapsed onto a single curve, indicating that more dimensionless parameters may be needed to fully capture bubble formation sizes and frequencies. However, the collapse is strong enough across a wide range of gas flow and liquid viscosity conditions to indicate that the mixed Ca number introduced is a strong factor in determining bubble formation properties.

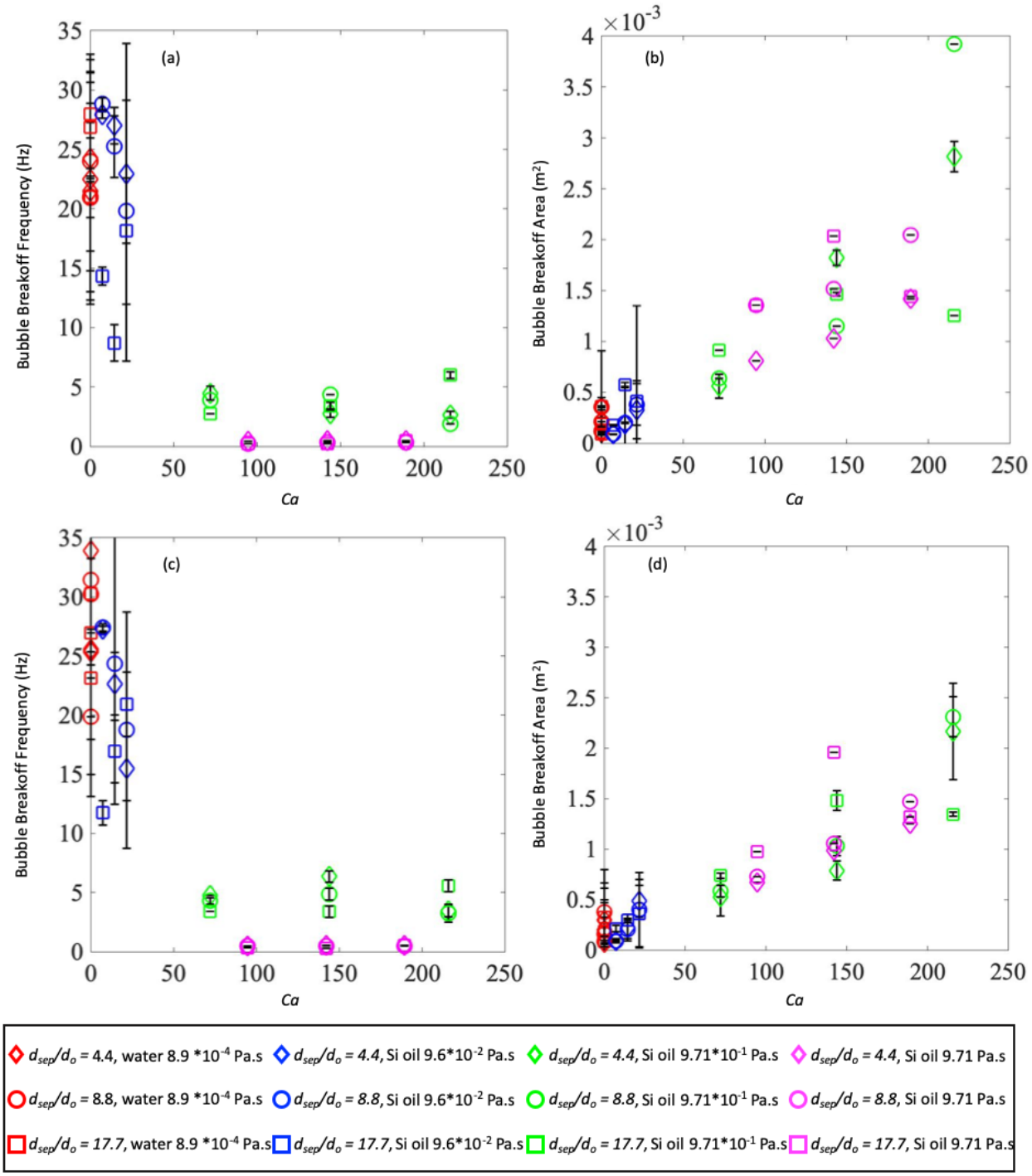

Figure 4.5. (a,c) bubble breakoff frequency vs. Ca, (b, d) calculated bubble breakoff area (Eq. 1) vs. Ca for two jets at (a, b) 10 cm liquid depth and (c, d) 40 cm depth.

From the bubble area in Eq. 1, the effective bubble diameter can be calculated according to $D_{b.eff} = \sqrt{4A_b/\pi}$. Figure 4.6 shows cross correlation ratio vs. effective bubble diameter

normalized by separation distance ($D_{b,eff}/d_{sep}$) for (a, b) low viscosity fluids and (c, d) high viscosity fluids and liquid depths of (a, c) 10 cm and (b, d) 40 cm. Results show that for values of $D_{b,eff}/d_{sep}$ from 0-1, the cross-correlation ratio increases from 1.0 to 1.5-2 with increasing $D_{b,eff}/d_{sep}$ in the low viscosity fluids. Few data points are available with $D_{b,eff}/d_{sep} > 1$ for the low viscosity fluids, since the flow patterns become too turbulent at higher gas flow rates to discern bubble breakoff patterns with image analysis. We attribute the behavior seen in the low viscosity fluids to jets not influencing one another when the separation distance is much greater than the bubble diameter, and thus there being no correlation between bubble breakoff ($S_{0.5}/S_0 \sim 1$). However, when bubble diameter approaches the separation distance, growing bubbles will cause bubbles at the neighboring jet to break off, causing the bubbles to break off in an alternating pattern ($S_{0.5}/S_0 > 1$), as seen in Fig. 4.2.

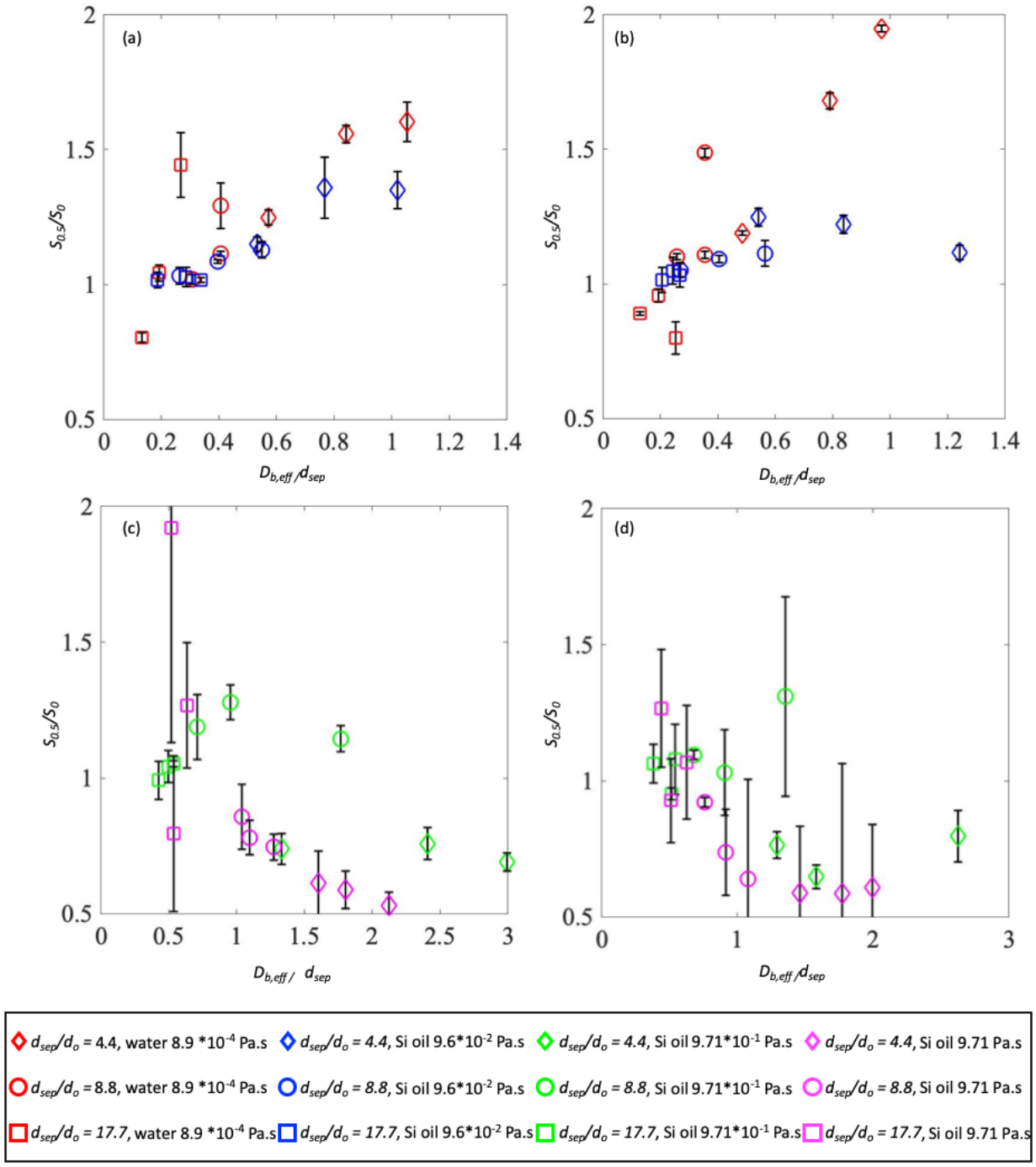

Figure 4.6. Cross correlation ratio vs. effective bubble diameter normalized by separation distance ($D_{b,eff}/d_{sep}$) for (a, b) low viscosity fluids and (c, d) high viscosity fluids and liquid depths of (a, c) 10 cm and (b, d) 40 cm. Data for water and silicone oils are shown.

In the high viscosity fluids, for cases with $D_{b,eff}/d_{sep} > 1$, $S_{0.5}/S_0 < 1$, and this ratio decreases with increasing $D_{b,eff}/d_{sep}$. We attribute this behavior to jets beginning to coalesce in this regime of $D_{b,eff}/d_{sep} > 1$, and thus jets beginning to behave like a single jet from which bubbles pinch off synchronously, as seen in Figure 4.3. $S_{0.5}/S_0$ does not follow a clear trend in the high viscosity fluids with $D_{b,eff}/d_{sep} < 1$, and we were not able to achieve conditions with very low values of $D_{b,eff}/d_{sep}$ for the high viscosity fluids, since bubbles did not form in these fluids below certain gas flow rates.

In cases where $D_{b,eff}/d_{sep} \sim 1$, there are some cases in which there is an alternating bubble pattern ($S_{0.5}/S_0 > 1$), others with no correlation in bubble breakoff events ($S_{0.5}/S_0 \sim 1$) and others with a synchronous bubbling pattern ($S_{0.5}/S_0 < 1$). We attribute this behavior to the fact that not all bubbles formed are circular, as assumed in the equation for $D_{b,eff}$. In cases of low *Ca* (low viscosity fluids), bubbles tend to have a taller aspect ratio, leading to less overlap between bubbles, which produces an alternating bubble pattern. In cases of high *Ca* (high viscosity fluids), bubbles tend to have a wider aspect ratio, leading to bubble coalescence which produces a synchronous bubbling pattern.

4.3.2 Harmonic Oscillator Model

Figure 4.7 shows a schematic time series of bubble breakoff images demonstrating the proposed physical mechanism creating the alternating bubble breakoff phenomenon. This figure is adapted from Penn et al. [31], who proposed a similar mechanism for bubble breakoff from jets in fluidized beds. As the left bubble grows (a), it pushes liquid away from it, causing liquid between the two jets to move to the right. Due to the incompressible nature of the liquid, this right moving liquid must cause the interface of the right bubble to move to the right, such that the right bubble pinches off as the left bubble grows. When the following right bubble starts to grow (b) due to air

flow through the right orifice, it then pushes central liquid to the left, causing the left bubble to pinch off. After this, the cycle repeats itself (c). Based on this mechanism, the continuous fluid would have to be compressible or the gas flow would have to drive more upward flow of central continuous fluid than horizontal flow to allow for synchronous bubble pinch-off. Thus, with the incompressible continuous fluid used here, synchronous bubble breakoff was only observed when jets from both orifices coalesced.

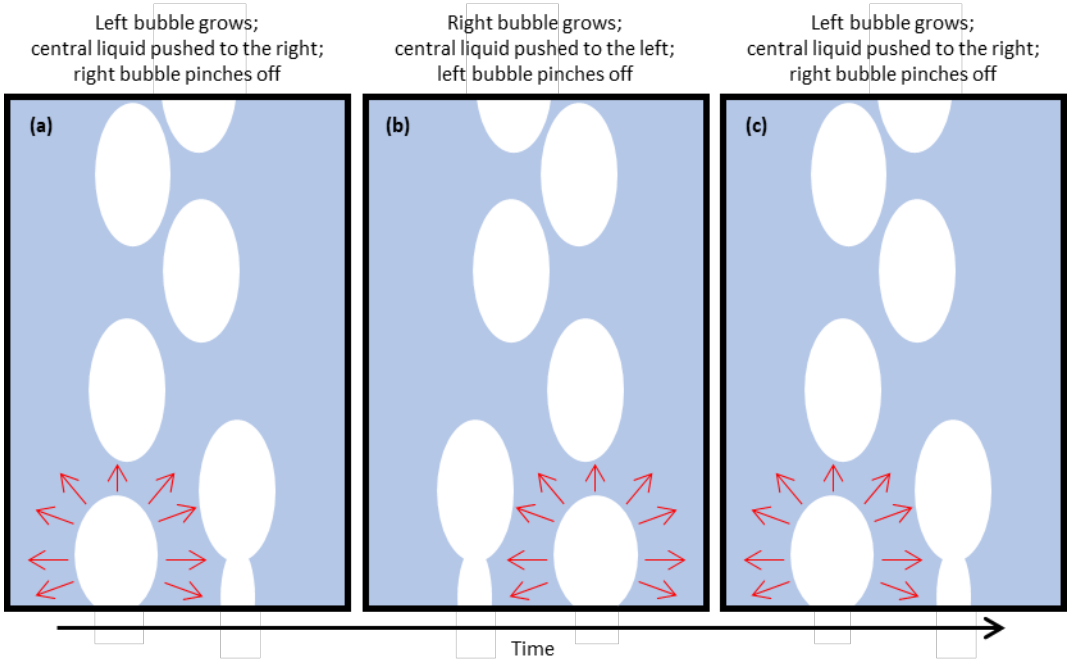

Figure 4.7. Schematic time series of bubble breakoff images demonstrating the proposed physical mechanism creating the alternating bubble breakoff phenomenon. Adapted from Penn et al. [31].

Based on the proposed physical mechanism and the oscillatory nature of the bubble breakoff, we propose a simplified model of the phenomenon corresponding to two coupled harmonic oscillators attached to dampened springs and each driven by an oscillatory external force as shown schematically in Figure 4.8. The equations of motion for this model are given by

$$m\ddot{x}_1 = -k_{out}x_1 + k_{in}(x_2 - x_1) - c_{out}\dot{x}_1 - c_{in}(\dot{x}_1 - \dot{x}_2) + A_0 cos(\omega_0 t - \phi_1) \quad (2)$$

$$m\ddot{x}_2 = -k_{out}x_2 - k_{in}(x_2 - x_1) - c_{out}\dot{x}_2 - c_{in}(\dot{x}_2 - \dot{x}_1) + A_0 cos(\omega_0 t - \phi_2) \quad (3)$$

In this model, the central spring corresponds to the liquid between the two jets, and the outer springs correspond to the gas in the jets and the walls correspond to the centers of the two jets. As such, the masses correspond to the cumulative weight of fluid between the two orifices, with mass 1 and mass 2 corresponding to fluid closer to the left and right orifices, respectively. For simplicity, the masses can be thought of as located at the interfaces between the two jets; we make this simplification because it still can capture the alternating or simultaneous bubble pinch-off phenomena while avoiding complications of making the springs possess mass themselves. The spring constants, k_{in} and k_{out}, correspond approximately to the inverse of the compressibility of the liquid and the gas, respectively, while the damping coefficients, c_{in} and c_{out}, correspond approximately to the viscosity of the liquid and the gas, respectively. Further, the driving force the masses corresponds to the oscillating motion of the jet interface for a single isolated jet due to the Kelvin-Helmholtz instability. As such, masses oscillating in-phase with one another corresponds to bubbles forming and breaking off out-of-phase with one another (i.e. the alternating bubble pattern). Masses oscillating out-of-phase with one another corresponds to bubbles forming and breaking off in-phase with one another (i.e. the synchronous bubble pattern). We note that since masses stay separate in this model, the model cannot predict bubble coalescence.

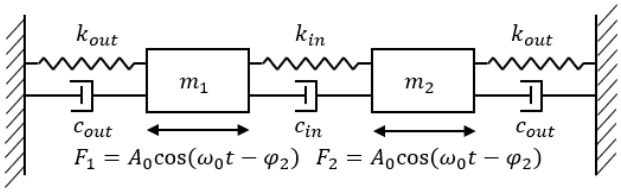

Figure 4.8. A schematic diagram of the coupled harmonic oscillator model.

Figure 4.9 shows a numerical solution to the model in Eqs. 2 and 3. An arbitrary phase offset of the external forcing $\phi_1 - \phi_2 = 0.05\pi$ is used to achieve a steady-state solution which is

not driven by the phase offset, as would only occur if the phase offset were 0 or π. This figure shows that by changing the ratio of k_{in}/k_{out} from 10 to 1000, the model goes from predicting alternating bubbling to synchronous bubbling. We interpret these results by treating the spring constants as an approximate equivalent of the compressibility of the fluid. The results show that for a high spring constant ratio, as is expected for an incompressible continuous fluid and a compressible dispersed fluid, as used here, alternating bubbling can form. Whereas, if the compressibility of the two fluids is more comparable, as if two incompressible fluids or two compressible fluids were used, synchronous bubbling can form.

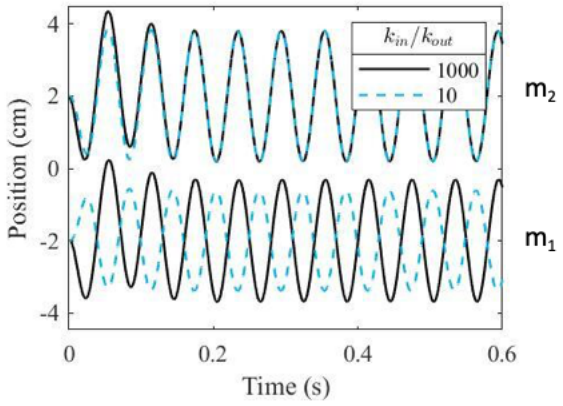

Figure 4.9. Model results for positions of the two masses with different values the ratio of inner and outer spring constant used. Model parameters used: m = 0.1 kg; c_{in} = 5 kg/s; c_{out} = 5 kg/s; $\phi_1 - \phi_2$ = 1.05π; ω_0 = 104 s-1. Black solid line: k_{out} = 100 kg/s²; k_{in} = 100000 kg/s². Blue dotted line: k_{out} = 100 kg/s²; k_{in} = 1000 kg/s². The lines oscillating between 0 to 4 cm represent the positions of m_2, whereas the lines oscillating between 0 to -4 cm represent the positions of m_1.

Steady-state solutions for the model in Eqs. 2 and 3 are given by

$$x_1 + x_2 = \frac{x_0 \cos\left(\frac{\Delta\phi}{2}\right)}{\sqrt{\left(\left(\frac{\omega_1}{\omega_0}\right)^2 - 1\right)^2 + \left(\frac{\gamma_1}{\omega_0}\right)^2}} \cos\left(\omega_0 t - \bar{\phi} - \tan^{-1}\left(\frac{\gamma_1 \omega_0}{\omega_1^2 - \omega_0^2}\right)\right) \quad (4)$$

$$x_1 - x_2 = \frac{x_0 \sin\left(\frac{\Delta\phi}{2}\right)}{\sqrt{\left(\left(\frac{\omega_2}{\omega_0}\right)^2 - 1\right)^2 + \left(\frac{\gamma_2}{\omega_0}\right)^2}} \sin\left(\omega_0 t - \bar{\phi} - \tan^{-1}\left(\frac{\gamma_2 \omega_0}{\omega_2^2 - \omega_0^2}\right)\right) \quad (5)$$

where substitutions $\omega_1 = \sqrt{\frac{k_{out}}{m}}$, $\omega_2 = \sqrt{\frac{k_{out}+2k_{in}}{m}}$, $\gamma_1 = \frac{c_{out}}{m}$, $\gamma_2 = \frac{c_{out}+2c_{in}}{m}$, $\bar{\phi} = \frac{\phi_1+\phi_2}{2}$, $\Delta\phi = \phi_1 - \phi_2$, are made, and dimensional factor is $x_0 = \frac{2A_0}{m\omega_0^2}$, which, for a given system, only depends on the frequency and amplitude of the driving force. Eqs. 4 and 5 apply to cases where $\omega_0 < \omega_1 < \omega_2$, which is almost always the case for system of fluids with relatively low compressibility as compared to the driving force of jet bubbling.

For this model, if the amplitude of the $(x_1 + x_2)$ solution, A_{1+2}, is much greater than that of the $(x_1 - x_2)$ solution, A_{1-2}, then the central interfaces move to the left synchronously then to the right synchronously, corresponding to the alternating bubble pattern observed in Figure 4.1 (a). Alternatively, if $A_{1+2} << A_{1-2}$, then synchronous bubble breakoff is observed, and if $A_{1+2} \sim A_{1-2}$, then the random phase offset between the driving forces of the two jets determines the phase offset between the two jet interfaces and no systematic bubble breakoff patterning is observed. The ratio of the amplitudes for the two solution modes is given by

$$\frac{A_{1+2}}{A_{1-2}} = \sqrt{\frac{\left(\left(\frac{\omega_2}{\omega_0}\right)^2 - 1\right)^2 + \left(\frac{\gamma_2}{\omega_0}\right)^2}{\left(\left(\frac{\omega_1}{\omega_0}\right)^2 - 1\right)^2 + \left(\frac{\gamma_1}{\omega_0}\right)^2}} \cot\left(\frac{\Delta\phi}{2}\right)$$

Thus, the key dimensionless parameters in determining whether alternating or synchronous bubble breakoff are observed are: $\frac{\omega_1}{\omega_0}$, $\frac{\omega_2}{\omega_0}$, $\frac{\gamma_1}{\omega_0}$, $\frac{\gamma_2}{\omega_0}$ and $\Delta\phi$. The $\cot\left(\frac{\Delta\phi}{2}\right)$ term will be approximately of order 1 unless $\Delta\phi$ is very close to zero, where it diverges, or when $\Delta\phi = \pi$, where it becomes 0. For this study, since the two jets are turned on at the same time, we could suppose $\Delta\phi = \pi$, but in reality, $\Delta\phi$ will change over time due to turbulent effects not accounted for in the oscillator model, and thus we consider this term to be of order 1. For alternating or synchronous bubbling to occur, compressibility or damping of the continuous or dispersed phase must dominate over the

external driving force for motion of the interface, i.e. at least one of the four terms $\frac{\omega_1}{\omega_0}$, $\frac{\omega_2}{\omega_0}$, $\frac{\gamma_1}{\omega_0}$, $\frac{\gamma_2}{\omega_0}$ must be greater than 1. Thus, assessing the value of $\frac{A_{1+2}}{A_{1-2}}$ relative to 1 reduces to assessing the values of $\frac{\omega_2}{\omega_1}$ and $\frac{\gamma_2}{\gamma_1}$. In the case of an incompressible continuous fluid and a compressible dispersed fluid, as studied here, $\frac{\omega_2}{\omega_1} \gg 1$, since $k_{in} \gg k_{out}$ due to the incompressibility of the inner fluid. In the case of a liquid inner fluid and a gas outer fluid, as studied here, $\frac{\gamma_2}{\gamma_1} \gg 1$ since $c_{in} \gg c_{out}$ due to the higher viscosity of liquids than gasses. As such, $\frac{A_{1+2}}{A_{1-2}} \gg 1$, corresponding to the alternating bubble pattern observed in Figure 4.2 (a). In the case that the separation distance between jets is increased, there is more space for fluid between jets to move vertically, effectively reducing ω_2 and γ_2, allowing for the transition from the alternating bubble regime to the random bubble breakoff regime. Increasing gas flow rate is expected to increase ω_0; however, faster motion of fluid between jets is also expected to increase ω_2 and γ_2, and thus the effect of gas velocity (which scales with *Ca*) on bubbling pattern predicted by the harmonic oscillator model is less clear.

It is expected that in the case where both phases are incompressible, $\frac{A_{1+2}}{A_{1-2}}$ will become lower in magnitude, causing alternating bubbling to be observed in fewer cases and potentially enabling synchronous bubbling to be observed. Further, in the case where both phases are compressible, such as in gas-fluidized beds, $\frac{A_{1+2}}{A_{1-2}}$ will also become lower in magnitude, enabling observation of synchronous bubble breakoff as has been reported previously [31] and can be seen predicted by the model in Figure 4.9. We expect that a future parametric study varying continuous and dispersed phase properties, jet velocity and separation distance can provide approximations for how the harmonic oscillator parameters correlate with fluid and flow properties, based on the transitions between alternating bubbling, random bubbling and synchronous bubbling regimes.

4.3.3 Comparison with Prior Research

A prior study has shown an alternating bubble pattern in bubbles emerging from adjacent ports in a microfluidic device [108]. However, this prior patterning [108] is different from that reported here for two critical reasons: (i) Both gas and liquid emerge from the orifices rather than only gas in the system studied here, and thus in the prior study gas emerges from the orifices intermittently. (ii) Just upstream of the orifices, the flow to the two orifices is connected by a T-piece, rather than gas coming from two separate sources in the system studied here. Thus, the prior study [108] accounts for the alternating bubble pattern based on coupled pressure oscillation in the pressure upstream of the orifices, rather than the coupling downstream of the orifices by central liquid shown in Figure 4.8 in this study, and thus the mechanisms for the two phenomena are distinct.

Prior research [31] has shown a synchronous bubble breakoff pattern from jets injected into gas-fluidized granular particles. The system in this prior study is distinct from the system studied here for three critical reasons: (a) There is no surface tension between the gas phase and the fluidized particulate phase. (b) Gas travels freely between the bubbles and the interstices between particles. (c) The fluidized particulate phase is compressible. On this basis, the coupled harmonic oscillator model proposed here could allow for synchronous bubble breakoff in gas-fluidized granular particles, while it does not allow for synchronous bubble breakoff in an incompressible liquid when jets are close together, as studied here.

The studies performed by Dzienis *et al.* [93], [102], [106] and Mosdorf *et al.* [109] are the most similar prior studies to the work presented in this paper, since these prior studies identify the alternating bubble pattern and attribute its formation to interaction between bubbles mediated by liquid separating the bubbles. These studies differ however from ours in flow regime studied, in

that we have investigated a broad spectrum of *Ca* values, including values much greater than 1, while the prior work studied flows with *Ca* values less than 10. Our study has thus added to the strong insights from this prior work in characterizing the importance of *Ca* on flow behavior. Further, our work has introduced a simple harmonic oscillator model to account for coupling between bubbles, while prior work has focused on more complex hydrodynamic motion to characterize coupling. The very recent study of Dzienis *et al.* [102] introduced the dimensionless parameter *ABD* to characterize whether or not alternating bubble patterns would form. This dimensionless parameter is the ratio of two velocities, that of fluid motion between jets, and that of bubble growth at a single jet. Similarly, we have proposed a dimensionless parameter $D_{b,eff}/d_{sep}$ which accounts for a ratio of length scales. Thus, both models account for the bubble size, frequency of bubble breakoff and separation distance between jets; however, Dzienis *et al.* [102] use these parameters to create a ratio of velocities, while here, we create a ratio of length scales. We attribute this difference to the fact that at lower *Ca* values, flow will be faster and thus inertial interactions will be stronger, while at higher *Ca* values, bubbles will mainly interact when they reach length scales needed to nearly overlap with one another.

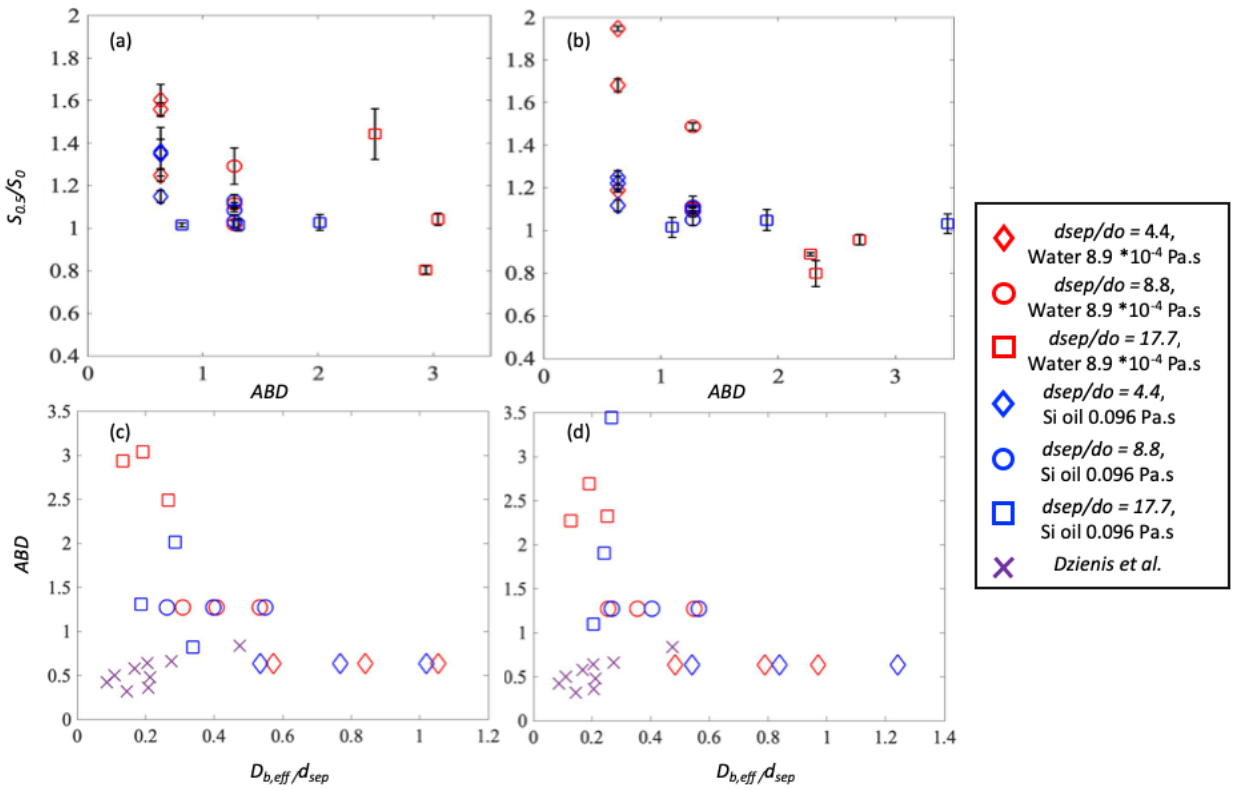

Figure 4.10. $S_{0.5}/S_0$ vs. ABD for low viscosity liquid data for (a) 10 cm and (b) 40 cm liquid height. (c-d) ABD vs. $D_{b,eff}/d_{sep}$ for the data of Dzienis et al. [102] as well as the low viscosity liquid data from this study for liquid heights of (c) 10 cm and (d) 40 cm.

Figure 4.10 (a-b) show $S_{0.5}/S_0$ vs ABD for our data for lower viscosity liquids, demonstrating that $S_{0.5}/S_0$ tends to be somewhat larger than 1 for $0.5 < ABD < 0.64$ and $S_{0.5}/S_0$ is somewhat closer to 1 for $ABD > 0.64$. Thus, the correlation of Dzienis *et al.* [102] stating that alternating patterns form when $0.5 < ABD < 0.64$ fits our data somewhat, but the correlation is not strong. We only compare data with lower viscosity liquids to avoid cases in which bubbles coalesce, which were not considered by Dzienis *et al.* [102]. Figure 4.10 (c-d) show ABD vs. $D_{b,eff}/d_{sep}$ for our data for low viscosity liquids and the data of Dzienis *et al.* [102]. Results show that the prior experiments produced much lower values of ABD for the same value of $D_{b,eff}/d_{sep}$ as the experiments here. The inability of ABD to collapse data from our study and our dimensionless parameters proposed to govern alternating bubbling to collapse data from the Dzienis *et al.* [102]

may be due to the fact that we used pseudo-2D system in which walls affect bubbly dynamics, while Dzienis *et al.* [102] use a 3D system in which wall effects are likely negligible. Further, the difference in the size of orifice (capillary) used in both studies may also play a role in the different parameters governing bubble interaction regime identified in the two studies. These differences can affect the bubble formation and rise behavior and thus cause the discrepancies between the two studies.

Figure 4.11 (a) shows alternating versus non-alternating bubble behavior vs. $D_{b,eff}/d_{sep}$ for the data of Dzienis *et al.* [102]. Results show that $D_{b,eff}/d_{sep}$ cannot capture whether alternating or non-alternating behavior will occur in the data of Dzienis *et al.* [102]. Figure 4.11 (b) shows that for the same value of Ca, the experiments in this paper produce larger values of $D_{b,eff}/d_{sep}$ than those in the Dzienis *et al.* paper. We attribute this difference to the fact that the experiments here used a pseudo-2D system with an orifice diameter four times larger than that in the experiments of Dzienis *et al.* [102]. Thus, we postulate that dimensionless parameters which account for orifice diameter more directly may be needed to characterize flow regimes across a wide range of flow conditions.

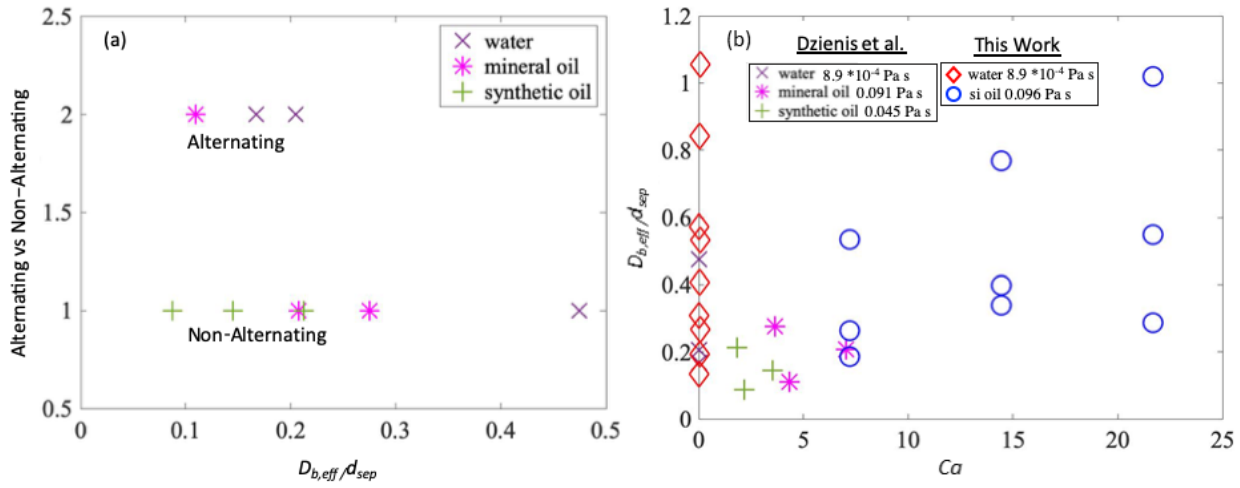

Figure 4.11. (a) Alternating vs. non-alternating bubbling patterns as a function of $D_{b,eff}/d_{sep}$ for the data of Dzienis et al. [102]. (b) $D_{b,eff}/d_{sep}$ vs. Ca for the data of Dzienis et al. [102] as well as the low viscosity liquid data acquired for this study.

Another potentially critical difference between the work presented in this paper and that of Dzienis *et al.* [102] is that our work uses orifices which are flush with a solid plate at the bottom of the liquid container, while that of Dzienis *et al.* [102] has orifices at the end of vertical tubes which penetrate into the liquid container. As such, bubbles produced in this work have no fluid below them to influence pinch-off, while those in the Dzienis *et al.* [102] work do have fluid below them, as shown schematically in Figure 4.12. We leave it to future work to investigate how critical this geometric difference is in the bubble pinch-off and interaction behavior, and whether or not making this flow geometry consistent can help to collapse data across studies and across a dimensionless parameter.

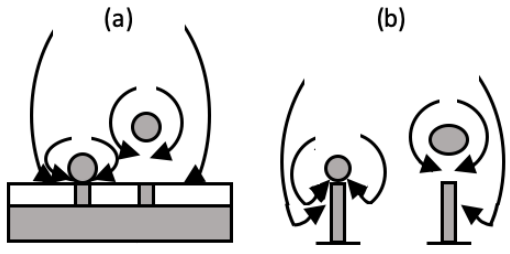

Figure 4.12. Schematic of injection setup for (a) this paper and (b) Dzienis *et* al. [102] paper.

Thus, a comparison with Dzienis *et al.* [102] demonstrates that neither ABD nor $D_{b,eff}/d_{sep}$ can fully capture the alternating vs. non-alternating bubble behavior across all the experimental data in the two papers. We attribute the differences in the two papers to (1) the difference between the 2D system in our experiment vs 3D system in Dzienis *et al.* paper, (2) experiments at values of *Ca* much higher than 1 were conducted here, (3) different values of orifice diameter were used in the two sets of experiments and (4) different placement of orifices. We leave it to future work to study if the insights between the two studies can be combined into a unified theory based on a study which conducts both 2D and 3D experiments, a wider range of flow conditions and orifice diameters. Such a study could potentially identify dimensionless parameters which govern alternating behavior on a fuller data set, and we expect that a dimensionless parameter which involves orifice diameter more directly, such as d_o/d_{sep}, will be needed.

4.4 Conclusion

In summary, this paper reports the finding of an alternating bubble breakoff pattern observed in two gas jets injected into an incompressible liquid when jets interact but do not coalesce. The extent of alternating vs. synchronous bubble pinch-off is quantified based on digital image analysis, showing that the ratio of the effective bubble diameter at the time of bubble breakoff to the separation distance between orifices ($D_{b,eff}/d_{sep}$) dictates the regime of jet interaction. The effective bubble diameter correlates with a capillary number for the system. When $D_{b,eff}/d_{sep} < 1$, jets are far away from one another and bubbles are small, causing the jets to not interact significantly and thus causing bubble breakoff events to be independent from one another at the two orifices. When $D_{b,eff}/d_{sep} > 1$, bubbles coalesce and break off synchronously as if they were coming from a single orifice. When $D_{b,eff}/d_{sep}$ is just less than one, bubbles from both jets come close to on another without coalescing, such that growing bubbles from one orifice push

liquid to the other orifice, causing bubble breakoff. This mechanism leads to the alternating bubble breakoff pattern reported here. This proposed mechanism is used to build a coupled harmonic oscillator model which predicts qualitatively the onset of the alternating bubble patterns when distance between jets is decreased. Comparison with the insights and data of shows that future work will require experimentation in both 2D and 3D system across a wider range of Dzienis *et al.* [102] flow conditions and orifice diameters to determine the full set of dimensionless parameters needed to capture regimes of jet interaction, including alternating bubbling.

Chapter 5 : Periodically Structured Coalescence of Bubbles in a Shear-Thickening Suspension

This chapter was previously submitted to *Physical Review Letter* journal and is in revision.

5.1 Introduction

Bubbles rise, split and coalesce with one another in liquids, having critical effects on interphase heat and mass transport as well as liquid mixing. Plumes or jets of bubbles injected through a single nozzle into a liquid occur in a variety of natural [103], [111] and industrial [98], [112]–[114] processes. Air bubbles injected vertically as a jet into a Newtonian liquid exhibit uniform size and spacing between bubbles at low flow rates, but have non-uniform unstable behavior at higher flow rates due to bubble coalescence [115]. Single bubbles rising in dense suspensions of spheres and in shear-thickening fluids have been shown to have dynamics heavily dependent on Stokes number [116] and the extent of shear-thickening [117], respectively. Further, bubble rise velocities in dense suspensions can be faster than those in a pure liquid with equivalent density due to particle migration [118].

Cornstarch-water suspensions exhibit highly non-Newtonian behavior, involving shear-thinning at low shear rates (~0.01-1 s^{-1}) and shear-thickening at higher shear rates (> 1 s^{-1}) [119], including discontinuous shear-thickening when the volume fraction of cornstarch is above 40% [119]–[122], leading to a variety of flow phenomena [119]–[126]. Dense spheres descending through these suspensions have been shown to undergo oscillatory descent velocities [127], or rebound and remain on the suspension surface [128] depending on flow conditions. Strongly vibrated cornstarch suspensions have been shown to sustain indented holes persistently [129]. Air injection into a horizontally-oriented Hele-Shaw cell filled with a cornstarch-water suspension has been shown to exhibit distinct regimes of viscous fingering and fracture [116].

In this chapter, we investigate the injection of a vertical jet of gas into cornstarch-water suspensions, forming a stream of bubbles, and report repeating coalescence of these bubbles in space and time under specific conditions. We demonstrate that regular coalescence leads to the size, shape and position of bubbles in a stream repeating itself periodically. The regular coalescence and periodic repetition are observed only under particular suspension and gas flow conditions. We attribute the regular coalescence to the shear-dependent rheology of fluid surrounding leading and trailing bubbles, where the fluid transitions locally from shear-thinning to shear-thickening behavior.

5.2 Methods

A pseudo-2D rectangular container 20 cm wide, 100 cm high and 1 cm deep was used. In the first part of the experiment, air was injected through a vertical nozzle at the base of the system at constant pressure of 1.4×10^5 Pa, and its flow was controlled using a rotameter (Omega FLDA3214G). The inner diameter of the nozzle was d_o = 4.5 mm. Gas flow rate was changed to achieve $Fr = u_o^2 g^{-1} d_o^{-1}$ values of 6.2 to 1.6×10^2, where u_o is gas velocity through the nozzle. In the second part of the experiment, consecutive air bubbles were injected via solenoid valve through the same vertical nozzle. We varied the injection time and the time interval between each injection. The cornstarch suspension was prepared using cornstarch (Millipore Sigma) and distilled water at different volumetric fractions of 10, 20, 30, 35, 40 and 44%. In some cases, CsCl was added to the water to create a suspension in which the density of the liquid matched the density of the cornstarch. The cell was filled with the suspension to a height of 60 cm. For comparison with a Newtonian fluid with a similar viscosity to the cornstarch suspensions, silicone oil with 0.096 Pa s viscosity was also used. All experiments were recorded using a high-speed camera PROMON 750 from Digital West Imaging at 500 frames per second and resolution of 0.800 mm (horizontal)

and 0.975 mm vertical with a field-of-view of 480 mm (horizontal) and 780 mm (vertical). Images were binarized into liquid- and gas-phase regions, and bubble area was determined by summing the areas of interconnected gas-phase pixels. Vertical bubble position was based on the height of the centroid of a bubble above the nozzle. Bubble width was determined based on the longest horizontal distance between interconnected gas-phase pixels. Bubble coalescence events were determined based on when two sets of interconnected gas-phase pixels first overlapped with one another. For each case, images were acquired over a period of 120 s. The frequency of bubble coalescence and bubble breakthrough were based on the frequency with a maximum in the Fourier Transform (FT) of plots of coalescence events vs. time and bubble motion through the top layer of pixels vs. time, respectively.

5.3 Results and Discussion

For a case of gas injection at $Fr = 25$ into a 40 vol% cornstarch solution, bubbles are found to coalesce periodically at three vertical positions in the system (Figure 5.1). The time-averaged bubble area increases with increasing vertical distance above the nozzle due to bubble coalescence, and at two vertical regions, 0-50 mm (Region 1) and 150-250 mm (Region 2), the bubble area increases rapidly with increasing vertical position, indicating large amounts of coalescence (Figure 5.1 (a)). In contrast, almost no coalescence occurred in the region 50-150 mm above the nozzle. Under these flow conditions, bubbles formed at the nozzle at a frequency of approximately 15 Hz. FTs of bubble coalescence vs. time plots in these two regions indicate that coalescence occurs at frequencies of 7.4 Hz and 3.7 Hz in Regions 1 and 2, respectively (Figure 5.1 (b)). Time series of images every 7.4 Hz (Figure 5.1 (c)) show that initially formed bubbles at the nozzle coalesce at a 7.4 Hz frequency at the same position low in the bed (white circles). Larger bubbles formed from the lower coalescence event coalesce every two images in the same upper position in the system

(green circles). Further, high in the system, bubbles appear to regularly coalesce at ¼ the frequency of the coalescence low in the bed (red circles), indicating that the coalescence events occur periodically at regular positions which persist high into the system.

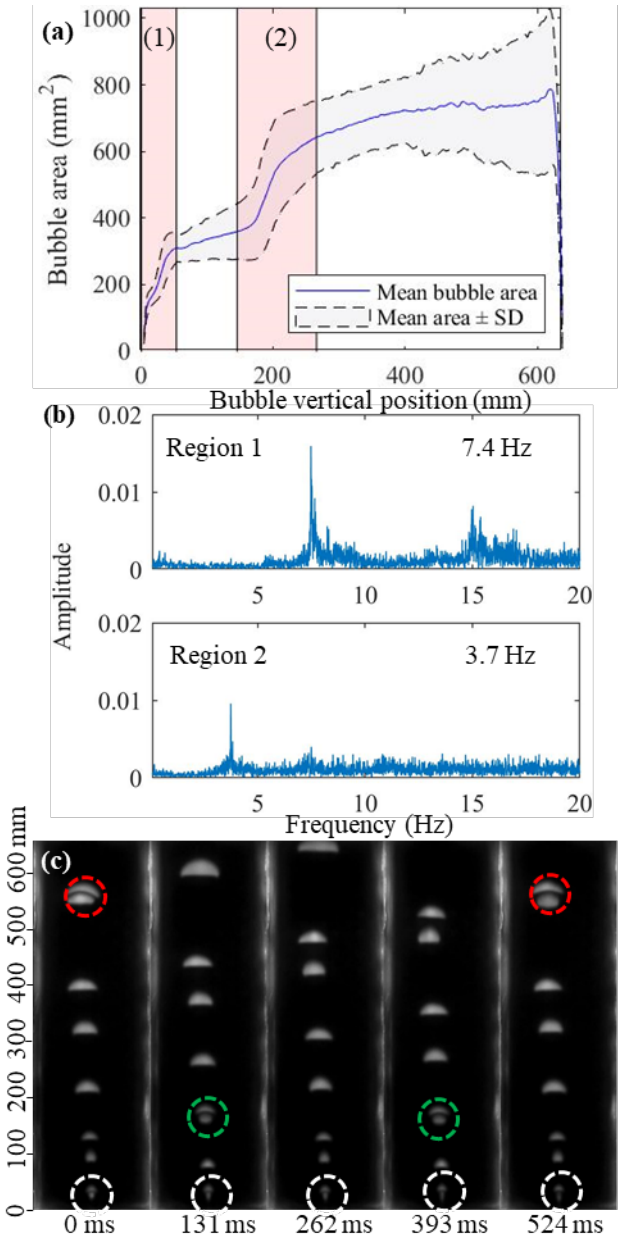

Figure 5.1. Characterization of bubbling from an air jet in a 40 vol% cornstarch-water suspension with Fr = 25. (a) Average bubble area vs. bubble vertical position, showing the standard deviation with the dotted lines and highlighting Regions 1 and 2 of bubble coalescence in red. (b) FTs of bubble coalescence vs. time plots in the two regions, indicating the dominant frequency of bubble coalescence in each region. (c) Time series of images of

bubble dynamics shown with a frequency of 7.4 Hz, circling points of periodic coalescence in three vertical regions. Under these flow conditions, bubbles formed at the nozzle at a frequency of approximately 15 Hz.

The periodic coalescence at the same vertical positions seen for the flow conditions in Figure 5.1 was no longer observed when flow conditions (suspension concentration, gas flow rate) were changed, indicating that specific flow conditions are needed to achieve regular coalescence. Figure 5.2 shows that while many other flow conditions lead to bubble area increasing with increasing vertical position, indicating bubble coalescence, only the case shown in Figure 5.1, which appears as the black curve in Figure 5.2, has multiple regions of rapid bubble increase in area, indicating regular coalescence. As such, we assert that particular gas flow conditions together with a particular rheological behavior of fluid are required to achieve this regular bubble coalescence.

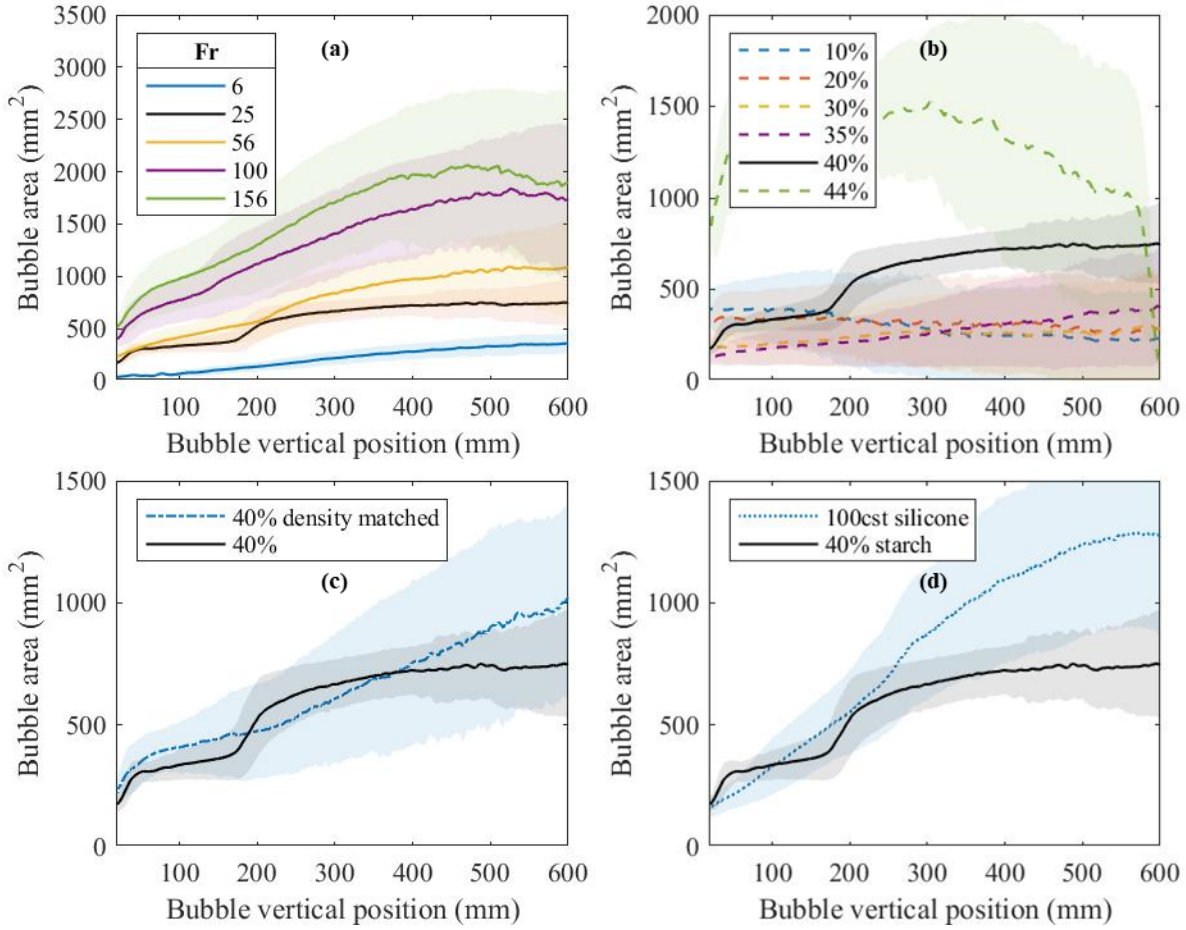

Figure 5.2. Bubble area vs. vertical bubble position for a 40 vol% cornstarch-water suspension at Fr = 25 (black line) as compared with other flow conditions: (a) different gas flow rates, same 40 vol% suspension (b) different vol% of cornstarch, same Fr (c) a density-matched 40 vol% cornstarch suspension, same Fr and (d) silicone oil with a viscosity of 0.096 Pa s, same Fr.

The regular coalescence flow conditions in Figure 5.1 also lead to bubble streams with the same shapes, sizes and positions repeating themselves periodically in the system. This periodicity can be determined based on the frequency of bubble breakthrough the liquid surface, which is 1.9 Hz in this case (Figure 5.3 (a)). This frequency of bubble breakthrough is ¼ and ½ that of bubble coalescence in Regions 1 and 2, corresponding to the three coalescence events that occur throughout the height of the system, as seen in Figure 5.1 (c). Time series of images shown with frequency of 1.9 Hz demonstrate nearly identical bubble stream configurations repeating themselves, even when no coalescence is occurring in the images (Figure 5.3 (b)).

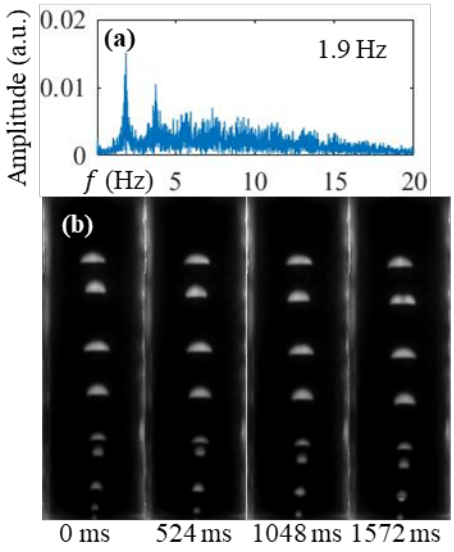

Figure 5.3. (a) FT of bubble breakthrough for the same regular coalescence case shown in Fig. 1. (b) Time series of images of bubbling for the same case shown at a frequency of 1.9 Hz.

The Pearson correlation coefficient [130] can be used to quantify the degree of periodic structure repetition in the system by assessing the similarity between images separated by the time period of bubble breakthrough. For a variety of liquid conditions and values of *Fr*, only the case shown in Fig. 5.1 and Fig. 5.3 and one other flow condition (44% cornstarch, *Fr* = 25) yield a correlation coefficient greater than 0.5, indicating a high degree of periodically repeating structure in bubble shape, size and position (Fig. 5.4). Investigation of the 44% cornstarch, *Fr* = 25 case demonstrated that while it had repeated bubble structuring, it did not undergo bubble coalescence and thus did not involve the regular coalescence shown in Fig. 5.1 (c). We attribute the lack of coalescence to the high particle concentration inhibiting bubble coalescence in the 44% cornstarch case.

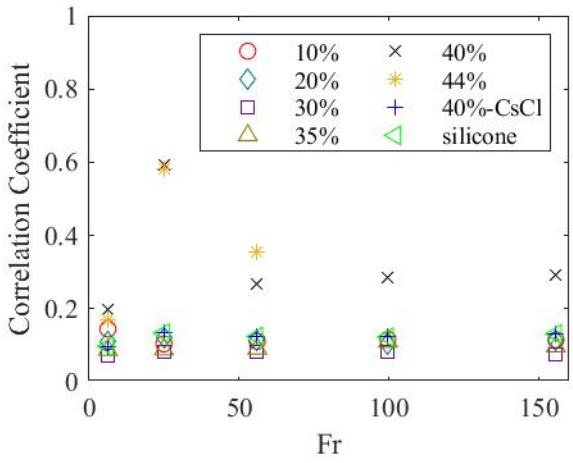

Figure 5.4. Correlation coefficient vs. Fr for a variety of fluid conditions: cornstarch suspensions with vol% of (i) 10, (ii) 20, (iii) 30, (iv) 40, and (v) 44, (vi) a density-matched 40 vol% cornstarch suspension and (vii) silicone oil with viscosity of 0.096 Pa s.

The physical mechanisms underlying the regular coalescence case in Figs. 5.1 and 5.3 can be better understood by investigating the dynamics of leading and trailing bubbles in the regions of regular coalescence just prior to coalescence (Fig. 5.5). We approximate the shear rate of fluid surrounding leading bubbles just prior to coalescence by dividing bubble rise velocity by bubble width (Fig. 5.5 (a)). By plotting these shear rates vs. the experimentally measured (Anton Paar MCR 302 Rheometer) effective viscosity of this cornstarch-water suspension, we see that these shear rates in the regular coalescence regions all lie in a shear rate regime high enough for strong shear-thickening to occur in the surrounding fluid. As such, leading bubbles decelerate just prior to coalescence in Regions 1 and 2 (Fig. 5.5 (b,c)). The leading bubbles are wider than the trailing bubbles in the regular coalescence regions (Fig. 5.5 (d)), and thus the trailing bubbles are shielded from drag by the leading bubbles. Analysis of the slow-motion videos shows that, in both regions, leading bubbles develop into a wide spherical cap shape because bubble coalescence above them leaves leading bubbles relatively unaffected by bubbles above them, while trailing bubbles are closer to leading bubbles above them, causing trailing bubbles to rise in a narrower shape. Since fluid is pulled upward in the wake of leading bubbles, trailing bubbles experience a lower relative

velocity to surrounding fluid, and thus the fluid surrounding trailing bubbles is likely in a shear-thinning regime. As such, the trailing bubble accelerates (Fig. 5.5 (b,c)), causing the trailing bubble to have a higher rise velocity than the leading bubble (Fig. 5.5 (e,f)). Thus, the trailing bubble catches up to the leading bubble, and the bubbles coalesce. In comparison, for the rare cases in which bubbles coalesce outside of these regular coalescence regions, the leading bubble is not systematically in either the shear-thinning or shear-thickening regime (Fig. 5.5 (a)). Further, analysis of the approximate shear rate and viscosity in fluid surrounding bubbles at the same *Fr* in suspensions with other cornstarch concentrations show that bubbles are not rising through fluid at the start of a shear-thickening regime, further demonstrating the need of shear-thickening to cause regular bubble coalescence.

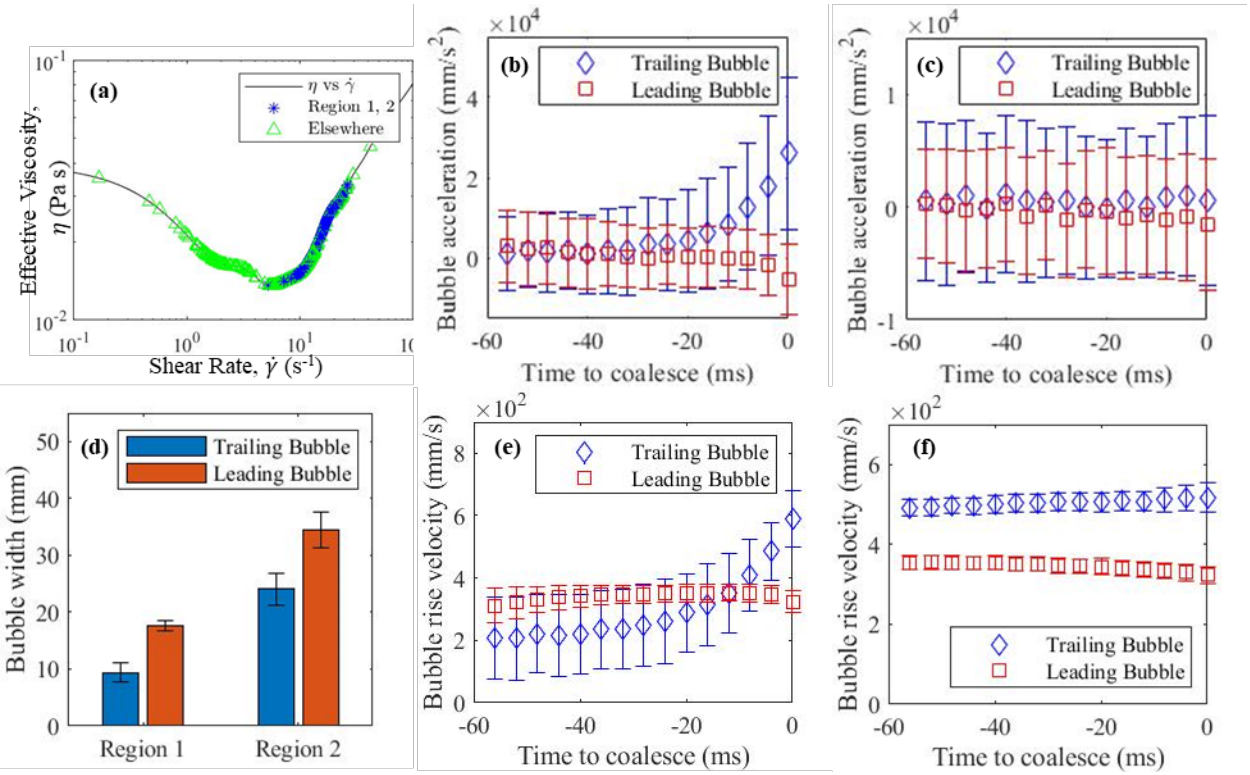

Figure 5.5. Dynamics of leading and trailing bubbles at points in time just prior to bubble coalescence for the regular bubble coalescence case shown in Figs. 5.1 and 5.3. (a) Effective viscosity vs. shear rate for the suspension (line) and approximated shear rate of fluid surrounding the leading bubble just prior to coalescence (markers). Average vertical bubble

acceleration (b,c) and average bubble rise velocity (e,f) vs. time before coalescence in Region 1 (b,e) and Region 2 (c,f). (d) Average bubble widths just before coalescence in the two regions.

Regular coalescence can be created for a range of controlled bubble sizes using solenoid valves (SMC Pneumatics Series VQ20/30) with varying times of opening and closing the valves to control the size and frequency of bubble injection (Fig. 5.6). The regions of rapid increase in bubble area with increasing vertical position indicate regular coalescence, and results show that increasing bubble injection time while keeping the same injection frequency increases bubble area while keeping the same coalescence points (Fig. 5.6 (a)). Further, keeping a constant injection time while varying injection frequency allows for the positions of coalescence to be controlled (Fig. 5.6 (b)).

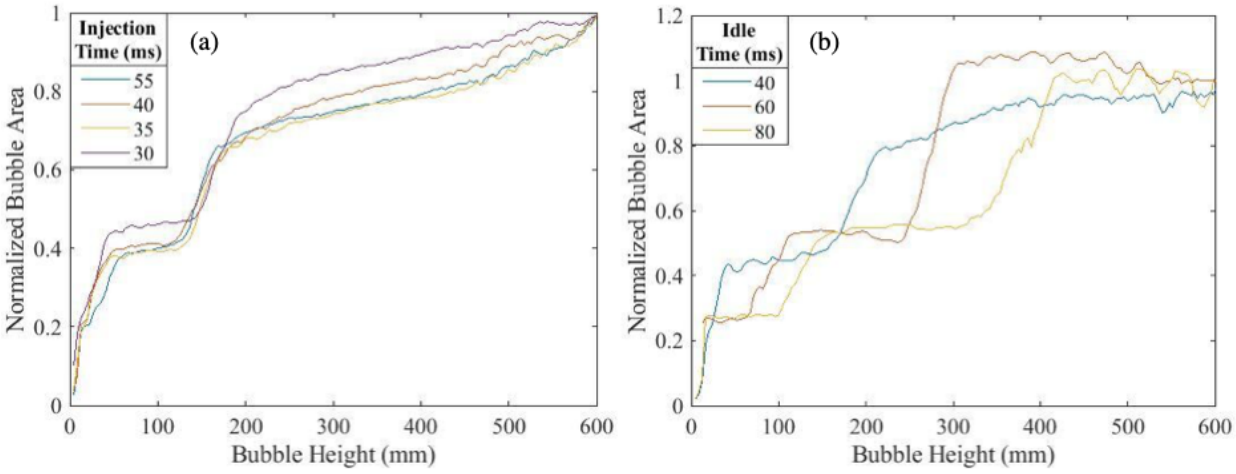

Figure 5.6. Normalized bubble area vs. vertical bubble position for a 40 vol% cornstarch-water suspension for (a) bubbles injected at a frequency of 15 Hz with varying bubble injection time, forming initial bubbles of different areas and (b) bubbles injected for the same amount of time but different idle time between injections, creating bubbles at different frequencies.

5.4 Conclusion

Taken altogether, the results in this chapter show that the transition to a heavily shear-thickening regime at higher shear rates in cornstarch-water suspensions is key to having leading bubbles decelerate in certain regions, causing regular, periodic coalescence, and this coalescence

can be controlled by manipulating gas injection conditions. Regular coalescence is not observed for Newtonian fluids or other cornstarch-water suspensions because for the liquids in which shear-thickening regimes exist, these regimes do not exist at the proper shear-rate conditions for the range of gas flow rates studied here. Particular combinations of bubble size and bubble formation rate are needed to achieve regular coalescence because these two factors are key to creating leading bubbles which enter a shear-thickening regime at locations in which trailing bubbles are close enough to leading bubbles to create regular coalescence.

This identification and understanding of regular coalescence can be used to test complex rheological models for cornstarch-water suspensions [131]–[136]. Further, this discovery can also be used to identify other conditions for potential regular coalescence in other fluids with strong shear-thickening regimes. Manipulation of gas injection can be used to tailor the regular coalescence properties for desired behavior in industrial devices. Ultimately, we expect that regular coalescence can be used in a variety of shear-thickening fluids in industry to optimize mass transport and liquid mixing for a range of applications.

Chapter 6 : Dynamics of Single Bubbles in Cornstarch-Water Suspensions

This chapter was previously submitted to the Journal of *Non-Newtonian Fluid Mechanics*.

6.1 Introduction

A wide variety of processes in nature and industry involve bubbles rising through non-Newtonian fluids, such as shear-thinning polymer solutions. Unlike bubbles in Newtonian fluids which tend to grow as they rise, proceed toward a final shape and terminal velocity [137], bubbles in non-Newtonian fluids can oscillate in rise velocity [7], [8] and shape [9], [10]. Further, these bubbles can form complex shapes never seen before in Newtonian fluids [9], [138], [139]. Such bubble dynamics can be used to probe the rheological behavior of these complex fluids by understanding the balance of forces at play when the fluids are under shear due to bubble rise. Further, these bubble dynamics have critical effects on the mixing of fluids as well as heat and mass transport and chemical reactions in systems ranging from chemical reactors [4], [140], [141] to volcanos [142]. Therefore, to design and optimize the process equipment involving bubbly flows in non-Newtonian fluids, it is crucial to predict these dynamics such as the bubble rise velocity [143] by understanding how they originate from bubble and fluid properties.

For the past few decades, many studies have revealed that the non-Newtonian behavior of the continuous phase has a significant impact on the bubble shape and bubble rise behavior. Some studies have involved bubbles in liquids [143]–[147], while others have studied bubble rise in particle-laden suspensions [148]–[151]. One of the latter studies on bubble rise in a granular suspension by Hooshyar et al. [151] highlights the effect of suspended particle size on the rising motion of a gas bubble. At low particle sizes and thus low Stokes numbers, bubble rise was only indirectly affected by particles, since particles increased the effective viscosity of the suspension

as compared to a pure liquid. In contrast, at large particle sizes and thus large Stokes numbers, particles collided directly with bubbles, changing the direction trajectory of bubbles and providing another method of energy dissipation via inelastic collisions. Thus, the average rise velocity of the bubble decreased with increasing solid volume fraction in this prior study.

As compared to other non-Newtonian fluids, the rise of bubbles in shear-thickening fluids has not received a significant amount of academic study. The authors are only aware of a couple prior studies of bubble rise in shear-thickening fluids [143], [144]. Battistella et al. [143] studied the shape of a single bubble in power law fluids including both shear-thinning and shear-thickening fluids using a Front-Tracking CFD model. For bubbles in both shear-thinning and shear-thickening fluids, the front and wake of the bubble are the regions of higher shear, creating lower viscosity in shear-thinning fluids and higher viscosity in shear-thickening fluids in these regions. For the case of shear-thinning fluid, the sphericity of the bubble decreases, and the bubble rises in a wobbling motion. Whereas for a shear-thickening fluid, the bubble shape is more spherical due to the increased viscosity in the fluid surrounding the bubble, and the bubble rises in a straight line similar to a bubble rise in a more viscous fluid. Ohta et al. [145] studied the rising motion of a bubble in a shear-thickening fluid by using a CLSVOF method [152], [153], and they revealed that the high viscosity regions formed above the bubble are wider than those below the bubble. In contrast, the decrease in viscosity for the shear-thinning case occurs over a wider region around the bubble and mainly below the bubble rather than above the bubble.

The aforementioned studies have also shed light on bubble rise motion in shear-thinning and shear-thickening fluids. Ohta et al. [145] found out that a bubble in a shear-thinning fluid rises faster than an identical bubble in a corresponding Newtonian fluid due to the lower viscosity above the former bubble. In contrast, the rise velocity of a bubble in a shear-thickening fluid is slower

than that in a Newtonian fluid due to the increased viscosity in the region above the bubble. This shear-thickening effect suppresses the wake behind a bubble and leads to a narrow region of increased viscosity around the bubble. Similarly, Battistella et al. [143] found out that in a highly shear-thickening fluid, the bubble rise terminal velocity decreases (bubble Re decreases) due to higher viscosity effects around the bubble.

In this paper, we investigate the rise behavior and shape of a gas bubble in a cornstarch-water suspension at different particle packing fractions, causing some bubbles to rise through a suspension in a shear-thinning regime and others to rise through a suspension in a slightly shear-thickening regime. For comparison with a Newtonian fluid with similar viscosity to the cornstarch-water suspensions, silicone oil with 0.096 Pa s and 0.0093 Pa s viscosities were also used. For the cases studied, wobbling behavior was dictated by Bo and Re, rather than Newtonian vs. non-Newtonian behavior.

6.2 Experimental Methods

A pseudo-2D rectangular container was constructed with PMMA (polymethyl methacrylate) with a vertical length of 100 cm, width of 20 cm and depth of 1 cm. Air was injected in the system using solenoid valves through a vertical nozzle with inner diameter of d_o = 4.5 mm at the base of the system at different pressures of 5, 15, and 25 psig. The solenoid valve is pilot operated and in order to open it a power input of 2.9 W and a voltage of 12 VDC must be applied to release the piston. A LabVIEW interface was used to control the valve. The injection time was set to 10 ms (meaning the duration of the time interval where the solenoid valve was open was 10 ms). A National Instruments data acquisition card was used as an interface between the computer and the solenoid valve. Also, a transistor-based electrical circuit was designed to connect an external 12 VDC power source to the solenoid valve.

The experimental setup contained a dense mixture of cornstarch particles and demineralized water. The cornstarch suspension was prepared using cornstarch (Millipore Sigma) and distilled water at different volumetric fractions of 5, 10, 20, 30, 40 and 44%. Suspensions were thoroughly mixed and allowed to equilibrate for a couple of hours and then re-mixed again prior to the experiment. The cell was filled with the suspension to a height of 60 cm. For comparison with a Newtonian fluid with a similar viscosity to the cornstarch suspensions, silicone oil with two different viscosities of 0.096 Pa s and 0.0093 Pa s were also used. All the experiments were recorded using a high-speed camera PROMON 750 from Digital West Imaging at 500 frames per second and resolution of 0.800 mm (horizontal) and 0.975 mm vertical with a field-of-view of 480 mm (horizontal) and 780 mm (vertical). Images were binarized into liquid- and gas-phase regions. Vertical bubble position was determined based on the height of the centroid of a bubble above the nozzle. Bubble rise velocity (u_b) was calculated based on difference between two consecutive vertical position of the bubble (height of the centroid) divided by the time step of the optical imaging measurements (2 ms). The amplitude of the rise velocity was calculated by taking half of the average of the difference between the maximum and the minimum rise velocity for each period of oscillation. In order to calculate the bubble diameter, first the bubble area (A_b) was determined by summing the areas of interconnected gas-phase pixels. Then, the equivalent bubble diameter (d) was calculated based on diameter of a circle with the same area as our bubble ($d = \frac{4A_b}{\pi}$). Lastly, bubble orientation was plotted determining the angle between the horizontal axis and the major axis of the bubble. The width of the bubble was determined as the horizontal distance between the left-most pixel in a bubble and the right-most pixel in a bubble. The viscosity measurements in Fig. 7 were obtained using Anton Paar MCR 302 Rheometer. The samples were prepared in the same fashion as for the single bubble injection experiments. A parallel plate geometry with 50 mm

and 25 mm diameter plates were used for lower packing fractions (5-30 vol%) and higher packing fractions (40-44 vol%), respectively. The rheology was measured in a shear rate control mode for $0.05 \leq \phi \leq 0.30$ and stress control mode for $0.4 \leq \phi \leq 0.44$. In shear rate control mode, shear stress was measured as a dependent variable responding to a step-wise increase in shear rate. In stress control mode, shear rate was measured as a dependent variable responding to a step-wise increase in stress with an adjustment time of 5 s and measurement duration of 5 s. To approximate the viscosity of fluid surrounding a bubble, the shear rate was approximated by dividing the average rise velocity of the bubble by the average width of the bubble.

6.3 Results and Discussion

Figures 6.1-6.3 show the trajectories and shapes of single bubbles as they rise through the different liquids after injection at (1) 5 psi, (2) 15 psi and (3) 25 psi for cornstarch-water suspensions with cornstarch vol% of (a) 0%, (b) 5%, (c) 10%, (d) 20%, (e) 30%, (f) 40% and (g) 44%. For comparison, silicone oils with viscosities of (h) 9.3 mPa s and (i) 96 mPa s are shown. The bubbles increase in size significantly with increasing injection pressure, since more air is injected, but the bubbles are fairly similar in size across different fluids, since essentially same amount of air is injected. For the smallest bubbles (Figure 6.1), the bubbles adopt ellipsoidal shapes for the cornstarch-water suspensions and spherical cap shapes in the silicone oils. The bubbles tend to "wobble", changing in orientation and horizontal position, in low packing fraction cornstarch-water suspensions, but this wobbling is not apparent in the 40% cornstarch-water suspension and the silicone oils. No plot is shown for the 5 psi, 44% case, since no bubble formed under these conditions. Figures 6.2 and 6.3 show that larger bubbles adopt spherical cap shapes in all fluids except for the 44% case in which they adopt ellipsoidal shapes. Wobbling is not apparent for these larger bubbles.

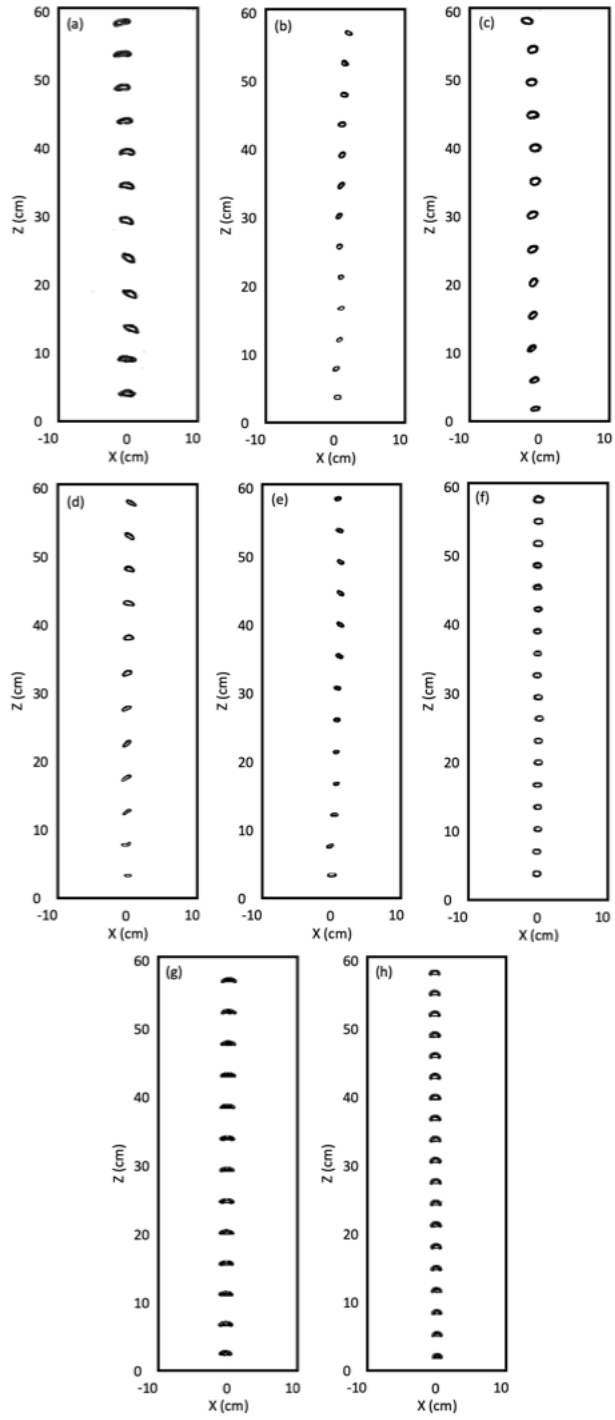

Figure 6.1. Bubble rise shape and trajectory at 5 psi: (a) 0%, (b) 5%, (c) 10%, (d) 20%, (e) 30%, (f) 40%, (g) silicone oil 9.3 mPa s, (h) silicone oil 96 mPa s.

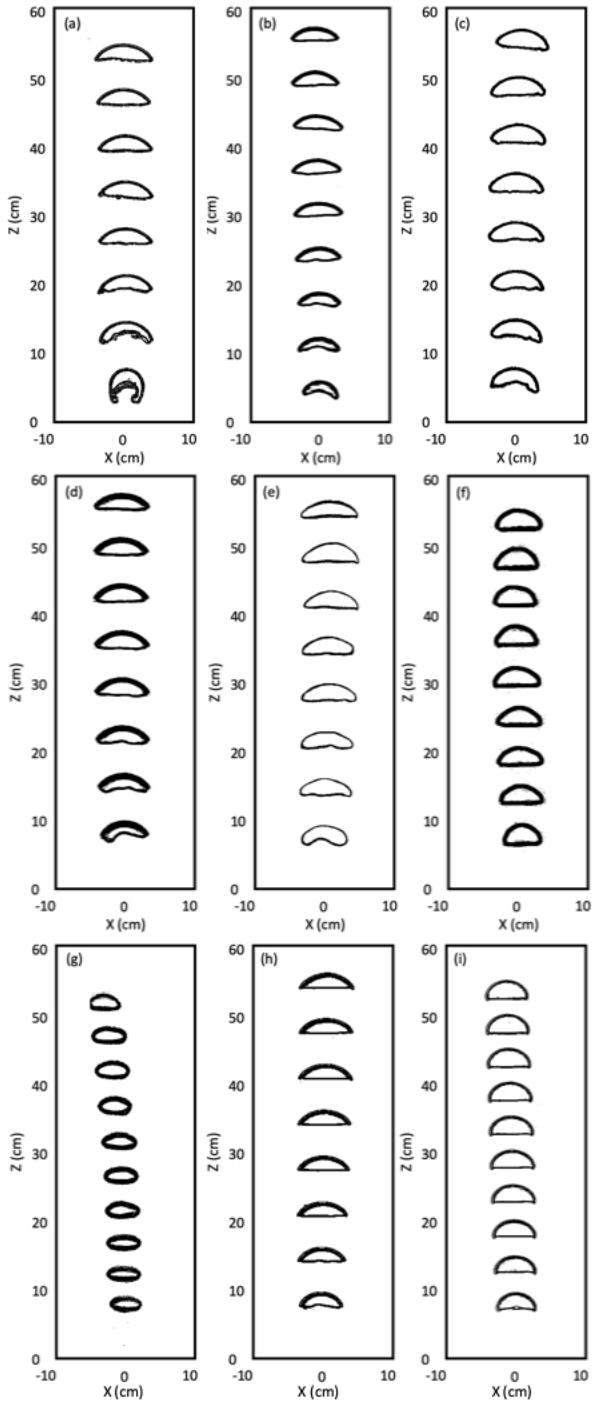

Figure 6.2. Bubble rise shape and trajectory at 15 psi: (a) 0%, (b) 5%, (c) 10%, (d) 20%, (e) 30%, (f) 40%, (g) 44%, (h) silicone oil 9.3 mPa s, (i) silicone oil 96 mPa s.

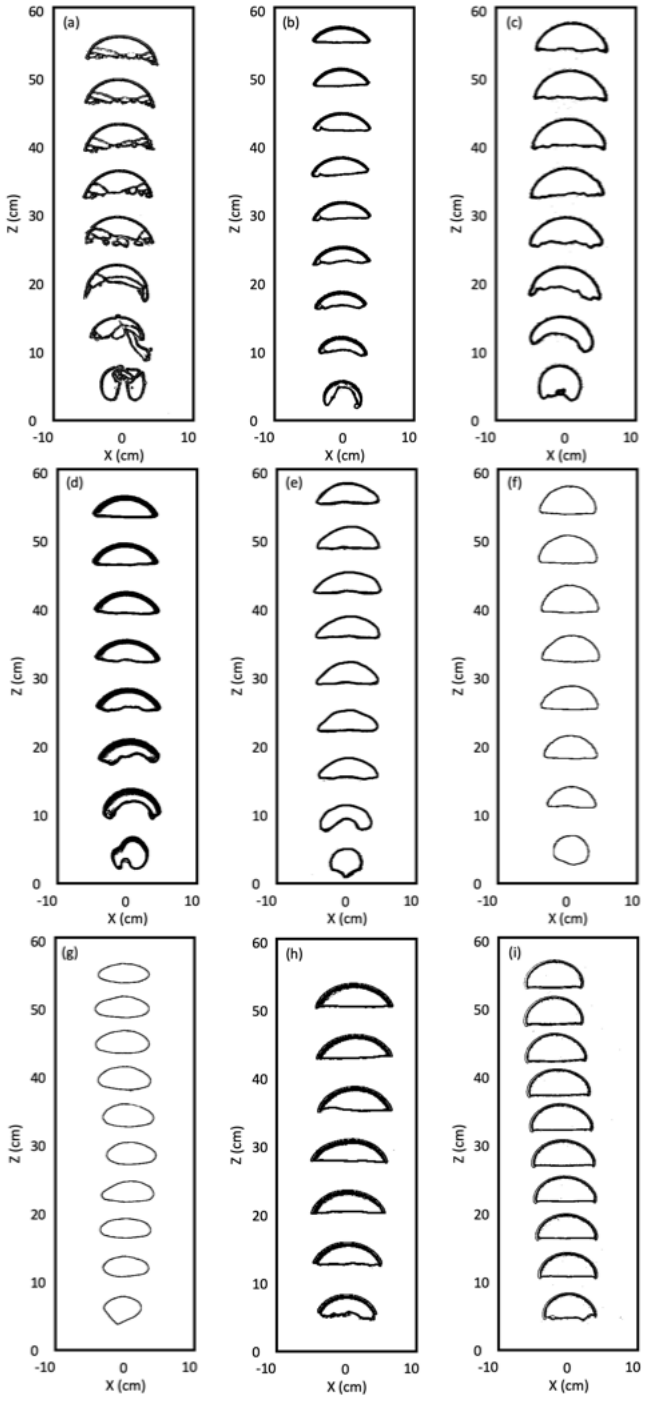

Figure 6.3. Bubble rise shape and trajectory at 25 psi: (a) 0%, (b) 5%, (c) 10%, (d) 20%, (e) 30%, (f) 40%, (g) 44%, (h) silicone oil 9.3 mPa s, (i) silicone oil 96 mPa s.

Figure 6.4 quantifies the orientation (first row) and the rise velocity (second row) vs. time for the 5 (first column), 15 (second column) and 25 (third column) psi cases. For the case of 5 psi,

we can observe that the air bubble in water and low packing fraction of cornstarch wobbles as it rises, oscillating in its orientation and rise velocity. Our finding is in an agreement with the finding of Grace et al. [154] where at relatively high Re and intermediate Bo number, bubbles have an ellipsoidal shape. According to Grace et al. [154] for $4.2 < d < 17$ and $1510 < Re < 4700$, the path of a bubble is rectilinear but with rocking (wobbling), which confirms our finding for the motion of bubble in water at 5 psi. Also, Battistella et al [143] showed in their numerical study that bubbles in both shear-thinning and Newtonian liquids oscillate in their rise velocity due to their wobbling behavior. As we increase the packing fraction from 30 vol% to 40 vol%, we observe that the value of rise velocity drops significantly due to the high concentrations of particles. This frictional interaction of particles creates similar effects to a highly viscous fluid, suppressing the rocking motion, and therefore no rise velocity oscillation occurs. For comparison, we also experimented silicone oil with different viscosities of 9.3 mPas and 96 mPas. For the lower viscosity oil, we observed an oscillation with small amplitude, while for the higher viscosity oil, no oscillation in the bubble rise was observed. Similar to the cornstarch-water suspensions, the value of the rise velocity decreases as the viscosity of the fluid increases in silicone oil.

At higher air injection pressures of 15 psi and 25 psi, the bubble size increases, and we no longer observe the rocking motion or change in the orientation of the bubble in most cases. For all cases in cornstarch suspensions at these two pressures, the bubble has a spherical cap shape, except for 44 vol% where the bubble has an ellipsoidal shape. In the 44 vol%, the viscosity of the fluid in suspension is higher than the viscosity of fluid surrounding the bubble in other concentrations, making it such that the viscous effects are dominant (as compared to inertial effects). In this case, the bubble forms an ellipsoidal shape due to its low Re and intermediate Bond number [154]. As the bubble size increases, we can also observe that the amplitude of the rise velocity oscillation

decreases for the air bubble in water and also bubble in low suspension packing fractions (5-30 vol%). For both 15 psi and 25 psi injection pressures at high packing fractions (40 vol% and 44 vol%) there is no oscillation as the viscosity of the fluid increases significantly. This increase in viscosity also slows down the speed of bubble rise. Bubbles in rise velocity with increasing injection pressure because of the increase in bubble size.

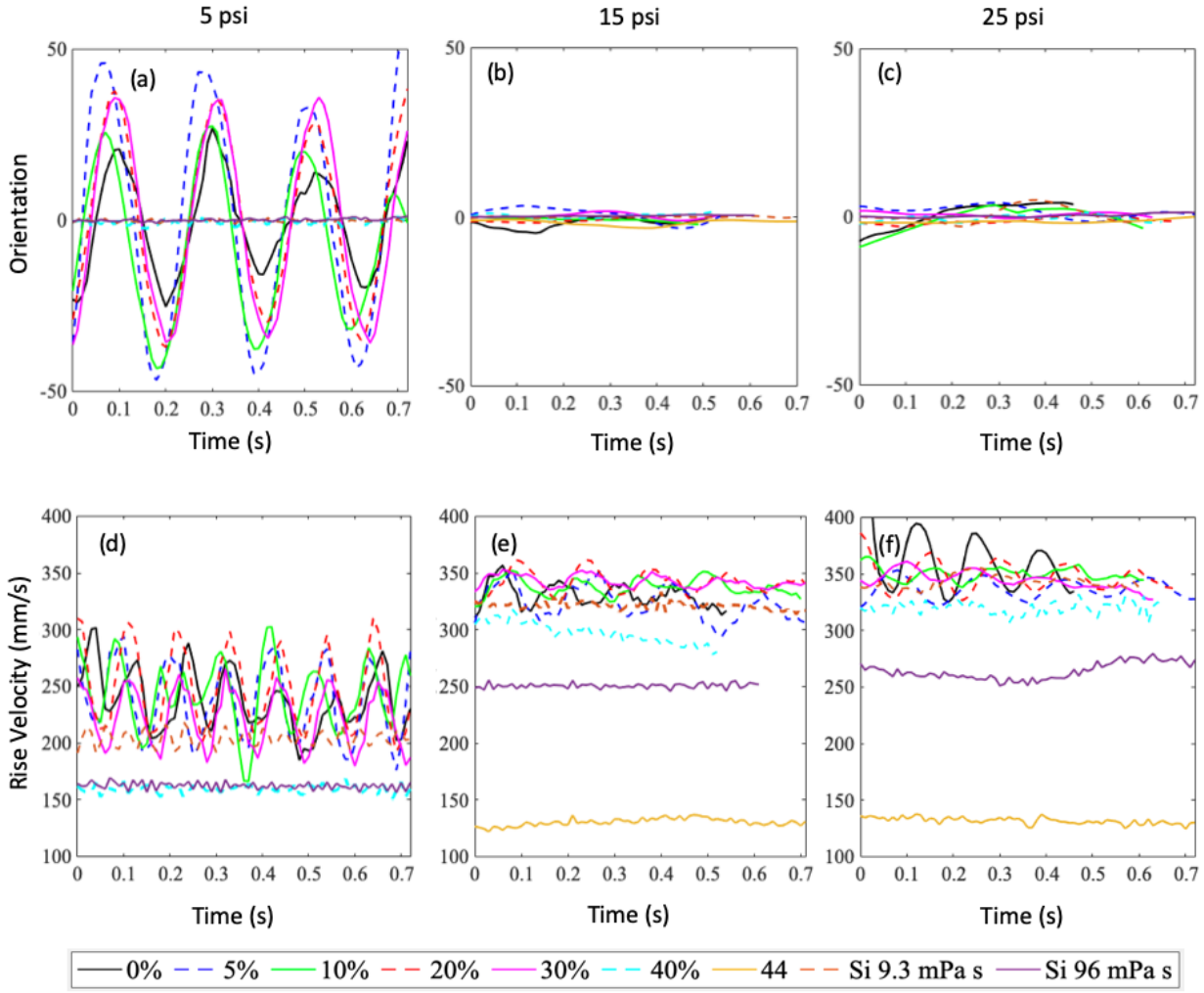

Figure 6.4. Bubble orientation (first row) and rise velocity (second row) for the (a,d) 5 psi, (b, e) 15 psi and (c,f) 25 psi injection pressures.

Figure 6.5 shows the amplitude of oscillation in rise velocity normalized by the average rise velocity vs. (a) $Re = \frac{\rho u_b d}{\mu}$, (b) $Bo = \frac{\Delta\rho g d^2}{\sigma}$ (c) $Mo = \frac{g\mu^4\Delta\rho}{\rho^2\sigma^3}$, (d) $Ca = \frac{u_b\mu}{\sigma}$, (e) $St = \frac{fd}{u_b}$ and

(f) $Ro = \frac{\rho f {d_e}^2}{\mu} = (St\ Re)$ on log-log plots, where ρ is suspension density, $\Delta\rho$ is the difference between the density of particles and fluid, u_b is bubble rise velocity, d is bubble diameter, μ is suspension viscosity and σ is the fluid surface tension. The surface tension of cornstarch suspensions is assumed to be the same as that of water (72 mN/m) since the confining stress comes from the surface tension of the fluid. f is the bubble rise oscillation frequency, determined from the maximum in the Fourier transform of the rise velocity vs. time for each case. The viscosity is approximated for the cornstarch-water solutions from the experimental viscosity vs. shear rate curves (Figure 6.7) with the shear rate approximated by dividing the average rise velocity by the bubble width. All the plots display that the bubble in water and low packing fractions of cornstarch (5-30 vol%) has the highest normalized rise velocity amplitude, indicating wobbling motion. The results show that the data do not collapse onto one curve across all suspension and bubble injection conditions with the use of any non-dimensional number, but the Bo achieves the best collapse. The collapse with Bo and not with other dimensionless parameters is somewhat surprising since this parameter does not account for viscosity, while our results generally show that wobbling only occurs in low viscosity fluids with small bubbles. However, this result is somewhat consistent with Grace's [154] finding that the regime of bubble behavior is dictated by Bo in addition to Re and Mo. Further, Bo accounts directly for bubble size, and our results clearly show that wobbling only occurs at small bubble sizes. Interestingly, bubble properties which are not known a priori, such as rise velocity and oscillation frequency, do not help to collapse velocity oscillation data, at least not in the dimensionless parameters investigated here.

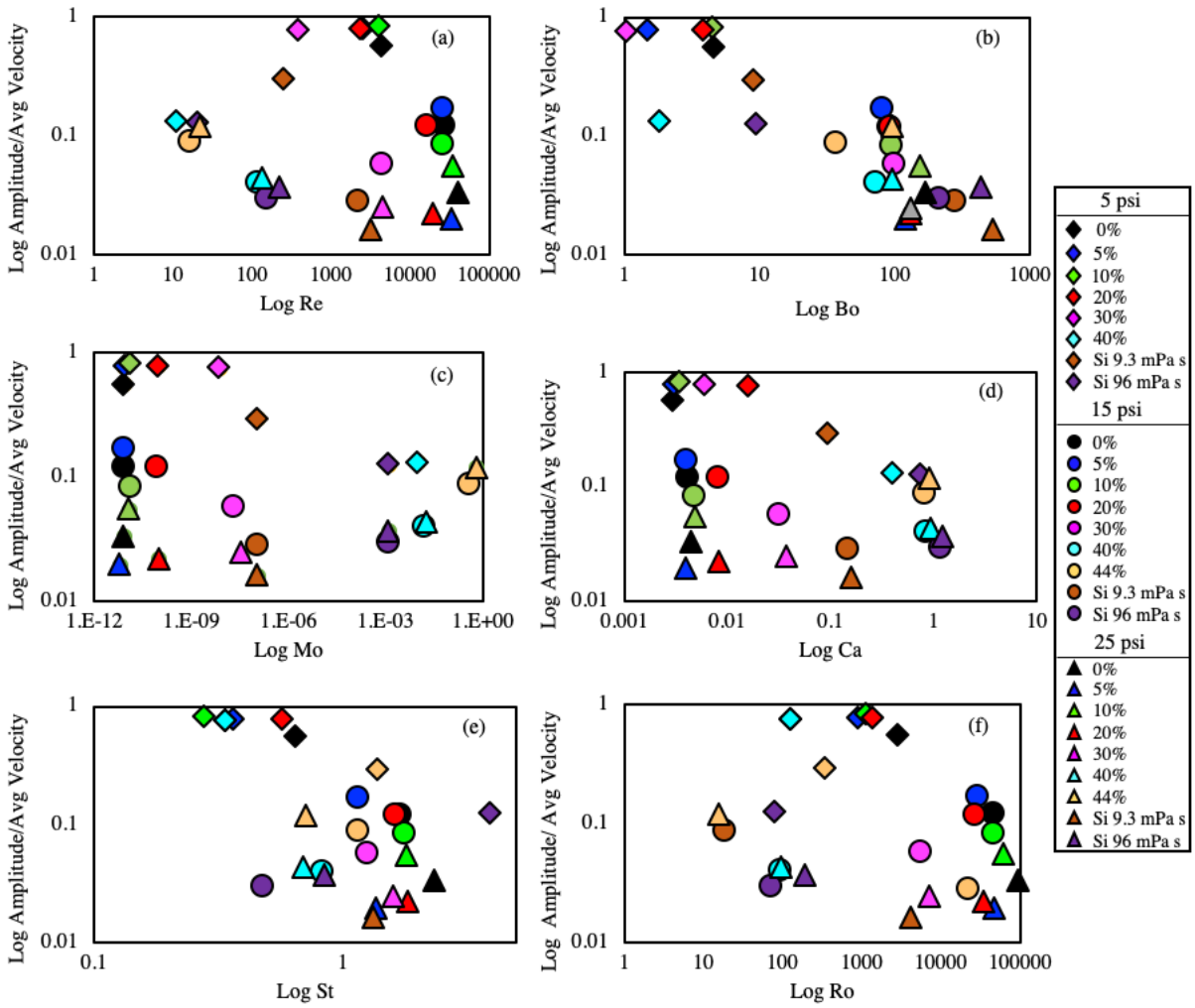

Figure 6.5. Amplitude of oscillation in rise velocity normalized by the average rise velocity vs. (a) Re, (b) Bo, (c) Mo, (d) Ca, (e) St and (f) Ro on a log-log scale.

Figure 6.6 shows the bubble conditions in our study plotted on the regime map of Grace et al. [154], with the color of the marker indicating the normalized velocity oscillation amplitude, which we use to quantify the extent of bubble wobbling. Results show that for the high Re and intermediate Bo, the bubble has a wobbling behavior which accounts for the bubble in water and low packing fraction of cornstarch (5-30 vol%) at 5 psi which are shown with the dark red color. At these conditions we observed the highest ratio of velocity oscillation amplitude to average rise velocity (~0.8-1) which justifies the oscillatory rise behavior. At intermediate Re and intermediate

Bo, we observed that the bubbles are in ellipsoidal regime which is caused by the high viscosity of fluid surrounding the bubble. These data marked pink in color belong to 40 vol%, silicone oil 9.3 mPa s and silicone oil 96 mPa s at 5 psi, and 44 vol% at 15 and 25 psi. In this regime, we observed an intermediate ratio of velocity oscillation amplitude to average rise velocity (~ 0.3-0.1). The shape regime shown in predicted by this regime map agrees with bubble rise shapes seen in Figs. 6.1-6.3 in our study. At high Bo, the bubbles are in the spherical-cap regime, and we observe a very low ratio of velocity oscillation amplitude to average rise velocity (~0.1-0.01). These data are shown in light pink. As such, Figure 6 show that our results match well with the regime map of Grace et al. [154], and wobbling quantified by high values of normalized velocity oscillation occurs at high Re, low Bo conditions.

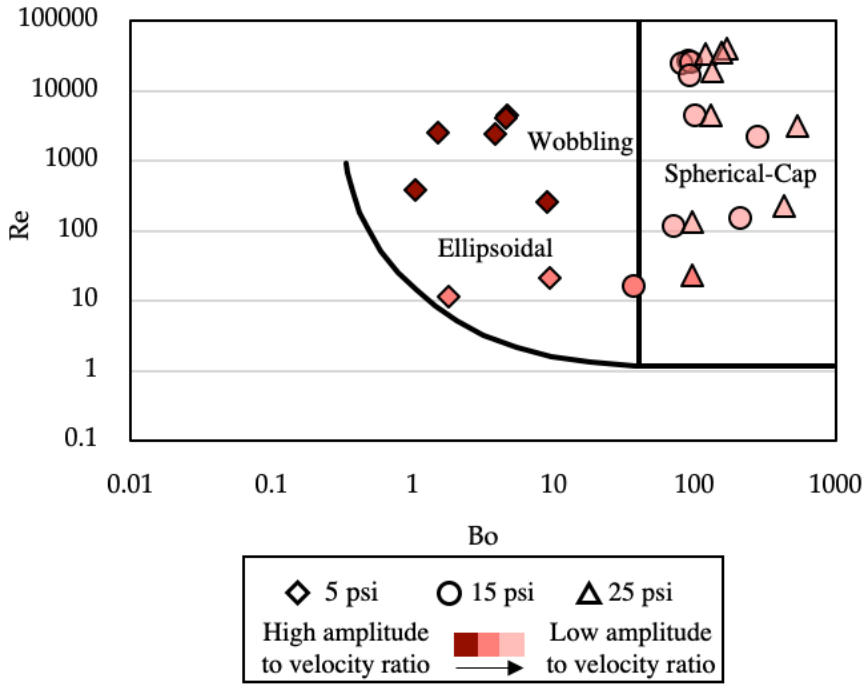

Figure 6.6. Shape regimes for bubbles through liquids in our study plotted on the regime map of Grace et al. [154], using the black dividing lines of the prior work.

Figure 6.7 shows the fluid viscosity surrounding the bubble vs. shear rate with markers showing the approximated viscosity in the fluid surrounding the bubbles for each packing fraction of (a) 5%, (b) 10%, (c) 20%, (d) 30%, (e) 40 %, and (f) 44 % and (g) for all fluids studied on the same plot. The markers demonstrate that all the bubbles in our experiment lie in essentially Newtonian regimes for the packing fraction below 30% and in shear-thinning regimes for the packing fractions 30% and above for all bubble sizes. It can be interpreted that the order of magnitude for the fluid viscosity in the lower packing fraction of 5-20 vol% is ~ 1 mPa s, the medium packing fraction of 30 vol% is ~ 10 and mPa s the higher packing fraction of 40 and 44 vol % is ~ 100 mPa s. At lowest injection pressure, the shear rate is always the highest, and as the injection pressure or bubble size increases, the shear rate for each condition decreases. While based on prior studies [144], [146], wobbling would be more expected in shear-thinning fluids than in Newtonian fluids, in our study wobbling occurs in the low-viscosity Newtonian fluids for small bubbles, but not in the high-viscosity shear-thinning fluid for any bubble size. We attribute this difference from past findings to the high viscosity damping bubble oscillation, even when the fluid is shear-thinning.

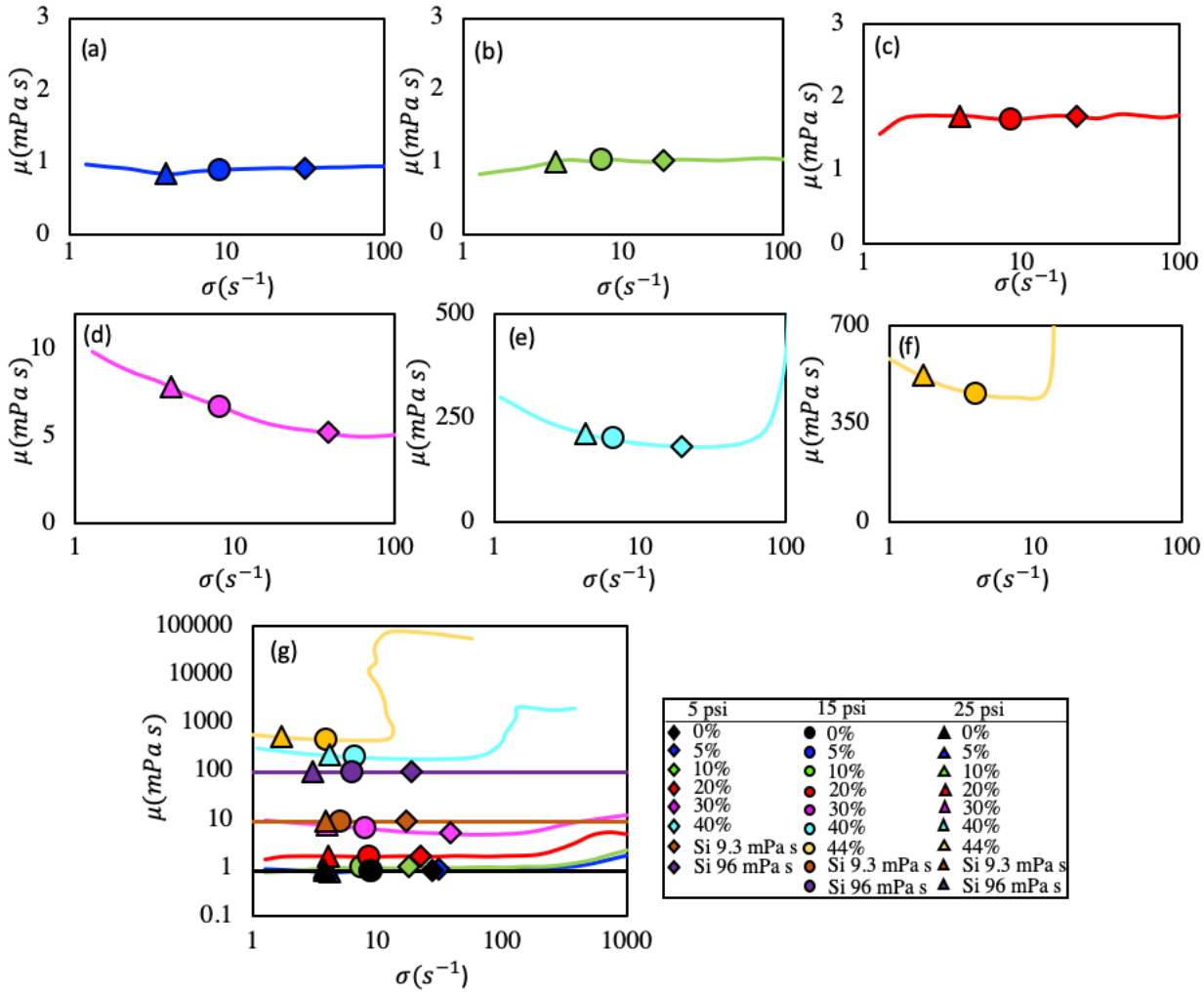

Figure 6.7. Experimentally measured effective viscosity vs shear rate for cornstarch-water suspensions with markers showing the approximate viscosity in the fluid surrounding the bubbles for each condition.

6.4 Conclusion

In summary, we investigated the bubble shape and rise behavior in cornstarch-water suspensions at different packing fractions and injection pressures. The results show that the wobbling behavior occurs at high Re and intermediate Bo, regardless of the fluid being Newtonian or shear thinning. In this regime, we observed a high ratio of the amplitude of oscillating rise velocity to average rise velocity, indicating oscillating bubble dynamics. At intermediate Re and intermediate Bo, the ellipsoidal regime occurs due to the high viscosity of the fluid surrounding

the bubble and the normalized amplitude of oscillating rise velocity is intermediate. At high Bo, the bubble is in spherical-cap regime and the normalized amplitude of oscillating rise velocity is low. We leave it to future work to study how bubble dynamics change in shear-thickening regimes of cornstarch-water suspensions as well as in systems with 3D geometry and different nozzle configurations in order to more fully understand the non-dimensional numbers needed to fully characterize bubble oscillation behavior.

Chapter 7 : Conclusion and Future Work

In this thesis, we investigate the dynamics of rising bubbles in three different media: 1) fluidized beds, 2) Newtonian fluids, and 3) non-Newtonian dense suspensions. Chapters 2 and 3 in this dissertation are dedicated to develop a theoretical understanding of hydrodynamic instabilities occurring in a three-dimensional fluidized bed by conducting CFD-DEM simulations which are compared with prior experimental magnetic resonance imaging (MRI) work [33], [155]. We were able to explain the anomalous collapse of a bubble in a side-by-side injection. This collapse occurs due to preferential gas channeling into the larger bubble, as determined by looking a simulation predictions of gas streamlines in and near the bubbles, something we were incapable of measuring experimentally. We also were able to explain the underlying mechanism behind the alternating asynchronous jet pinch-off by looking into the drag forces acting on the particles, also something that we were not able of measuring experimentally. In Chapter 4, we conducted experiments to understand different interaction patterns between two gas jets in Newtonian fluids; this investigation was inspired by our study in Chapter 3. We were able to identify three regimes of bubble breakoff as well as the fact that a mixed Capillary number (Ca) was the key parameter to determine the bubble size produced. We found that the ratio of bubble diameter to separation distance between jets was the key parameter which dictated the regime of bubble breakoff. We also proposed a theoretical model, based on a coupled harmonic oscillator model, which can capture the alternating bubbling regime. In Chapters 4 and 5 we investigated the following questions on bubble rise dynamics:

1) How do the rheological properties of non-Newtonian fluids and dense suspensions affect single bubble dynamics, in particular rise velocity, bubble shape and flow field surrounding the bubble?

2) How do non-Newtonian properties affect interaction and coalescence of consecutive bubbles?

All these questions overlap, and we addressed them in projects which work in conjunction with one another. To answer these two questions, we sought to understand the effect of complex properties of cornstarch-water suspension on single bubble dynamics and consecutive bubble dynamics in a pseudo two-dimensional system. We identified that for single bubbles rising in a dense suspension composed of cornstarch and water, bubbles wobble (oscillate in rise velocity and shape) at intermediate Bond number (Bo) and high Reynolds number (Re). However, these measurements were only limited to Newtonian and shear-thinning regimes of cornstarch-water suspensions due to the smaller values of experimentally applied shear rate achieved in the system used. Dynamics of these bubbles can be further investigated in the shear-thickening regime of cornstarch-water suspension (higher values of applied shear rate) both experimentally and computationally to test the hypothesis that the shear-thickening and jamming nature of dense suspensions will cause different types of bubble oscillation. We also discovered that for a case of consecutive bubbles formed in a cornstarch-water suspension, a periodic coalescence of bubbles occurs at the same points in space in 40 vol% suspension at a specific flow rate (Froude number) due to the rheology of the suspension where the leading bubbles entering a shear-thickening regime, while trailing bubbles are in a shear-thinning regime, leading to coalescence. Manipulation of gas injection can be used to tailor the regular coalescence properties for desired behavior in industrial equipment. In addition, this discovery can be used to identify other conditions for potential regular coalescence in other fluids with strong shear-thickening regimes, such as suspensions of glass beads in silicone oil and suspensions of silica particles in polyethylene glycol (PEG). Furthermore, all of the above-mentioned dynamics can be investigated in a three-

dimensional system using new MRI techniques developed by our research group by leveraging the optical imaging results from our two-dimensional system as a basis to understand how bubbles rise in non-Newtonian fluids in unprecedented detail, and what are the similarities and differences in dynamics between 2D and 3D bubbles.

Taken together, these potential future studies will build upon the finding is this thesis to provide unprecedented insight into bubble behavior in complex fluids and answer the fundamental question of how bubbles respond to different rheological behavior of non-Newtonian suspensions. These potential futures studies will bring insights to both interfacial and buoyancy-driven physics as well as rheology. These insights will be applicable to a variety of industrial systems and natural phenomena.

References

[1] B. P. Boudreau, B. D. Johnson, Y. Furukawa, K. M. Dorgan, and P. A. Jumars, "Bubble growth and rise in soft sediments," no. 6, pp. 517–520, 2005.

[2] C. Bourry *et al.*, "Free gas and gas hydrates from the Sea of Marmara , Turkey Chemical and structural characterization," *Chem. Geol.*, vol. 264, pp. 197–206, 2009.

[3] S. Vergniolle, "Strombolian explosions 1 . A large bubble breaking at the surface of a lava are only slightly damped explosions," *J. Geophys. Res.*, vol. 101, 1996.

[4] Y. T. Shah, B. G. Kelkar, S. P. Godbole, and W.-D. Deckwer, "Design parameters estimations for bubble column reactors," *AIChE J.*, vol. 28, no. 3, pp. 353–379, May 1982.

[5] D. Rodrigue, D. De Kee, and C. F. Chan Man Fong, "An experimental study of the effect of surfactants on the free rise velocity of gas bubbles," *J. Nonnewton. Fluid Mech.*, vol. 66, no. 2–3, pp. 213–232, 1996.

[6] S. G. Cohen *et al.*, "The mechanics of large bubbles rising through extended liquids and through liquids in tubes," *Proc. R. Soc. London. Ser. A. Math. Phys. Sci.*, vol. 200, no. 1062, pp. 375–390, Feb. 1950.

[7] D. Fraggedakis, M. Pavlidis, Y. Dimakopoulos, and J. Tsamopoulos, "On the velocity discontinuity at a critical volume of a bubble rising in a viscoelastic fluid," *J. Fluid Mech.*, vol. 789, pp. 310–346, 2016.

[8] S. B. Pillapakkam, P. Singh, D. Blackmore, and N. Aubry, "Transient and steady state of a rising bubble in a viscoelastic fluid," *J. Fluid Mech.*, vol. 589, pp. 215–252, Oct. 2007.

[9] A. Belmonte, "Self-oscillations of a cusped bubble rising through a micellar solution," *Rheol. Acta*, vol. 39, no. 6, pp. 554–559, 2000.

[10] N. Z. Handzy and A. Belmonte, "Oscillatory rise of bubbles in wormlike micellar fluids

with different microstructures," *Phys. Rev. Lett.*, vol. 92, no. 12, pp. 15–18, 2004.

[11] G. Kong, H. Mirsandi, K. A. Buist, E. A. J. F. Peters, M. W. Baltussen, and J. A. M. Kuipers, "Oscillation dynamics of a bubble rising in viscous liquid," *Exp. Fluids*, vol. 60, no. 8, p. 130, 2019.

[12] R. Poryles and V. Vidal, "Rising bubble instabilities and fragmentation in a confined polymer solution," *J. Nonnewton. Fluid Mech.*, vol. 241, pp. 26–33, 2017.

[13] M. Ohta, Y. Yoshida, and M. Sussman, "A computational study of the dynamic motion of a bubble rising in Carreau model fluids," *Fluid Dyn. Res.*, vol. 42, no. 2, 2010.

[14] M. Ohta, S. Kimura, T. Furukawa, Y. Yoshida, and M. Sussman, "Numerical simulations of a bubble rising through a shear-thickening fluid," *J. Chem. Eng. Japan*, vol. 45, no. 9, pp. 713–720, 2012.

[15] S. Von Kann, J. H. Snoeijer, and D. Van Der Meer, "Velocity oscillations and stop-go cycles: The trajectory of an object settling in a cornstarch suspension," *Phys. Rev. E - Stat. Nonlinear, Soft Matter Phys.*, vol. 87, no. 4, 2013.

[16] C. R. Müller, J. F. Davidson, J. S. Dennis, and A. N. Hayhurst, "A study of the motion and eruption of a bubble at the surface of a two-dimensional fluidized bed using Particle image velocimetry (PIV)," *Ind. Eng. Chem. Res.*, vol. 46, no. 5, pp. 1642–1652, Feb. 2007.

[17] J. Westerweel, "Fundamentals of digital particle image velocimetry," *Meas. Sci. Technol.*, vol. 8, pp. 1379–1392, 1997.

[18] D. Parker, C. Broadbent, P. Fowles, M. R. Hawkesworth, and P. McNeil, "Positron emission particle tracking-a technique for studying flow within engineering equipment," *Nucl. Instruments*, vol. 326, no. 3, pp. 592–607, 1993.

[19] N. Devanathan, D. Moslemian, and M. Dudukovic, "Flow mapping in bubble columns using

CARPT," *Chem. Eng. Sci.*, vol. 45, no. 8, pp. 2285–2291, 1990.

[20] R. Mudde, "Time-resolved X-ray tomography of a fluidized bed," *Powder Technol.*, 2010.

[21] F. Fischer, D. Hoppe, and E. Schleicher, "An ultra fast electron beam x-ray tomography scanner," *Meas. Sci. Technol.*, vol. 19, no. 9, 2008.

[22] W. Warsito and L. Fan, "Neural network based multi-criterion optimization image reconstruction technique for imaging two-and three-phase flow systems using electrical capacitance," *Meas. Sci. Technol.*, vol. 12, pp. 2198–2210, 2001.

[23] M. van der Hoef and R. Beetstra, "Lattice-Boltzmann simulations of low-Reynolds-number flow past mono-and bidisperse arrays of spheres: results for the permeability and drag force," *J. Fluid Mech.*, vol. 528, pp. 233–254, 2005.

[24] N. G. Deen, M. V. S. Annaland, M. A. Van der Hoef, and J. A. M. Kuipers, "Review of discrete particle modeling of fluidized beds," *Chem. Eng. Sci.*, vol. 62, no. 1–2, pp. 28–44, 2007.

[25] Y. Tsuji, T. Kawaguchi, and T. Tanaka, "Discrete particle simulation of two-dimensional fluidized bed," *Powder Technol.*, vol. 77, no. 1, pp. 79–87, Oct. 1993.

[26] C. Y. Wen and Y. H. Yu, "A generalized method for predicting the minimum fluidization velocity," *AIChE J.*, vol. 12, no. 3, pp. 610–612, 1966.

[27] R. Beetstra, M. van der Hoef, and J. A. M. Kuipers, "Numerical study of segregation using a new drag force correlation for polydisperse systems derived from lattice-Boltzmann simulations," *Chem. Eng. Sci.*, vol. 62, no. 1–2, pp. 246–255, 2007.

[28] J. Ding and D. Gidaspow, "A bubbling fluidization model using kinetic theory of granular flow," *AIChE J.*, vol. 36, no. 4, pp. 523–538, 1990.

[29] C. M. Boyce, A. Penn, A. Padash, M. Lehnert, K. P. Pruessmann, and C. R. Müller,

"Anomalous collapse of interacting bubbles in a fluidized bed: A magnetic resonance imaging study," *Phys. Rev. Fluids*, vol. 4, no. 3, p. 034303, Mar. 2019.

[30] A. Padash and C. M. Boyce, "Collapse of a bubble injected side-by-side with another bubble into an incipiently fluidized bed: A CFD-DEM study," *Phys. Rev. Fluids*, vol. 5, no. 3, p. 34304, Mar. 2020.

[31] A. Penn, A. Padash, M. Lehnert, K. Pruessmann, C. R. Muller, and C. M. Boyce, "Asynchronous bubble pinch-off pattern arising in fluidized beds due to jet interaction: A magnetic resonance imaging and computational modeling study," *Phys. Rev. Fluids*, vol. 5, no. 9, p. 94303, Sep. 2020.

[32] A. Padash, B. Chen, and C. M. Boyce, "Characterizing alternating bubbles emerging from two interacting vertical gas jets in a liquid," *Chem. Eng. Sci.*, vol. 248, p. 117199, Feb. 2022.

[33] A. Penn, A. Padash, M. Lehnert, K. P. Pruessmann, C. R. Müller, and C. M. Boyce, "Asynchronous bubble pinch-off pattern arising in fluidized beds due to jet interaction: A magnetic resonance imaging and computational modeling study," *Phys. Rev. Fluids*, vol. 5, no. 9, pp. 1–17, 2020.

[34] J. F. Davidson and D. Harrison, "Fluidized Particles, Cambridge University Press," *Cambridge, New York*, 1963.

[35] R. M. Davies and G. I. Taylor, "The mechanics of large bubbles rising through extended liquids and through liquids in tubes," *Proc. R. Soc. London. Ser. A. Math. Phys. Sci.*, vol. 200, no. 1062, pp. 375–390, 1950.

[36] J. Dennis, "Properties of stationary (bubbling) fluidised beds relevant to combustion and gasification systems," *Fluid. Bed Technol. Near-Zero Emiss. Combust. Gasif.*, pp. 77–146, 2013.

[37] T. W. Asegehegn, M. Schreiber, and H. J. Krautz, “Investigation of bubble behavior in fluidized beds with and without immersed horizontal tubes using a digital image analysis technique,” *Powder Technol.*, vol. 210, no. 3, pp. 248–260, Jul. 2011.

[38] P. A. Cundall and O. D. L. Strack, “A discrete numerical model for granular assemblies,” *http://dx.doi.org/10.1680/geot.1979.29.1.47*, vol. 29, no. 1, pp. 47–65, May 2015.

[39] T. B. Anderson and R. Jackson, “Fluid mechanical description of fluidized beds: Equations of Motion,” *Ind. Eng. Chem. Fundam.*, vol. 6, no. 4, pp. 527–539, Nov. 1967.

[40] C. Y. Wen and Y. H. Yu, “A generalized method for predicting the minimum fluidization velocity,” *AIChE J.*, vol. 12, no. 3, pp. 610–612, 1966.

[41] C. Goniva, C. Kloss, N. G. Deen, J. A. M. Kuipers, and S. Pirker, “Influence of rolling friction on single spout fluidized bed simulation,” *Particuology*, vol. 10, no. 5, pp. 582–591, 2012.

[42] H. G. Weller, G. Tabor, H. Jasak, and C. Fureby, “A tensorial approach to computational continuum mechanics using object-oriented techniques,” *Comput. Phys.*, vol. 12, no. 6, p. 620, 1998.

[43] C. Kloss, C. Goniva, A. Hager, S. Amberger, and S. Pirker, “Models, algorithms and validation for opensource DEM and CFD–DEM,” *Prog. Comput. Fluid Dyn.*, vol. 12, no. 3, pp. 140–152, 2012.

[44] C. M. Boyce, A. Ozel, N. P. Rice, G. J. Rubinstein, D. J. Holland, and S. Sundaresan, “Effective particle diameters for simulating fluidization of non-spherical particles: CFD-DEM models vs. MRI measurements,” *AIChE J.*, vol. 63, no. 7, pp. 2555–2568, Jul. 2017.

[45] C. R. Müller, D. J. Holland, A. J. Sederman, S. A. Scott, J. S. Dennis, and L. F. Gladden, “Granular temperature: Comparison of Magnetic Resonance measurements with Discrete

Element Model simulations," *Powder Technol.*, vol. 184, no. 2, pp. 241–253, May 2008.

[46] S. Radl and S. Sundaresan, "A drag model for filtered Euler–Lagrange simulations of clustered gas–particle suspensions," *Chem. Eng. Sci.*, vol. 117, pp. 416–425, Sep. 2014.

[47] C. M. Boyce, D. J. Holland, S. A. Scott, and J. S. Dennis, "Limitations on Fluid Grid Sizing for Using Volume-Averaged Fluid Equations in Discrete Element Models of Fluidized Beds," *Ind. Eng. Chem. Res.*, vol. 54, no. 43, pp. 10684–10697, Oct. 2015.

[48] A. Penn, T. Tsuji, D. O. Brunner, C. M. Boyce, K. P. Pruessmann, and C. R. Müller, "Real-time probing of granular dynamics with magnetic resonance," *Sci. Adv.*, vol. 3, no. 9, p. 1701879, 2017.

[49] M. Stehling, R. Turner, and P. Mansfield, "Echo-planar imaging: magnetic resonance imaging in a fraction of a second," *Science (80-.).*, vol. 254, no. 5028, pp. 43–50, 1991.

[50] K. P. Pruessmann, M. Weiger, M. B. Scheidegger, and P. Boesiger, "SENSE: Sensitivity Encoding for Fast MRI," *Magn. Reson. Med. An Off. J. Int. Soc. Magn. Reson. Med.*, vol. 42, no. 5, pp. 952–962, 1999.

[51] P. Callaghan, *Principles of nuclear magnetic resonance microscopy*. Oxford University Press on Demand, 1993.

[52] C. M. Boyce, J. F. Davidson, D. J. Holland, S. A. Scott, and J. S. Dennis, "The origin of pressure oscillations in slugging fluidized beds: Comparison of experimental results from magnetic resonance imaging with a discrete element," *Chem. Eng. Sci.*, vol. 116, pp. 611–622, 2014.

[53] C. P. McLaren, T. M. Kovar, A. Penn, C. R. Müller, and C. M. Boyce, "Gravitational instabilities in binary granular materials," *Proc. Natl. Acad. Sci.*, vol. 116, no. 19, pp. 9263–9268, 2019.

[54] C. M. Boyce, D. J. Holland, S. A. Scott, and J. S. Dennis, "Adapting data processing to compare model and experiment accurately: A discrete element model and magnetic resonance measurements of a 3d cylindrical fluidized," *Ind. Eng. Chem. Res.*, vol. 52, no. 50, pp. 18085–18094, Dec. 2013.

[55] C. S. WU and W. B. WHITING, "Interacting jets in a fluidized bed," *Chem. Eng. Commun.*, vol. 73, no. 1, pp. 1–17, 1988.

[56] Q. Guo, Z. Tang, G. Yue, Z. Liu, and J. Zhang, "Flow pattern transition in a large jetting fluidized bed with double nozzles," *AIChE J.*, vol. 47, no. 6, pp. 1309–1317, Jun. 2001.

[57] M. Van Buijtenen, W. Van Dijk, N. G. Deen, J. A. M. Kuipers, T. Leadbeater, and D. Parker, "Numerical and experimental study on multiple-spout fluidized beds," *Chem. Eng. Sci.*, vol. 66, no. 11, pp. 2368–2376, 2011.

[58] P. Philippe and M. Badiane, "Localized fluidization in a granular medium," *Phys. Rev. E*, vol. 87, no. 4, Apr. 2013.

[59] J. Ngoma *et al.*, "Interaction between two localized fluidization cavities in granular media: Experiments and numerical simulation," *Geomech. From Micro to Macro*, 2015.

[60] K. Zhang, P. Pei, S. Brandani, H. Chen, and Y. Yang, "CFD simulation of flow pattern and jet penetration depth in gas-fluidized beds with single and double jets," *Chem. Eng. Sci.*, vol. 68, no. 1, pp. 108–119, 2012.

[61] R. Hong, Q. Guo, G. Luo, J. Zhang, and J. Ding, "On the jet penetration height in fluidized beds with two vertical jets," *Powder Technol.*, vol. 133, no. 1–3, pp. 216–227, 2003.

[62] M. Pore *et al.*, "Magnetic resonance studies of a gas–solids fluidised bed: Jet–jet and jet–wall interactions," *Particuology*, vol. 8, no. 6, pp. 617–622, 2010.

[63] M. Bieberle, F. Fischer, E. Schleicher, H. J. Menz, H. G. Mayer, and U. Hampel, "Ultrafast

cross-sectional imaging of gas-particle flow in a fluidized bed," *AIChE J.*, vol. 56, no. 8, pp. 2221–2225, Aug. 2010.

[64] B. Harms, S., Stapf, S., & Blümich, "Application of k-and q-space encoding NMR techniques on granular media in a 3D model fluidized bed reactor," *J. Magn. Reson.*, vol. 178, no. 2, pp. 308–317, 2006.

[65] R. Stannarius, "Magnetic resonance imaging of granular materials," *Rev. Sci. Instrum.*, vol. 88, no. 5, p. 051806, May 2017.

[66] E. Fukushima, "Nuclear magnetic resonance as a tool to study flow," *Annu. Rev. Fluid Mech.*, vol. 31, pp. 95–123, 1999.

[67] M. Pore *et al.*, "A comparison of magnetic resonance, X-ray and positron emission particle tracking measurements of a single jet of gas entering a bed of particles," *Chem. Eng. Sci.*, vol. 122, pp. 210–218, 2015.

[68] C. R. Müller *et al.*, "Geometrical and hydrodynamical study of gas jets in packed and fluidized beds using magnetic resonance," *Can. J. Chem. Eng.*, vol. 87, no. 4, pp. 517–525, Aug. 2009.

[69] A. C. Rees *et al.*, "The nature of the flow just above the perforated plate distributor of a gas-fluidised bed, as imaged using magnetic resonance," *Chem. Eng. Sci.*, vol. 61, no. 18, pp. 6002–6015, 2006.

[70] A. Penn, T. Tsuji, D. O. Brunner, C. M. Boyce, K. P. Pruessmann, and C. R. Müller, "Real-time probing of granular dynamics with magnetic resonance," *Sci. Adv.*, vol. 3, no. 9, p. 1701879, Sep. 2017.

[71] C. R. Boyce, C. M., Penn, A., Pruessmann, K. P., & Müller, "Magnetic resonance imaging of gas–solid fluidization with liquid bridging," *AIChE J.*, vol. 64, no. 8, pp. 2958–2971,

Aug. 2018.

[72] A. Penn, C. M. Boyce, T. Kovar, T. Tsuji, K. P. Pruessmann, and C. R. Müller, "Real-Time Magnetic Resonance Imaging of Bubble Behavior and Particle Velocity in Fluidized Beds," *Ind. Eng. Chem. Res.*, vol. 57, no. 29, pp. 9674–9682, Jul. 2018.

[73] C. M. Boyce, A. Penn, M. Lehnert, K. P. Pruessmann, and C. R. Müller, "Characteristics of a single jet injected into an incipiently fluidized bed: A magnetic resonance imaging study," *Adv. Powder Technol.*, vol. 30, no. 12, pp. 3146–3152, 2019.

[74] C. R. Penn, A., Boyce, C.M., Pruessmann, K.P. and Müller, "Regimes of jetting and bubbling in a fluidized bed studied using real-time magnetic resonance imaging," *Chem. Eng. J.*, vol. 383, p. 123185, 2020.

[75] D. Geldart, "Types of gas fluidization," *Powder Technol.*, vol. 7, no. 5, pp. 285–292, May 1973.

[76] M. Stehling, R. Turner, and P. Mansfield, "Echo-planar imaging: magnetic resonance imaging in a fraction of a second," *Science (80-.).*, vol. 254, no. 5028, pp. 43–50, 1991.

[77] P. T. Callaghan., "Principles of nuclear magnetic resonance microscopy," *Oxford Univ. Press*, Apr. 1993.

[78] C. Kloss, C. Goniva, A. Hager, S. Amberger, and S. Pirker, "Models, algorithms and validation for opensource DEM and CFD–DEM," *Prog. Comput. Fluid Dyn.*, vol. 12, no. 3, pp. 140–152, 2012.

[79] C. Y. Wen and Y. H. Yu, "A generalized method for predicting the minimum fluidization velocity," *AIChE J.*, vol. 12, no. 3, pp. 610–612, May 1966.

[80] C. Boyce, N. Rice, A. Ozel, and J. Davidson, "Magnetic resonance characterization of coupled gas and particle dynamics in a bubbling fluidized bed," *Phys. Rev. Fluids*, vol. 1,

no. 7, p. 74201, Nov. 2016.

[81] M. Link, J.M., Godlieb, W., Tripp, P., Deen, N.G., Heinrich, S., Kuipers, J.A.M., Schönherr, M. and Peglow, "Comparison of fibre optical measurements and discrete element simulations for the study of granulation in a spout fluidized bed," *Powder Technol.*, vol. 189, no. 2, pp. 202–217, 2009.

[82] A. B. Feng, Y.Q. and Yu, "Assessment of model formulations in the discrete particle simulation of gas− solid flow," *Ind. Eng. Chem. Res.*, vol. 43, no. 26, pp. 8378–8390, Dec. 2004.

[83] J. Kozney, "Uber kapillare leitung der wasser in boden," *Sitzungsber Akad. Wiss., Wien*, vol. 136, pp. 271–306, 1927.

[84] P. B. Blake, T.R., Webb, H. and Sunderland, "The nondimensionalization of equations describing fluidization with application to the correlation of jet penetration height," *Chem. Eng. Sci.*, vol. 45, no. 2, pp. 365–371, 1990.

[85] W. C. Yang and D. L. Keairns, "Estimating the Jet Penetration Depth of Multiple Vertical Grid Jets," *Ind. Eng. Chem. Fundam.*, vol. 18, no. 4, pp. 317–320, Nov. 1979.

[86] J. M. D. Merry, "Penetration of vertical jets into fluidized beds," *AIChE J.*, vol. 21, no. 3, pp. 507–510, 1975.

[87] Q. Guo, Z. Liu, and J. Zhang, "Flow characteristics in a large jetting fluidized bed with two nozzles," *Ind. Eng. Chem. Res.*, vol. 39, no. 3, pp. 746–751, 2000.

[88] J. Guo, Q., Zhang, J. and Werther, "Jetting transition velocity in a jetting fluidized bed with two nozzles," *Chem. Eng. J.*, vol. 92, no. 1–3, pp. 63–67, 2003.

[89] M. RRuzicka, J. Drahoš, J. Zahradník, and N. H. Thomas, "Structure of gas pressure signal at two-orifice bubbling from a common plenum," *Chem. Eng. Sci.*, vol. 55, no. 2, pp. 421–

429, 2000.

[90] M. Ruzickaa, J. Drahoš, J. Zahradník, and N. H. Thomas, “Natural modes of multi-orifice bubbling from a common plenum,” *Chem. Eng. Sci.*, vol. 54, no. 21, pp. 5223–5229, 1999.

[91] S. Xie and R. B. H. Tan, “Bubble formation at multiple orifices—bubbling synchronicity and frequency,” *Ind. Eng. Chem. Res.*, vol. 58, no. 20, pp. 4639–4647, 2003.

[92] F. A. C. Pereira, E. Colli, and J. C. Sartorelli, “Synchronization of two bubble trains in a viscous fluid: Experiment and numerical simulation,” *Phys. Rev. E - Stat. Nonlinear, Soft Matter Phys.*, vol. 87, no. 2, Feb. 2013.

[93] P. Dzienis, R. Mosdorf, and T. Wyszkowski, “Nonlinear dynamics of self-organising bubble departures from twin nozzles,” *Meccanica*, vol. 54, no. 14, pp. 2119–2130, Nov. 2019.

[94] M. Iguchi, K. Takahashi, and H. Kiuchi, “Merging distance of two air-water vertical bubbling jets subjected to Coanda effect,” *ISIJ Int.*, vol. 39, no. 12, pp. 1311–1313, 1999.

[95] T. B. McNallan, M. J., & King, “Fluid dynamics of vertical submerged gas jets in liquid metal processing systems,” *Metall. Trans. B*, vol. 13, no. 2, pp. 165–173, 1982.

[96] S. Koria, “Principles and applications of gas injection in steelmaking practice,” *Scand. J. Metall.*, vol. 22, pp. 271–279, 1993.

[97] S. R. Syeda and A. M. Ansery, “Formation and Development of Submerged Air Jets,” *J. Mech. Eng.*, vol. 44, no. 2, pp. 137–141, Jan. 2015.

[98] T. Uemura, M. Iguchi, and Y. Ueda, “Visualization of Flow Induced by Bubble Dispersion,” pp. 51–62, 2018.

[99] N. Torres Brauer, B. Serrano Rosales, and H. De Lasa, “Single-Bubble Dynamics in a Dense Phase Fluidized Sand Bed Biomass Gasification Environment,” *Ind. Eng. Chem. Res.*, vol.

59, no. 13, pp. 5601–5614, Apr. 2020.

[100] G. W. Huber, S. Iborra, and A. Corma, “Synthesis of transportation fuels from biomass: Chemistry, catalysts, and engineering,” *Chem. Rev.*, vol. 106, no. 9, pp. 4044–4098, Sep. 2006.

[101] J. A. Ramirez, A. J. Baird, T. J. Coulthard, and J. M. Waddington, “Testing a simple model of gas bubble dynamics in porous media,” *Water Resour. Res.*, vol. 51, no. 2, pp. 1036–1049, 2015.

[102] P. Dzienis, R. Mosdorf, D. T.-T. Science, and U. 2019, “A hydrodynamic criterion of alternative bubble departures,” *doiserbia.nb.rs*, 2019.

[103] A. W. Woods, “Turbulent plumes in nature,” *Annu. Rev. Fluid Mech.*, vol. 42, pp. 391–412, Jan. 2010.

[104] M. C. BBoufadel, S. Socolofsky, J. Katz, D. Yang, C. Daskiran, and W. Dewar, “A review on multiphase underwater jets and plumes: Droplets, hydrodynamics, and chemistry,” *Rev. Geophys.*, vol. 58, no. 3, Sep. 2020.

[105] E. . Capponi, A. and Llewellin, “Experimental observations of bubbling regimes at in-line multi-orifice bubblers,” *Int. J. Multiph. Flow*, vol. 114, pp. 66–81, 2019.

[106] P. Dzienis, R. Mosdorf, … D. T.-M. W. of, and U. 2018, “Formation of bubble chains over twin nozzles,” *MATEC Web Conf.*, vol. 240, p. 05039, 2018.

[107] S. Xie and R. B. H. Tan, “Bubble formation at multiple orifices-bubbling synchronicity and frequency,” *Chem. Eng. Sci.*, vol. 58, no. 20, pp. 4639–4647, 2003.

[108] M. Hashimoto, S. S. Shevkoplyas, B. Zasońska, T. Szymborski, P. Garstecki, and G. M. Whitesides, “Formation of bubbles and droplets in parallel, coupled flow-focusing geometries,” *small*, vol. 4, no. 10, pp. 1795–1805, Oct. 2008.

[109] R. Mosdorf and T. Wyszkowski., "Self-organising structure of bubble departures," *Int. J. Heat Mass Transf.*, vol. 61, no. 1, pp. 277–286, 2013.

[110] A. A. Kulkarni and J. B. Joshi, "Bubble formation and bubble rise velocity in gas− liquid systems: a review," *Ind. Eng. Chem. Res.*, vol. 44, no. 16, pp. 5873–5931, Aug. 2005.

[111] M. C. Boufadel, S. Socolofsky, J. Katz, D. Yang, C. Daskiran, and W. Dewar, "A Review on Multiphase Underwater Jets and Plumes: Droplets, Hydrodynamics, and Chemistry," *Rev. Geophys.*, vol. 58, no. 3, pp. 1–40, 2020.

[112] S. R. Syeda and A. M. Ansery, "Formation and Development of Submerged Air Jets," *J. Mech. Eng.*, vol. 44, no. 2, pp. 137–141, 2015.

[113] S. C. Koria, "Principles and applications of gas injection in steelmaking practice," *Scand. J. Metall.*, vol. 22, no. 5, pp. 271–279, 1993.

[114] T. B. McNallan, M. J., & King, "Fluid dynamics of vertical submerged gas jets in liquid metal processing systems," *Metall. Trans. B*, vol. 13, no. 2, pp. 165–173, 1982.

[115] M. B. Nguyen, K., Daw, C. S., Chakka, P., Cheng, M., Bruns, D. D., Finney, C. E. A., & Kennell, "Spatio-temporal dynamics in a train of rising bubbles," *Chem. Eng. J. Biochem. Eng. J.*, vol. 64, no. 1, pp. 191–197, 1996.

[116] B. Ozturk, D., Morgan, M. L., & Sandnes, "Flow-to-fracture transition and pattern formation in a discontinuous shear thickening fluid," *Commun. Phys.*, vol. 3, no. 1, pp. 1–9, 2020.

[117] M. Ohta, M., Kimura, S., Furukawa, T., Yoshida, Y., & Sussman, "Numerical simulations of a bubble rising through a shear-thickening fluid," *J. Chem. Eng. Japan*, pp. 1203230347–1203230347, 2012.

[118] S. Madec, C., Collin, B., Jerome, J. J. S., & Joubaud, "Puzzling bubble rise speed increase

in dense granular suspensions," *Phys. Rev. Lett.*, vol. 125, no. 7, Aug. 2020.

[119] M. W. Crawford, N. C., Popp, L. B., Johns, K. E., Caire, L. M., Peterson, B. N., & Liberatore, "Shear thickening of corn starch suspensions: Does concentration matter?," *J. Colloid Interface Sci.*, vol. 396, pp. 83–89, 2013.

[120] E. Brown and H. Jaeger, "Dynamic jamming point for shear thickening suspensions," *Phys. Rev. Lett.*, vol. 103, no. 8, Aug. 2009.

[121] J. F. Morris, "Shear Thickening of Concentrated Suspensions: Recent Developments and Relation to Other Phenomena," *Annu. Rev. Fluid Mech.*, vol. 52, pp. 121–144, Jan. 2020.

[122] A. All *et al.*, "Macroscopic discontinuous shear thickening versus local shear jamming in cornstarch," *Phys. Rev. Lett.*, vol. 114, no. 9, pp. 1–5, Mar. 2015.

[123] E. Brown and H. Jaeger, "Shear thickening in concentrated suspensions: phenomenology, mechanisms and relations to jamming," *Reports Prog. Phys.*, vol. 77, no. 4, 2014.

[124] C. Clavauda, A. Be-ruta, B. Metzgera, and Y. Forterrea, "Revealing the frictional transition in shear-thickening suspensions," *Proc. Natl. Acad. Sci. U. S. A.*, vol. 114, no. 20, pp. 5147–5152, 2017.

[125] S. Cao *et al.*, "Shear jamming onset in dense granular suspensions," *J. Rheol. (N. Y. N. Y).*, vol. 65, no. 3, pp. 419–426, May 2021.

[126] J. F. Morris, "Toward a fluid mechanics of suspensions," *Phys. Rev. Fluids*, vol. 5, no. 11, p. 110519, Nov. 2020.

[127] S. von Kann, J. Snoeijer, D. Lohse, and D. van der M. E, "Nonmonotonic settling of a sphere in a cornstarch suspension," *Phys. Rev. E*, vol. 84, no. 6, p. 60401, Dec. 2011.

[128] H. M. Peters, I. R., Majumdar, S., & Jaeger, "Direct observation of dynamic shear jamming in dense suspensions," *Nature*, vol. 532, no. 7598, pp. 214–217, 2016.

[129] F. S. Merkt, R. D. Deegan, D. I. Goldman, E. C. Rericha, and H. L. Swinney, "Persistent Holes in a Fluid," *Phys. Rev. Lett.*, vol. 92, no. 18, p. 184501, May 2004.

[130] K. Pearson, "VII. Mathematical contributions to the theory of evolution.—III. Regression, heredity, and panmixia," *Philos. Trans. R. Soc. London. Ser. A, Contain. Pap. a Math. or Phys. Character*, vol. 187, pp. 253–318, Dec. 1896.

[131] E. Mukhopadhyay, S., Allen, B., & Brown, "Testing constitutive relations by running and walking on cornstarch and water suspensions," *Phys. Rev. E*, vol. 97, no. 5, p. 52604, May 2018.

[132] E. E. B. White, M. Chellamuthu, and J. P. Rothstein, "Extensional rheology of a shear-thickening cornstarch and water suspension," *Rheol. Acta*, vol. 49, no. 2, pp. 119–129, Jan. 2010.

[133] M. M. Denn and J. F. Morris, "Rheology of non-brownian suspensions," *Annu. Rev. Chem. Biomol. Eng.*, vol. 5, pp. 203–228, 2014.

[134] K. Baumgarten, A.S. and Kamrin, "A general constitutive model for dense, fine-particle suspensions validated in many geometries," *Proc. Natl. Acad. Sci.*, vol. 116, no. 42, pp. 20828–20836, 2019.

[135] S. Von Kann, J. H. Snoeijer, and D. Van Der Meer, "Velocity oscillations and stop-go cycles: The trajectory of an object settling in a cornstarch suspension," *Phys. Rev. E - Stat. Nonlinear, Soft Matter Phys.*, vol. 87, no. 4, pp. 1–14, Apr. 2013.

[136] A. Fall, F. Bertrand, G. Ovarlez, and D. Bonn, "Shear thickening of cornstarch suspensions," *J. Rheol. (N. Y. N. Y).*, vol. 56, no. 3, p. 575, Apr. 2012.

[137] R. M. DAVIES and S. G. TAYLOR, "The mechanics of large bubbles rising through extended liquids and through liquids in tubes," *Dyn. Curved Front.*, pp. 377–392, 2014.

[138] G. Kong, H. Mirsandi, K. A. Buist, E. A. J. F. Peters, M. W. Baltussen, and J. A. M. Kuipers, "Oscillation dynamics of a bubble rising in viscous liquid," *Exp. Fluids*, vol. 60, no. 8, pp. 1–13, 2019.

[139] R. Poryles and V. Vidal, "Rising bubble instabilities and fragmentation in a confined polymer solution," *J. Nonnewton. Fluid Mech.*, vol. 241, pp. 26–33, Mar. 2017.

[140] W. P. M. Beenackers, A.A.C.M. and Van Swaaij, "Mass transfer in gas—liquid slurry reactors," *Chem. Eng. Sci.*, vol. 48, no. 18, pp. 3109–3139, 1993.

[141] A. W. Nienow, M. F. EDWARDS, and N. Harnby, *Mixing in the process industries*. Butterworth-Heinemann, 1997.

[142] M. Manga, J. Castro, K. V. Cashman, and M. Loewenberg, "Rheology of bubble-bearing magmas," *J. Volcanol. Geotherm. Res.*, vol. 87, no. 1–4, pp. 15–28, Dec. 1998.

[143] A. Battistella, S. J. G. van Schijndel, M. W. Baltussen, I. Roghair, and M. van Sint Annaland, "On the terminal velocity of single bubbles rising in non-Newtonian power-law liquids," *J. Nonnewton. Fluid Mech.*, vol. 278, no. February, p. 104249, 2020.

[144] L. Zhang, C. Yang, and Z. S. Mao, "Numerical simulation of a bubble rising in shear-thinning fluids," *J. Nonnewton. Fluid Mech.*, vol. 165, no. 11–12, pp. 555–567, 2010.

[145] M. Ohta, S. Kimura, T. Furukawa, Y. Yoshida, and M. Sussman, "Numerical simulations of a bubble rising through a shear-thickening fluid," *J. Chem. Eng. Japan*, vol. 45, no. 9, pp. 713–720, 2012.

[146] S. Li, Y. Ma, T. Fu, C. Zhu, and H. Li, "The viscosity distribution around a rising bubble in shear-thinning non-newtonian fluids," *Brazilian J. Chem. Eng.*, vol. 29, no. 2, pp. 265–274, 2012.

[147] W. Fan and X. Yin, "Influence of orifice spacing on twin bubbles formation in shear-

thinning fluids: Laser image measurement," *Optik (Stuttg).*, vol. 125, no. 7, pp. 1871–1874, Apr. 2014.

[148] Y. E. Yu, S. Khodaparast, and H. A. Stone, "Separation of particles by size from a suspension using the motion of a confined bubble," *Appl. Phys. Lett.*, vol. 112, no. 18, p. 181604, May 2018.

[149] X. Luo, J. Zhang, K. Tsuchiya, and L. S. Fan, "On the rise velocity of bubbles in liquid-solid suspensions at elevated pressure and temperature," *Chem. Eng. Sci.*, vol. 52, no. 21–22, pp. 3693–3699, Nov. 1997.

[150] "Bubble Wake Dynamics in Liquids and Liquid–Solid Suspensions," *Bubble Wake Dyn. Liq. Liq. Suspens.*, 1990.

[151] R. F. Hooshyar, N., Van Ommen, J. R., Hamersma, P. J., Sundaresan, S., & Mudde, "Dynamics of single rising bubbles in neutrally buoyant liquid-solid suspensions," *Phys. Rev. Lett.*, vol. 110, no. 24, Jun. 2013.

[152] M. Sussman and EG Puckett, "A coupled level set and volume-of-fluid method for computing 3D and axisymmetric incompressible two-phase flows," *J. Comput. Phys.*, vol. 162, no. 2, pp. 301–337, 2000.

[153] M. Sussman, "A second order coupled level set and volume-of-fluid method for computing growth and collapse of vapor bubbles," *J. Comput. Phys.*, vol. 187, no. 1, pp. 110–136, 2003.

[154] M. E. W. Clift, Roland, John R. Grace, "Bubbles, Drops, and Particles," 2005. [Online]. Available: https://books.google.com/books?hl=en&lr=&id=UUrOmD8niUQC&oi=fnd&pg=PP1&dq=bubbles+drops+and+particles&ots=pHwTYE7OeW&sig=vf-BU-yCRfR-

I058ybkxd0M60zY#v=onepage&q=bubbles drops and particles&f=false. [Accessed: 21-Oct-2021].

[155] C. M. Boyce, A. Penn, A. Padash, M. Lehnert, K. P. Pruessmann, and C. R. Müller, "Anomalous collapse of interacting bubbles in a fluidized bed: A magnetic resonance imaging study," *Phys. Rev. Fluids*, vol. 4, no. 3, p. 34303, 2019.